Superconductor-Insulator Transition and Charge-Phase Duality in TiN Nanowires

Dissertation
zur Erlangung des Doktorgrades der Naturwissenschaften
(Dr. rer. nat.)
der Fakultät Physik
der Universität Regensburg

vorgelegt von
Ina Alexandra Schneider
aus Schweinfurt

im Jahr 2017

Die Arbeit wurde von Prof. Dr. Christoph Strunk angeleitet.
Das Promotionsgesuch wurde am 07.07.2016 eingereicht.
Das Kolloquium fand am 16.05.2017 statt.

Prüfungsausschuss:	Vorsitzender:	Prof. Dr. Tilo Wettig
	1. Gutachter:	Prof. Dr. Christoph Strunk
	2. Gutachter:	Prof. Dr. Ferdinand Evers
	weiterer Prüfer:	Prof. Dr. Sergey Ganichev

Contents

CHAPTER 1

Introduction

The superconductor-insulator transition in disordered thin films such as polycrystalline films of TiN is a topic that is still under intense debate. In the ongoing discussion several scenarios are considered. A concept that is strongly supported by accumulating experimental evidence [1, 2, 3, 4] is the Josephson junction array as a model system for disordered films. It is believed that due to strong fluctuations an electronic granularity prevails in the films that may lead to the formation of self organized superconducting islands. These islands are embedded into an insulating matrix so that the system forms a randomly arranged natural Josephson junction array. The artificially fabricated counterpart to this system are well known mesoscopic devices that are subject of an intensive, both theoretical and experimental work [5, 6, 7, 8]. Two energy scales play an important role in Josephson junction networks: Firstly the Josephson coupling energy which is connected to the tunneling of Cooper pairs and favors a superconducting inductive behavior. Secondly the charging energy which is the energy that is necessary to add an electron and which favors an insulating capacitive behavior.
In the framework of this thesis micro and nanostrips were patterned out of TiN thin films. The samples were subject of a characterization of the electronic properties at low temperatures and high magnetic fields. The main motivation for our work was the question about the consequences of an electronic fragmentation, i.e., a self organized Josephson junction array emerging in TiN films, when we go to samples with a width in the range of

a few tens of nanometers, i.e., quasi one-dimensional wires. On the basis of the addressed model system we may expect that our films undergo a transition from a two-dimensional to a one-dimensional natural network. As regards the artificial device field, two-dimensional Josephson junction arrays have already been studied intensively and the observations give a first expectation and serve as a comparison to our results [9]. One of the prime elements in the understanding of quasi one-dimensional superconducting systems is the loss of global phase coherence by quantum phase slips. The process is rather well understood for one-dimensional artificial arrays of Josephson junctions but less clear for nanowires fabricated from disordered films.
A popular motivation for the research on Josephson junctions and related systems can be found in the possible application of these systems for the realization of qubits. Normal computers depend on conventional transistors. In today's microprocessors up to billions of them are placed on one single chip with the size of about one square centimeter which is then called an integrated circuit. The field of electronics made an amazing progress during the last decades when it comes to the shrinking of the structure sizes. The number of transistors packed into integrated circuits increased constantly. However computers are facing increasingly tough demands while at the same time a physical limit is set to the miniaturization of chip structures. At a certain point quantum mechanical effects like for example the tunneling of charge carriers come into play. On the one hand these effects interfere with a limitless downsizing of transistors but on the other hand they open up the possibility for new types of computers that rely on quantum mechanical processes. In such quantum computers the ordinary bits are replaced by qubits which on contrary may not only store the values 0 and 1 but an infinite number of values in between the ground state $|0\rangle$ and the excited state $|1\rangle$ in form of a superposition. To realize quantum computers it is therefore necessary to find suitable quantum mechanical two-level systems. One of the possible candidates are Josephson junctions [10, 11, 12, 13, 14]. A charge qubit can be realized by a gate capacitor that is coupled to a Josephson junction. Easily speaking the state of a charge qubit is determined by the number of Cooper pairs, i.e., bound electron pairs that have tunneled through the junction.

The structure of this thesis is as follows: Chapter 2 introduces the relevant concepts necessary to explain and classify the experimental results of this work. We start with the introduction of the most important theories on superconductivity. Subsequently we want to discuss the physics of Josephson junctions in different limits as well as suitable model concepts that allow for a better understanding of the dynamics of this system. We address the meaning of charge and phase as dual quantum variables and the role of this duality in the framework of Josephson physics. In the last part of the theory chapter the

superconductor-insulator transition which can for example be observed in polycrystalline two-dimensional TiN films is characterized.
Chapter 3 covers the experimental field starting with the precise introduction of the wafer material and the fabrication methods that were applied for the processing of TiN microstructures and nanowires. We further explain the measurement and cryostat setup that was employed for the measurements of the electric transport properties of our samples at low temperatures.
In chapter 4 the measurement results are presented and analyzed. The first two sections are dedicated to the superconducting and insulating states of the structures patterned onto a first chip named D03-wd. The last section deals with the results obtained for another chip called D03-sar2.
Chapter 5 sums up the results of this thesis and gives an outlook to future work.
In the two abstract chapters the precise recipe for the preparation of micro and nanosamples from TiN thin films can be found as well as the detailed instructions that lead through the fitting routines applied in this work.

CHAPTER 2

Theoretical Background

2.1. A Short Introduction to Superconductivity

In this section, we briefly explore the basic phenomena of superconductivity and the theoretical background. The London equations, the BCS theory and the Ginzburg-Landau theory as important milestones in the history of superconductivity will be introduced. Unless stated differently, the books of Tinkham [15], Buckel [16], Hunklinger [17] and Kittel [18] served as sources for the information collected in the following. Since within the limits of this work we can only give a very brief insight into this very wide and complex topic, the reader is referred to these books for a deeper understanding.
Superconductivity is characterized by the absence of electrical resistivity [19] when the material is cooled below a certain temperature called critical temperature T_c. Besides that, superconductors display a number of other remarkable characteristics, for example the partial or complete expulsion of an external magnetic field, known as the Meissner effect [20]. One distinguishes between two types of superconductors depending on their characteristic behavior in the presence of a magnetic field. Type I superconductors show a full Meissner effect meaning that the magnetic field is repelled from the interior of the material as long as the field strength is smaller than a temperature dependent critical value $B_c(T)$. Superconductors in this so called Meissner state exhibit a perfectly diamagnetic behavior. In contrast type II superconductors experience an intermediate state between two temperature

dependent critical fields $B_{c_1}(T)$ and $B_{c_2}(T)$. This state is also referred to as Shubnikov phase after L. Shubnikov who was the first one to experimentally observe the mixed state and the appearance of two critical fields in superconductors in 1935 [21]. In the Shubnikov phase the magnetic flux penetrates the material in form of quantized vortices, often referred to as fluxons. The mutually repelling vortices arrange in a regular triangular lattice. This regular array was predicted in 1957 by A. A. Abrikosov in his theoretical work on the mixed state and is called Abrikosov vortex lattice [22].

2.1.1. London Equations

After the discovery of perfect conductivity by H. Kamerlingh Onnes in 1911 [19] and perfect diamagnetism by W. Meissner and R. Ochsenfeld in 1933 [20] scientists worked on finding theoretical descriptions and explanations for the observed phenomena. Already in 1935 a successful phenomenological approach was made by the brothers F. and H. London [23]. They derived the first London equation

$$\frac{\partial \vec{j}_s}{\partial t} = \frac{n_s e^2}{m}\vec{E} = \frac{1}{\mu_0 \lambda^2}\vec{E} \tag{2.1}$$

with the supercurrent density $\vec{j}_s$ and

$$\lambda = \sqrt{\frac{m}{\mu_0 n_s e^2}} \tag{2.2}$$

from the simplified picture that a certain density of electrons n_s in the superconductor experiences no scattering which allows for the negligence of the corresponding term in the description of the electron motion $m(d\vec{v}/dt) = e\vec{E} - m\vec{v}/\tau$ in the standard Drude model. On closer inspection and taking into account Maxwell's equations, the London brothers demonstrated that time-varying magnetic fields are screened on the characteristic length scale λ. By using the second London equation

$$\nabla \times \vec{j}_s = -\frac{n_s e^2}{m}\vec{B} = -\frac{1}{\mu_0 \lambda^2}\vec{B} \tag{2.3}$$

which can not be formally derived and again applying Maxwell's equations they were able to show that also time-independent magnetic fields are screened in this same distance. The London equations therefore allow for an explanation of the Meissner effect. It can be demonstrated that a magnetic field parallel to the surface of a bulk superconductor

decreases exponentially in its interior as

$$B(x) = B(0)e^{-x/\lambda} \tag{2.4}$$

with x being the distance to the surface. The parameter λ is called the London penetration depth.

2.1.2. BCS Theory

In 1956 L. N. Cooper was able to demonstrate that any attractive interaction between two electrons causes the ground state of the Fermi gas to become unstable since the overall energy of the system is lowered by the formation of bound electron pairs, the so called Cooper pairs [24]. Since the two electrons that form a Cooper pair possess opposite momenta and spins they couple to an integer spin and show a bosonic character. Therefore the Cooper pairs may condense in the same quantum state which is characterized by a single macroscopic wave function $\psi(\vec{r}) = \psi_0(\vec{r})e^{i\varphi(\vec{r})}$. The mechanism that leads to the attractive interaction between the electrons is initially of no importance. Nevertheless, a possible origin of it could already be given in detail in 1950/51 by H. Fröhlich [25] and J. Bardeen [26] independently from one another. The isotope effect (described by E. Maxwell in 1950 [27]), the fact that $T_c \propto M^{-\alpha}$, where M is the isotopic mass and α a material dependent value, suggested that the mechanism of interaction is carried out via the crystal lattice, i.e., the ion cores. This mechanism works in the following way: when an electron approaches a positive ion core, it feels attractive Coulomb interaction. Consequently, the ion core is set in motion and the lattice gets distorted and thus polarized. A second electron now experiences an attraction to this polarization and thereby to the first electron.
Based on a weak attractive interaction process between the electrons, J. Bardeen, L. N. Cooper and J. R. Schrieffer developed their famous microscopic theory of superconductivity, the BCS theory, in 1957 [28]. Many pages could be filled with this complex theory but we rather mention the most important conclusions of it at this point. The BCS theory predicted the existence of an energy gap Δ, meaning that a minimum energy $E_g = 2\Delta(T)$ is necessary to break a Cooper pair and to create two quasi-particle excitations. It was demonstrated that this energy gap reaches a value

$$\Delta(0) = 1.764\, k_B T_c \tag{2.5}$$

at zero temperature and drops to zero at T_c with the dependence

$$\Delta(T) \approx 1.74\,\Delta(0)\sqrt{1-(T/T_c)^2} \qquad T \approx T_c \tag{2.6}$$

near T_c. The BCS theory also predicts the Meissner effect and the dependence of the penetration depth as a function of temperature correctly.

2.1.3. Ginzburg-Landau Theory

Because of its phenomenological origin, the Ginzburg-Landau (GL) theory which was proposed already in 1950 [29], initially received little attention. However it is of great importance since the microscopic BCS theory hits its boundaries when the energy gap Δ is not a constant in space. Especially with regard to the description of type II superconductors the more macroscopic GL theory becomes indispensable.
Within the Landau theory, a theory about second-order, i.e., continuous phase transitions [30], V. L. Ginzburg and L. D. Landau treated the macroscopic wave function $\psi(\vec{r}) = \psi_0(\vec{r})e^{i\varphi(\vec{r})}$ of the superconducting state as a complex order parameter. $|\psi(\vec{r})|^2$ is the local density of superconducting electrons n_s. When deriving the GL theory from the BCS theory, as demonstrated by L. P. Gor'kov in 1959 [31], it turns out that the order parameter is directly proportional to the gap parameter Δ:

$$\psi(\vec{r}) = \Delta(\vec{r})e^{i\varphi(\vec{r})}. \tag{2.7}$$

Gor'kov also showed that the GL theory is a limiting form of the BCS theory which is valid near T_c and that ψ can be interpreted as the wave function of the center-of-mass motion of the Cooper pairs.
The GL theory follows a thermodynamical approach and assumes that the thermodynamical Gibbs free energy can be expressed by a series expansion in powers of ψ and $\nabla\psi$ and expansion coefficients α and β. Applying a variational principle, one obtains the differential equation

$$\frac{1}{2m^*}\left(\frac{\hbar}{i}\nabla - \frac{e^*}{c}A\right)^2\psi + \beta|\psi|^2\psi = -\alpha(T)\psi \tag{2.8}$$

where $e^* = 2e$ and $m^* = 2m_e$ and $\vec{A}(\vec{r})$ is the vector potential. The corresponding equation for the supercurrent is given by

$$\vec{J}_s = \frac{e^*\hbar}{i2m^*}\left(\psi^*\nabla\psi - \psi\nabla\psi^*\right) - \frac{e^{*2}}{m^*c}|\psi|^2\vec{A}. \tag{2.9}$$

Based on these equations, the GL theory introduces the GL coherence length

$$\xi_{GL}(T) = \frac{\hbar}{|2m^*\alpha(T)|^{1/2}} \tag{2.10}$$

which is a characteristic length describing the distance over which $\psi(\vec{r})$ can vary without an undue increase of energy. The ratio of the London penetration depth and the GL coherence length is called the GL parameter κ which is given by

$$\kappa = \frac{\lambda}{\xi_{GL}}. \tag{2.11}$$

This parameter is almost independent of the temperature around T_c since λ and ξ_{GL} show almost the same temperature dependence in this range.
In typical superconductors, λ is much smaller than ξ_{GL}, so that $\kappa \ll 1$. One can prove that in this case, a positive surface energy in connection with a domain wall between normalconducting and superconducting material exists. In 1957, A. A. Abrikosov investigated the case of $\xi < \lambda$ which should in contrast to the reverse case lead to a negative surface energy [22]. He was able to show that at $\kappa = 1/\sqrt{2}$, a change from positive to negative surface energy occurs and demonstrated that this leads to a rigorous change of the properties of the material. He found that in case of $\kappa > 1/\sqrt{2}$, the magnetic flux continuously penetrates the material between two critical magnetic fields B_{c1} and B_{c2} in a regular pattern of flux tubes. Abrikosov called these kinds of superconductors type II superconductors and thereby predicted a state of matter that was not experimentally observed until years later.

2.2. The Dynamics of Josephson Junctions

In the following chapter we want to discuss the basic properties of Josephson junctions and the physical phenomena that are observable in these systems. The relevant energy scales defining the junction behavior will be addressed and the tilted washboard potential as a mechanical analog for the phase dynamics of Josephson junctions will be introduced. The last section deals with the Ivanchenko-Zil'berman theory which allows to model the behavior of small tunnel contacts under the influence of thermal noise.

2.2.1. Josephson Effects and the Relevant Energy Scales

In section 2.1 we saw that the superconducting state is characterized by a macroscopic wave function $\psi(\vec{r}) = \psi_0(\vec{r})e^{i\varphi(\vec{r})}$. When two superconductors with charge numbers n_1 and

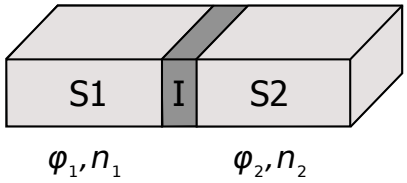

Figure 2.1.: Schematic of a Josephson junction consisting of two superconductors separated by a thin insulator allowing the two wave functions to overlap. S1 and S2 are specified by their number of Cooper pairs $n_{1,2}$ and the phases of their wave functions $\varphi_{1,2}$. The superconducting electrodes may also be separated by any other type of weak link like a normal metal or a geometric constriction.

n_2 and wave function phases φ_1 and φ_2 are separated by a barrier thin enough so that their wave functions can overlap, a flow of a supercurrent between the electrodes without any voltage drop can be observed due to the coherent quantum mechanical tunneling of Cooper pairs. The barrier can be formed by an insulator, a normal metal or a any type of geometric constriction forming a so called weak link between the two superconducting electrodes. The device is called Josephson junction (see figure 2.1).
The resulting supercurrent, i.e., the current that flows across the junction without any dissipation is given by

$$I_s = I_c \sin \varphi. \tag{2.12}$$

Here I_c is the maximum supercurrent that the particular junction can sustain and $\varphi = \varphi_1 - \varphi_2$ is the phase difference of the wave functions describing the superconducting states in the two electrodes. This observation is called the dc Josephson effect and was predicted by B. D. Josephson in 1962 [32]. He also predicted the time evolution of the phase difference φ in presence of a voltage drop V across the junction as

$$\frac{d\varphi}{dt} = \frac{2eV}{\hbar} = \frac{2\pi V}{\Phi_0}. \tag{2.13}$$

Integrating equation 2.13 and inserting φ into equation 2.12 shows that an alternating current of amplitude I_c is flowing with the Josephson frequency

$$f = \frac{2eV}{h} = \frac{V}{\Phi_0}. \tag{2.14}$$

This is referred to as the ac Josephson effect [15]. A detailed derivation of the two Josephson relations can be found in [33]. Since $2e/h = 483.6\,\mathrm{GHz/mV}$, the characteristic Josephson frequency is typically found in the microwave regime in experiments. Taking the time derivative of equation 2.12 and inserting the time evolution of the phase $d\varphi/dt$ from equation 2.13 yields

$$\frac{dI_s}{dt} = I_c \cos\varphi \frac{2eV}{\hbar} = I_c \cos\varphi \frac{2\pi V}{\Phi_0}. \tag{2.15}$$

A comparison to the conventional expression $U = L(dI/dt)$ for the inductance shows that the Josephson junction behaves like a nonlinear inductor [34] with the Josephson inductance given by

$$L_J = \frac{\hbar}{2eI_c}\frac{1}{\cos\varphi} = \frac{\Phi_0}{2\pi I_c}\frac{1}{\cos\varphi} = L_{J0}\frac{1}{\cos\varphi} \tag{2.16}$$

with

$$L_{J0} = \frac{\hbar}{2eI_c} = \frac{\Phi_0}{2\pi I_c}. \tag{2.17}$$

Remarkably, the Josephson inductance L_J is negative in the intervals $\pi/2 + 2\pi n < \varphi < 3\pi/2 + 2\pi n$ and becomes large for $\varphi \to \pi/2 + n\pi$ with n being an integer number.
In the following we want to take a look at the characteristic energy scales that determine the behavior of the junction. Clearly for a junction in the superconducting state without any voltage drop there will be no energy dissipation. However, a certain energy is stored in the junction arising from the overlap of the two wave functions of the electrodes. For a better idea of this energy we can imagine a Josephson junction with zero current flowing. Increasing the current I_s in time will involve an increase of the phase difference φ according to the current-phase relation (see equation 2.12) which in turn will lead to a voltage drop according to the voltage-phase relation (see equation 2.13). To determine the energy stored in the junction we have to integrate the power given by the product of the Josephson current $I_s(t)$ and the voltage $V(t)$:

$$U_J = \int_0^{t_0} (I_c \sin\tilde{\varphi}) \left(\frac{\Phi_0}{2\pi}\frac{d\tilde{\varphi}}{dt}\right) dt. \tag{2.18}$$

We assume that the phase difference at $t = 0$ is equal zero and reaches φ at $t = t_0$. Then we arrive at

$$U_J = \frac{\Phi_0 I_c}{2\pi}\int_0^{\varphi} \sin\tilde{\varphi}\, d\tilde{\varphi} \tag{2.19}$$

and obtain

$$U_J = \frac{\hbar I_c}{2e}(1 - \cos\varphi) = \frac{\Phi_0 I_c}{2\pi}(1 - \cos\varphi) = E_J(1 - \cos\varphi) \tag{2.20}$$

with

$$E_J = \frac{\hbar I_c}{2e} = \frac{\Phi_0 I_c}{2\pi}. \tag{2.21}$$

E_J is called the Josephson coupling energy which is proportional to the critical current. To demonstrate the relation to the Josephson inductance we can also express it in the form

$$E_J = \frac{\hbar^2}{4e^2 L_{J0}}. \tag{2.22}$$

The Josephson coupling energy is a measure for the coupling strength of the junction and favors a superconducting behavior. The necessary energy to increase the current by accelerating the Cooper pairs and change the phase difference is provided by the external current source.
There is a second characteristic energy which on contrary favors an insulating behavior of the junction, namely the energy of the electric field between the superconducting electrodes given by

$$U_C = \frac{CV^2}{2} = \frac{Q^2}{2C} = \frac{(2en)^2}{2C} = E_C \left(\frac{Q}{e}\right)^2 = E_C(2n)^2 \tag{2.23}$$

where n is the total number of Cooper pairs on one electrode.

$$E_C = \frac{e^2}{2C} \tag{2.24}$$

is called the charging energy and is inversely proportional to the capacitance which is defined by the geometry of the Josephson junction. It describes the energy that is necessary to add one extra electron.
The charging energy and the Josephson coupling energy are determined by the junction's capacitance and inductance, respectively. They can be considered as competing energy scales with the ratio E_J/E_C defining the behavior of the junction. We can also regard the problem from a quantum mechanical point of view. A detailed derivation for the Hamiltonian of a Josephson junction can be found in [35]. The phase operator $\widehat{\varphi}$ and the number operator $\widehat{n}$ are then quantum mechanical conjugate variables with the commutation relation $[\widehat{\varphi}, \widehat{n}] = i$ and the Heisenberg uncertainty relation $\Delta\varphi\Delta n \geq 1/2$ or $\Delta\varphi\Delta Q \geq e$ applies [36, 37]. In the picture of competing energy scales the observation of the insulating state means that the charging energy wins over the Josephson coupling energy. Quantum mechanically a Coulomb-blockaded state arises since the exchange of charges, i.e., Cooper pairs is forbidden. In this situation, the number of Cooper pairs is well defined and the phase difference between the electrodes is uncertain. On contrary we find the junction in the superconducting state when the phase difference is well defined allowing for an uncertain number of charges that manifests in a high rate of Cooper pair tunneling.

2.2.2. RCSJ Model and the Tilted-Washboard Potential

An ideal Josephson junction is characterized well by the relations presented in the previous section. A more detailed description of the realistic junction is given by the RCSJ (resistively and capacitively shunted junction) model developed by W. C. Stewart [38] and D. E. McCumber [39] in 1968 which includes the quasi-particle tunneling and capacitive

effects [15]. This model depicts the physical Josephson junction in an equivalent circuit as an ideal junction in a parallel configuration with a capacitor C and an ohmic resistor R (see figure 2.2(a)). The ideal junction part obeys the current-phase relation in equation 2.12 for I_s and represents the superconducting channel of the arrangement. The resistor accounts for the dissipative quasi-particle tunnel current I_r arising in the presence of a voltage V and the capacitive element originates from the geometric capacitance of the junction as addressed before. It contributes to the total current by the displacement current I_d. We can therefore express the total, i.e., bias current as

$$I_B = I_s + I_r + I_d = I_c \sin\varphi + \frac{V}{R} + C\,\frac{dV}{dt}. \tag{2.25}$$

Replacing the voltage in favor of the phase according to the voltage-phase relation given in equation 2.13 yields

$$I_B = I_c \sin\varphi + \frac{\hbar}{2e}\frac{1}{R}\frac{d\varphi}{dt} + \frac{\hbar}{2e}C\,\frac{d^2\varphi}{dt^2}. \tag{2.26}$$

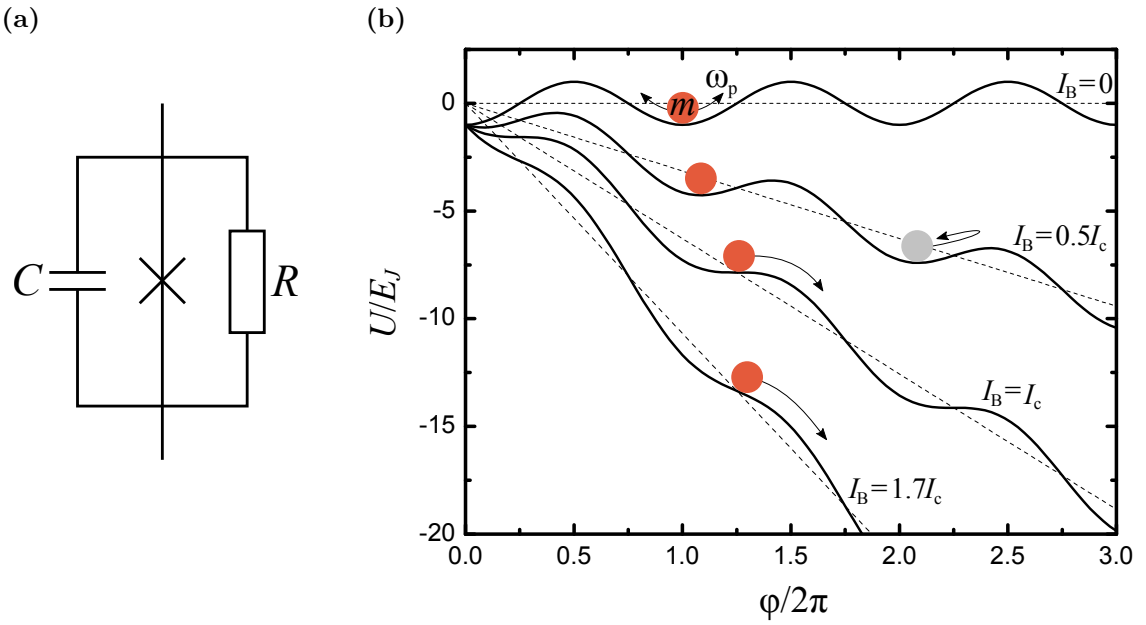

Figure 2.2.: (a) Equivalent circuit of a physical Josephson junction in the RCSJ model: an ideal junction is shunted by a capacitor C and a resistor R. **(b)** Tilted-washboard potential: a particle of mass m and coordinate φ moves in a cosine-potential with a tilt proportional to the total current I_B through the junction. As soon as the particle can move downwards in the potential and along the φ-coordinate, a voltage appears according to the voltage-phase relation 2.13 ($I_B \geq I_c$). Upon decreasing I the particle may be caught at a certain retrapping current $I_r \leq I_c$ which depends on the mass of the particle and the damping of the system (gray particle).

Multiplying by $\hbar/2e$ and considering the expression 2.21 for the Josephson coupling energy in the $\sin\varphi$ - term we obtain the numerically solvable differential equation

$$\left(\frac{\hbar}{2e}\right)^2 C\,\frac{d^2\varphi}{dt^2} + \left(\frac{\hbar}{2e}\right)^2 \frac{1}{R}\frac{d\varphi}{dt} + \frac{d}{d\varphi}\left(-E_J\cos\varphi - \frac{\hbar I_B}{2e}\varphi\right) = 0 \tag{2.27}$$

which on closer inspection gives a mechanical analog for the RCSJ model. It resembles the equation of motion

$$m\frac{d^2x}{dt^2} + \eta\frac{dx}{dt} + \frac{d}{dx}U = 0 \tag{2.28}$$

for a particle of mass $m = (\hbar/2e)^2\,C$ moving along the φ-axis in an effective potential

$$U(\varphi) = -E_J\cos\varphi - \frac{\hbar I_B}{2e}\varphi = -E_J\left(\cos\varphi + \frac{I_B}{I_c}\right) \tag{2.29}$$

and the speed of the particle corresponds to the voltage across the junction. The motion is damped by a viscous drag force $(\hbar/2e)^2\,(1/R)\,d\varphi/dt$. The particle oscillates with a small amplitude in a minimum of the potential at the plasma frequency

$$\omega_p = \frac{1}{\tau_p} = \frac{1}{\sqrt{L_J C}} = \left(\frac{2eI_c}{\hbar C}\right)^{1/2} = \left(\frac{2\pi I_c}{\Phi_0 C}\right)^{1/2}. \tag{2.30}$$

The second term in equation 2.29 leads to a tilt of the $-E_0\cos\varphi$ - function proportional to the total current I_B and the resulting potential looks like a tilted washboard as sketched in figure 2.2(b). At zero total current through the junction the cosine-function runs horizontally and the particle of mass m resides at a minimum of the potential, oscillating at the plasma frequency ω_p. Since the particle does not change its coordinate φ we find the junction in a zero voltage state according to the voltage-phase relation given in equation 2.13. When the current is increased, the cosine-function gets tilted and at a current $I_B = I_c$ the minima disappear so that the particle may start to move downwards in the potential along φ. This means that the phase coordinate changes in time which leads to a voltage drop across the junction. When we decrease the current the particle can be caught again in a minimum at a certain retrapping current $I_r \leq I_c$. The particle movement, i.e., the change of φ is stopped and the junction enters the zero voltage state again. I_r is defined by a competition between the particle mass m which is proportional to the junction capacitance C and the damping of the system which is proportional to $1/R$. A large capacitance means a large mass in the tilted-washboard model which leads to a higher kinetic energy of the particle. As a result, the retrapping current will be comparably small since the particle will not be caught in a minimum until the tilt is small enough so that it cannot overcome the maxima anymore. On the other side, a strong damping, i.e., small R leads to a higher retrapping current since it reduces the kinetic energy of the particle. To characterize the phase dynamics

of a junction, Stewart and McCumber introduced the dimensionless Stewart-McCumber parameter

$$\beta_c = \frac{2\pi}{\Phi_0} I_c R^2 C \tag{2.31}$$

where the influence of mass and damping, i.e., capacitance and resistance are merged. We refer to the phase dynamics of the junction as overdamped for $\beta \ll 1$ and as underdamped for $\beta \gg 1$. [15, 40]

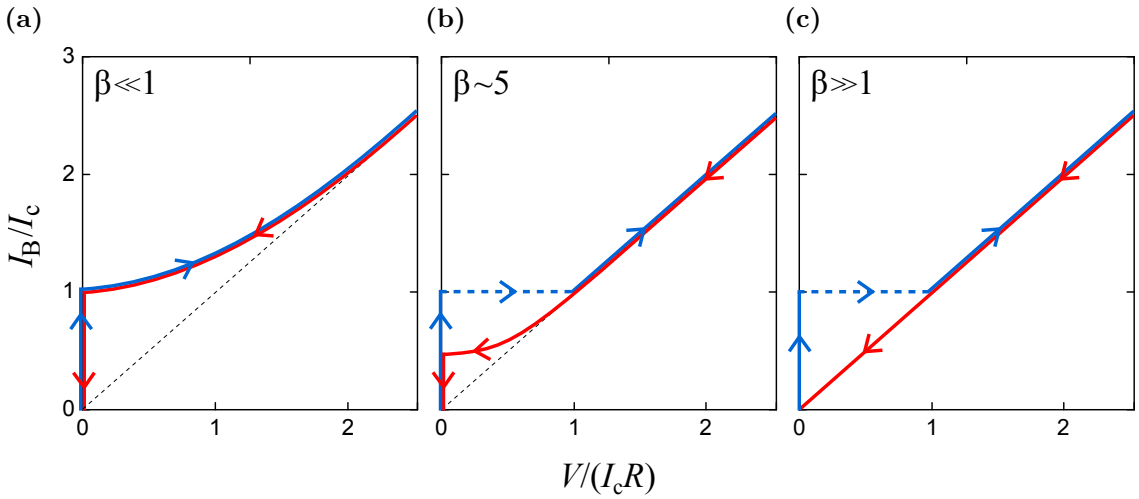

Figure 2.3.: Current-voltage characteristics of **(a)** an overdamped ($\beta \ll 1$, small capacitance and/or resistance), **(b)** a weakly damped ($\beta \sim 5$) and **(c)** an underdamped ($\beta \gg 1$, large capacitance and/or resistance) Josephson junction.

Three examples of current-voltage characteristics for an overdamped, a weakly damped and an underdamped junction are presented in figure 2.3. For $\beta \ll 1$ we find the junction in the overdamped regime (small capacitance and/or resistance, see figure 2.3(a)). As soon as the current exceeds I_c the particle in the washboard model starts to move along φ slowly due to the strong damping corresponding to a slow voltage increase. On contrary in the underdamped case (large capacitance and/or resistance, see figure 2.3(c)) the particle is immediately accelerated to an average velocity causing a voltage jump from zero to a finite value. When the current is decreased in an overdamped junction, the particle is slowed down when I_c is approached and stops immediately as soon as minima reappear in the potential at $I_B = I_c$. As a result, the voltage slowly goes back to zero and the current-voltage characteristic is non-hysteretic. On the underdamped side the kinetic energy is large due to the large mass of the particle and/or the weak damping so that the potential has to be brought back into the horizontal position before the particle will stop to move. This means that zero voltage will not be reached until the current is decreased to $I_B = 0$ and we observe a hysteretic behavior. The weakly damped Josephson junction

(see figure 2.3(b)) also behaves hysteretically. The current must be decreased to a certain extent below I_c before the particle is slowed down and finally retrapped in a minima so that the junction slowly reenters the zero voltage state. The corresponding retrapping current that was already mentioned above is given by

$$I_r = \frac{4I_c}{\pi Q} \tag{2.32}$$

where Q is the so called quality factor which can also be expressed as

$$Q = \beta_c^{1/2}. \tag{2.33}$$

The retrapping current formula can be derived from a consideration of the energy that a particle in the tilted-washboard potential dissipates between two maxima and the kinetic energy gained in the same time (for the derivation see [15]).

2.2.3. Finite Temperatures and the Ivanchenko-Zil'berman Theory

Up to now we did not include any thermal fluctuations in our considerations which is appropriate as long as k_BT is much smaller than the barrier height $2E_J$ [15]. Within the RCSJ model we can include current contributions I_f from noise sources like thermal fluctuations, shot noise and $1/f$ noise by adding an additional term in equation 2.25:

$$I_B = I_s + I_r + I_d + I_f. \tag{2.34}$$

Hence for the potential arising from equation 2.27 and expressed in equation 2.29 we obtain

$$U(\varphi) = -E_J \cos\varphi - \frac{\hbar I_B}{2e}\varphi + \frac{\hbar I_f}{2e}\varphi = -E_0 \left(\cos\varphi + \frac{I_B}{I_c} - \frac{I_f}{I_c}\right). \tag{2.35}$$

For the tilted-washboard potential sketched in figure 2.2(b) this results in an additional random tilt allowing the particle to escape over a neighboring maximum involving a phase slip by $\pm 2\pi$. As long as the washboard-potential runs horizontally, i.e., no external current is applied, thermal fluctuations will cause the particle to escape to the left and to the right with equal probability and consequently the resulting average voltage will remain zero [8]. When a current is applied in an underdamped or a weakly damped junction, thermal fluctuations lead to a reduced critical current since the particle may escape and gain velocity prematurely already before I_c is reached. The junction abruptly switches to the normal state then. In contrast thermal fluctuations can help retrapping the particle and hence an increased retrapping current I_r can be observed. Escaping and retrapping of the particle are stochastic processes which is why a distribution of both values can be observed.

In the overdamped regime thermal fluctuations will also allow the particle in the tilted-washboard to escape into the next minimum involving a phase slip of 2π. However, due to the heavy damping the particle is going to settle there instead of proceeding its motion like in the underdamped case. As a result it will move over the barriers continuously in a diffusive process with a finite average velocity. This process leads to a randomly spaced series of voltage pulses in time. Consequently the resulting averaged voltage will remain finite even below the critical current I_c. The current-voltage characteristics are rounded at low voltages and a reduced critical current will be observed [41].
The problem of a small junction with uniformly distributed current in the strong damping regime in the presence of thermal noise was treated almost simultaneously by V. Ambegaokar and B. I. Halperin (published in 1969) [42] and by Yu. M. Ivanchenko and L. A. Zil'berman (published in 1968) [43, 44] with the same approach and the same solution.[1] They assumed the current $I_f(t)$ to be a Markov process and therefore deployed the Fokker-Planck equation equivalent to expression 2.34 that they were able to solve analytically. For the Cooper pair current they derived the expression

$$I(V_{B_{IZ}}) = I_0 \,\mathrm{Im}\left[\frac{\mathcal{I}_{1-i\beta\hbar V_{B_{IZ}}/2eR_B}(\beta E_J)}{\mathcal{I}_{-i\beta\hbar V_{B_{IZ}}/2eR_B}(\beta E_J)}\right]. \tag{2.36}$$

$\mathcal{I}_\nu(z)$ is the modified Bessel function with argument z and complex order ν. $\beta = 1/k_BT$ is the inverse temperature. Equation 2.36 uses the notation of Steinbach et al. [47].[2] R_B is a resistance in series to the junction and $V_{B_{IZ}}$ the total bias voltage. The voltage drop V_{IZ} across the junction can therefore be obtained by a recalculation $V_{IZ} = V_{B_{IZ}} - R_B I$.[3] The notation I_0 is used in order to clarify that we do not speak about the actual observable critical current but about its theoretical maximum, i.e, intrinsic value. We will also stick to this notation. Exemplary curves as yielded within the Ivanchenko-Zil'berman model are sketched in figure 2.4 for several values of βE_J.
A comparison of the curves displayed in figure 2.3(a) and those in figure 2.4 illustrates that thermal fluctuations lead to the observation of a supercurrent peak with suppressed critical current instead of a supercurrent branch. Steinbach et al. [47] were the first ones to experimentally observe this supercurrent peak in 2001 even though it has been predicted

[1] When Ambegaokar and Halperin published their findings in June 1969 [42] they referred to an earlier publication by Ivanchenko and Zil'berman from August 1968 on the same topic [45, 46] and pointed out their own different and more precise approach. In an erratum to their publication from August 1969 they write that their attention has been drawn to a second paper of Ivanchenko and Zil'berman from December 1968 [43, 44] which they did not know before.

[2] We corrected a mistake that appears in the publication of Steinbach et al. in equation (1) in the indexes of the Bessel functions. The correct expression becomes clear when the function is derived from the work of Ivanchenko and Zil'berman.

[3] We added the index "IZ" to the voltage variables V_B and V as they were used by Steinbach et al. [47] with regard to a later disambiguation when applying the theory to our experiment.

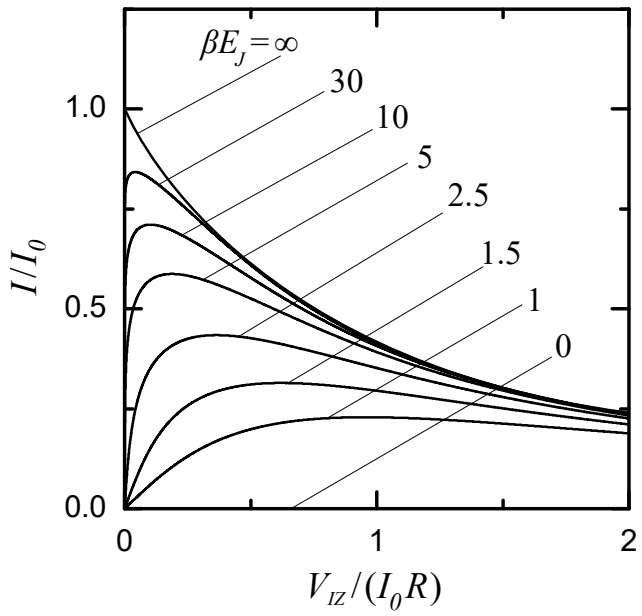

Figure 2.4.: Current-voltage characteristics as derived by Ivanchenko and Zil'berman for small tunnel contacts for several values of βE_J. A supercurrent peak is observed instead of a supercurrent branch.

more than 30 years earlier. In their experiment they voltage biased an ultrasmall tunnel junction and measured the average current through the junction by a current meter in series.

2.3. Charge-Phase Duality

Alternatively to the competition of Josephson coupling energy and charging energy we already briefly considered the behavior of a Josephson junction within the framework of the uncertainty relation between phase and charge in section 2.2.1. Based on these quantum mechanical conjugate variables one can establish a dual model to the observations on Josephson junctions and their dynamics. Within the context of this thesis, the dual model to overdamped small tunnel contacts, i.e., the state of phase diffusion as described in the previous section is of particular importance. Initially we want do discuss the striking exact duality between a Josephson junction and a so called phase slip junction where the tunneling of Cooper pairs is the dual process to the tunneling of magnetic flux.

2.3.1. Phase-Slip Junction as the Dual Element to a Josephson Junction

Based on the fact that charge and phase are dual variables in a superconductor, J. E. Mooij and Yu. V. Nazarov published theoretical work in 2006 where they investigated the tunneling of magnetic flux through a narrow superconducting wire [48]. As the Meissner effect (see section 2.1) describes, a superconductor expels magnetic flux. The process therefore involves a phase slip: a temporary change of the phase by 2π between two superconducting regions in the wire. The order parameter locally fluctuates to zero before the superconducting state is reestablished. Mooij and Nazarov demonstrated that a coherent quantum phase slip in such a system is the exact dual to the coherent tunneling of Cooper pairs of charge $2e$ in a Josephson junction. The two dual physical systems are opposed in figure 2.5.

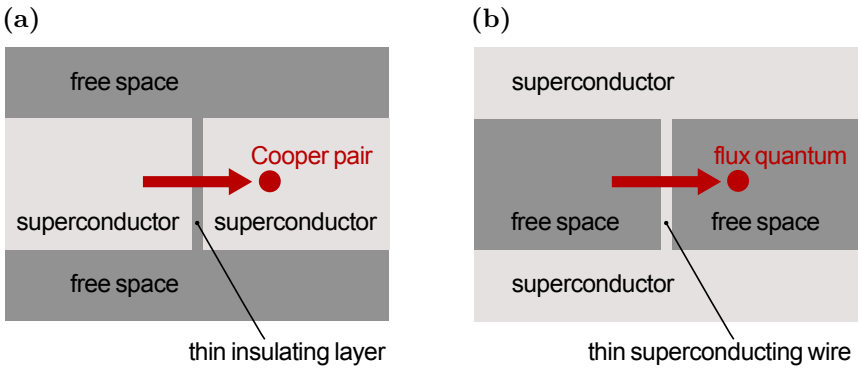

Figure 2.5.: In a Josephson junction **(a)** Cooper pairs can tunnel between two superconductors through an insulating barrier. In its dual element, the phase slip junction **(b)**, flux quanta may tunnel through a thin superconducting wire and the phase locally slips by 2π. Based on [49].

Since 2006 various publications have dealt with possible experimental implementations and realizations, materials and devices based on duality considerations [50, 51, 52, 53]. However, in the years after the publication of Mooij and Nazarov no one was able to experimentally demonstrate the occurrence of coherent quantum phase slips across a superconductor. The breakthrough was achieved in 2012 by O. V. Astafiev and his colleagues [54] with the observation of coherent quantum phase slips in an InO_x wire that was embedded in a larger superconducting loop. They exposed the device to microwave frequencies and tuned the magnetic flux through the loop. A band gap in the energy curves of the two flux states became visible due to the tunneling of flux quanta through the wire to avoid the quantum mechanically forbidden occupation of the same energy level. The experiments were performed at ultra-low temperatures where the influence of thermal fluctuations is negligibly small. The quantum nature of the phase slips was particularly proven since superposition states of flux quanta having crossed and having not crossed the superconducting wire were observed.

The uncertainty relation between charge and phase $\Delta\varphi\Delta Q \geq e$ or $\Delta\varphi\Delta n \geq 1/2$ with n being the number of Cooper pairs with charge $2e$ has the following meaning in the context of the duality between the two described systems: in a Josephson junction the phase is a good quantum number and well defined while the charge is poorly defined. On contrary we find the reverse situation in a phase slip junction: the phase fluctuates and the number of Cooper pairs in the junction is fixed giving rise to a Coulomb blockade of Cooper pairs and a zero current state which is the electrodynamic dual to the dc Josephson effect (see equation 2.12). As the dual effect to the ac Josephson effect (see equation 2.13) Bloch oscillations of the voltage can be observed in quantum phase slip junctions. By synchronizing them to an external microwave signal one can in principle induce current Shapiro steps in contrast to the voltage Shapiro steps occurring in Josephson junctions. The roles of current and voltage are interchanged in the two dual systems. [48, 55, 56]

(a)

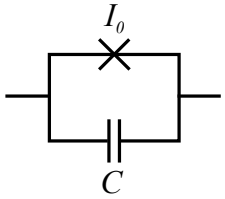

$$
\begin{aligned}
I &= I_0 \sin\varphi + C(\hbar\,/\,2e)\ddot{\varphi} \\
V &= (\hbar\,/\,2e)\dot{\varphi} \\
U &= E_J(1-\cos\varphi) + C(\hbar\,/\,2e)^2\,\dot{\varphi}^2\,/\,2 \\
I_0 &= (2e\,/\,\hbar)E_J \\
E_C &= 4e^2\,/\,2C
\end{aligned}
$$

(b)

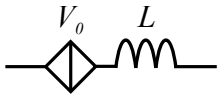

$$
\begin{aligned}
V &= V_0 \sin(2\pi Q\,/\,2e) + L\ddot{Q} \\
I &= \dot{Q} \\
U &= E_S\,\{1-\cos(2\pi Q\,/\,2e)\} + L\dot{Q}^2\,/\,2 \\
V_0 &= 2\pi E_S\,/\,2e \\
E_L &= (h/2e)^2\,/\,2L
\end{aligned}
$$

Figure 2.6.: Duality between **(a)** a Josephson junction and **(b)** a QPS junction. The dual element to a capacitance in parallel is an inductance in series. Phase and charge are dual variables in the two systems. Based on [55].

The full duality between a Josephson junction and a QPS (quantum phase slip) junction is depicted in figure 2.6. A voltage biased QPS junction in series with an inductance is the dual circuit to a current biased capacitively shunted Josephson junction. A Cooper pair tunneling through a Josephson junction obtains an additional phase factor $\exp(\pm i\varphi)$ and the coupling energy is given by $U_J = E_J(1-\cos\varphi)$ (see equation 2.20). In the dual picture of the QPS junction a flux quantum picks up a charge factor $\exp(2\pi iQ/2e)$ when tunneling over the superconductor. Analog to the coupling energy this leads to a QPS energy $U_S = E_S\{1-\cos(2\pi Q/2e)\}$ with E_S being the QPS amplitude. The QPS amplitude defines the critical voltage $V_0 = 2\pi E_S/2e$ in analogy to the critical current $I_0 = (2e/\hbar)E_J$ which is defined by the Josephson coupling energy (see equation 2.21). However we have to

be aware that these are only approximations for the limiting cases $E_S \gg E_L$ and $E_J \gg E_C$ respectively. Precise calculations that include the ratio of the energy scales have been performed by A. B. Zorin and can be found in [57]. The total energy is given by the Josephson coupling energy plus the capacitive term $C(\hbar/2e)^2\dot{\varphi}^2/2$ in case of the Josephson junction and the QPS energy plus the inductive term $L\dot{Q}^2/2$ in case of the QPS junction. The total current in the Josephson junction is given by $I = I_0 \sin\varphi + C(\hbar/2e)\ddot{\varphi}$ which is the derivative of the energy with respect to the phase. In analogy we find the total voltage in the QPS junction to be $V = V_0 \sin(2\pi Q/2e) + L\ddot{Q}$ as the derivative of the energy with respect to the charge. Dual to the tilted-washboard potential for a particle moving along the phase coordinate this corresponds to a particle moving along the charge coordinate [58]. In the first case the particle is trapped in a potential minimum and the system is in the zero voltage state as long as the current does not exceed the critical current. The QPS junction is in the dual zero current state which emerges as long as the voltage does not exceed the critical voltage. Dual to the charging energy $E_C = 4e^2/2C$ which favors the insulating state of the Josephson junction and brings it to the charging regime for $E_C \gg E_J$ we find the QPS junction in the superconducting inductive regime when the inductive energy $E_L = (h/2e)^2 \,/\, 2L$ sufficiently exceeds the QPS amplitude E_S.[4] [48, 55]

2.3.2. The Energy Band Picture

The duality can also be regarded in terms of the Bloch wave description of the Coulomb-blockaded Josephson junction. D. V. Averin, A. B. Zorin and K. K. Likharev [59, 60] used the Hamilton operator

$$\mathcal{H} = \frac{Q^2}{2C} + U_J(\varphi) = E_C \frac{\partial^2}{\partial\varphi^2} - E_J \cos\varphi. \tag{2.37}$$

in order to describe a single Josephson junction.[5] Here Q is the charge on the junction electrode, C the capacitance of the Josephson junction, E_J the Josephson coupling energy and φ the phase difference across the junction. This Hamiltonian is analog to the one for particles in a periodic potential, e.g., the electrons in a crystal lattice:

$$\mathcal{H} = \frac{\hat{p}^2}{2m} + V(\vec{r}) = -\frac{\hbar^2}{2m}\nabla^2 + V(\vec{r}). \tag{2.38}$$

[4] Unlike the common textbook convention $U_C = E_C(2n)^2$ with $E_C = e^2/2C$ used in equation 2.23 and 2.24 we change to the now more convenient definition $U_C = E_C n^2$ with $E_C = 4e^2/2C$ as used in the cited references where E_C gives the energy necessary to add one Cooper pair instead of one electron. n is the number of Cooper pairs. In analogy we have $U_L = E_L n^2$ with n being the number of flux quanta.

[5] Unlike [59] we again stick to the convention $U_C = E_C n^2$ with $E_C = 4e^2/2C$.

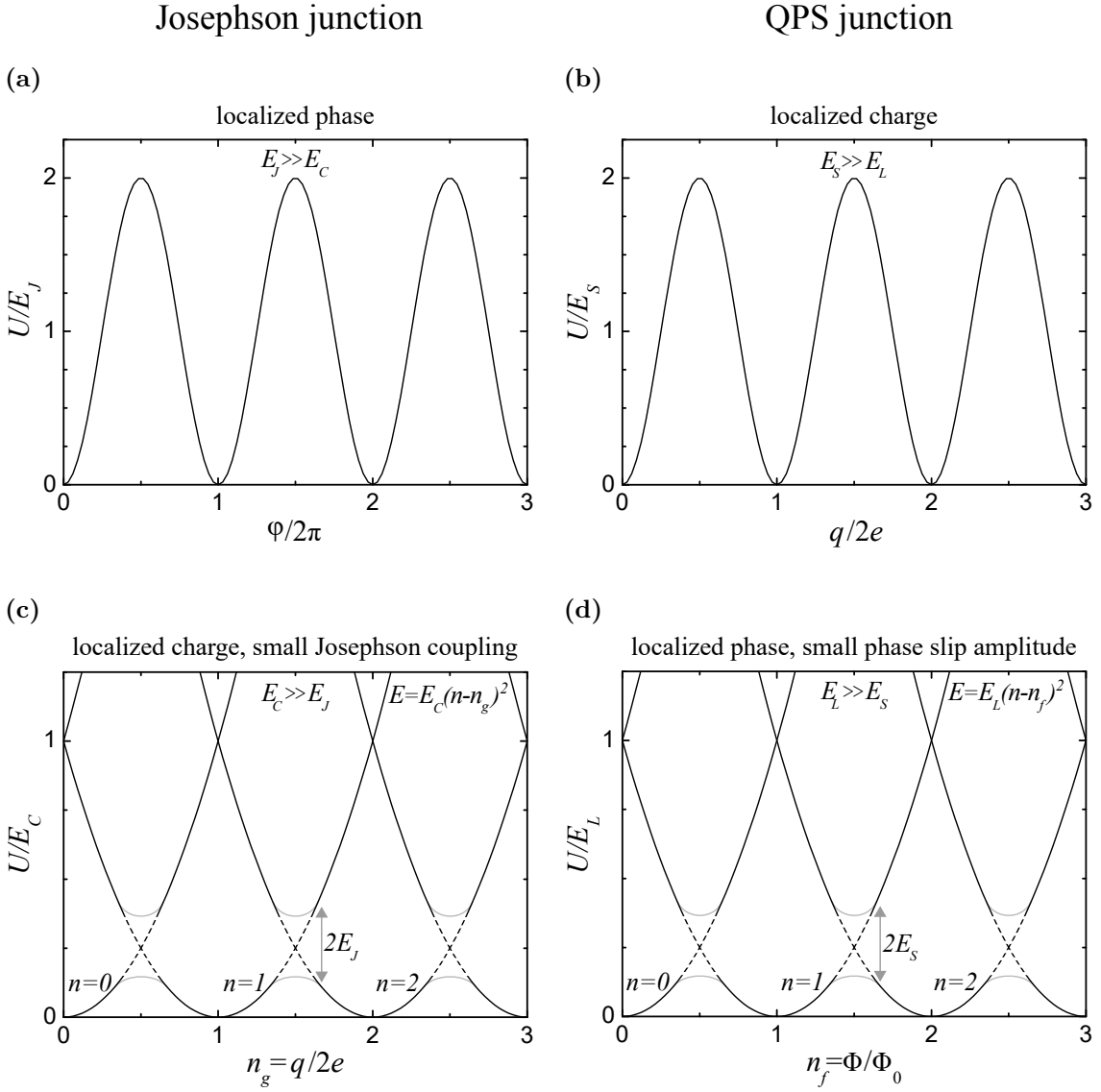

Figure 2.7.: Duality of the energy bands of Josephson junction and QPS junction. In a Josephson junction a crossover from **(a)** superconducting inductive to **(c)** insulating capacitive behavior is observed when E_C exceeds E_J. In analogy a crossover from the insulating capacitive regime **(b)** to the superconducting inductive regime **(d)** in a QPS junction occurs when E_L exceeds E_S. Based on [55]

The energy of the Josephson junction is periodic with respect to the phase and the comparison of the two Hamiltonians shows that the phase φ in the Josephson junction plays the same role as the coordinate $\vec{r}$ of the electron in the crystal lattice. Furthermore $(\hbar/2e)^2C$ is analog to the mass and $(\hbar/2e)Q$ is analog to the momentum [59]. The resulting wave functions are of the type $\psi(\varphi) = u_n(\varphi)\exp(i\varphi q/2e)$ [61] where q is given by the current through the junction as $q = \int I(t)dt$. A comparison to the wave functions of a particle in a periodically-repeating environment $\psi(\vec{r}) = u_{\vec{k}}(\vec{r})\exp(i\vec{k}\vec{r})$ shows that for the Josephson junction q is equivalent to the crystal momentum or quasi-momentum $\hbar\vec{k}$. In analogy it is therefore called quasi-charge. Just like the situation for electrons in the periodic potential of a crystal lattice the Josephson junction exhibits a Bloch band energy spectrum. The eigenvalues $E_n(q)$ are periodic with respect to q with a period of $2e$ and the first Brillouin zone extends over the range $-e \leq q \leq e$. Further phenomena connected to the Bloch character of the Josephson junction will be discussed later on in this section.

We want to apply the duality aspects of Josephson and QPS junction to the Bloch picture now. The energy as a function of $\varphi/2\pi$ for a Josephson junction in the superconducting inductive regime where $E_J \gg E_C$ is displayed in figure 2.7(a). The dual diagram as a function of $q/2e$ for a QPS junction in the insulating capacitive regime with $E_S \gg E_L$ is opposed in figure 2.7(b). The Josephson junction undergoes a transition to the insulating charging regime for $E_C \gg E_J$ (see figure 2.7(c)) while the QPS junction is driven into the superconducting inductive regime for $E_L \gg E_S$ (see figure 2.7(d)). The energy dependence of the Josephson junction is now dominated by the charging energy which depends parabolically on the induced normalized charge $n_g = q/2e$. The parabolas appear periodically. At the charge degeneracy points showing up at half integer values of n_g a level splitting equal to $2E_J$ arises due to the avoided crossing of the parabolas. The dual situation is found for the QPS junction. The energy is given by periodically emerging parabolas as defined by the inductive energy E_L as a function of the applied normalized flux $n_f = \Phi/\Phi_0$. At the flux degeneracy point a gap of $2E_S$ is induced and the energy diagram is split up into multiple bands. Figure 2.7 depicts the strict duality between Josephson and QPS junction. We also see that the QPS junction for $E_S \gg E_L$ and the Josephson junction for $E_C \gg E_J$ share the quasi-charge as the relevant quantum number. Vice versa for the QPS junction in the regime of $E_L \gg E_S$ and the Josephson junction at $E_J \gg E_C$, the phase is the relevant quantum variable. [48, 55]

When a constant bias current is applied a Josephson junction with $E_C \gg E_J$ will stay in its lowest energy band E_0 as long as the charge is increased adiabatically, i.e., at sufficiently small bias currents. It is following adjacent parabolas and performs so called Bloch oscillations in analogy to the oscillations of charge carriers in a solid under the influence of a periodic potential with an applied electric field. From the energy-charge relation depicted in figure 2.7(c) one can obtain the voltage-charge relation by taking the

derivative of the lowest energy band $V = dE_0/dq$ with respect to the charge. Qualitative solutions depending on the ratio E_J/E_C are shown in figure 2.8. In the case of $E_J \ll E_C$ the dependence of the voltage on the charge is described by a sawtooth-like behavior. This corresponds to a charging of the junction which is terminated by the tunneling of a single Cooper pair. As a result a jump in the voltage is observed. When E_J and E_C are of the same magnitude, the dependence can be approximated by a function proportional to $\sin(2\pi q/2e)$. It was already mentioned in section 2.3.1 that Bloch oscillations of the voltage can be observed in a QPS junction as the equivalent effect to the ac Josephson effect of the current in a Josephson junction. The fact that Bloch oscillations show up in a Josephson junction in the capacitive regime also becomes clear within the framework of duality.

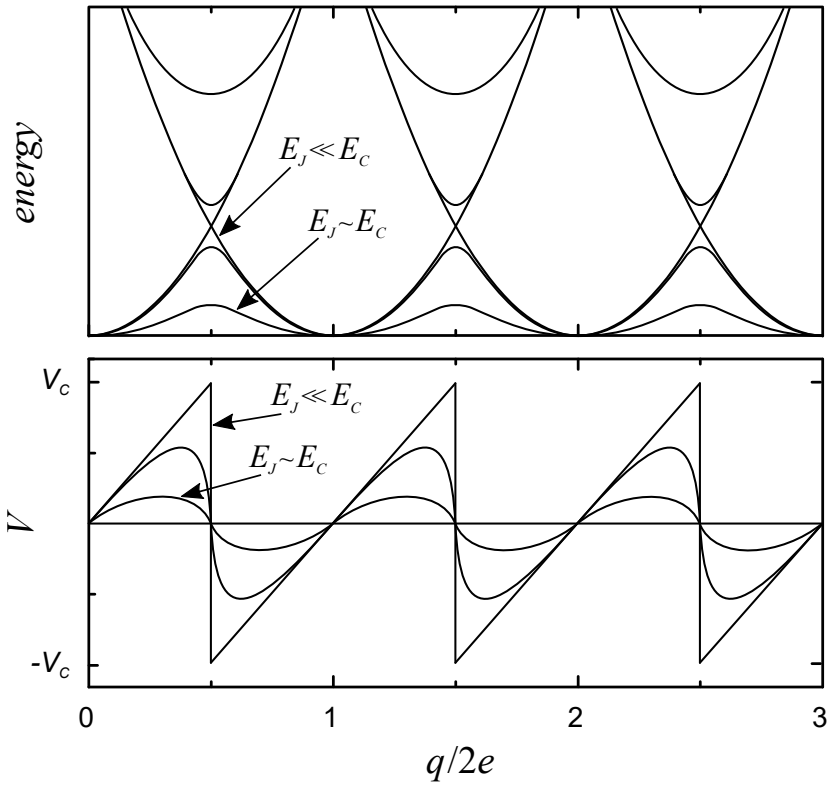

Figure 2.8.: Voltage as a function of quasi-charge in a Josephson junction. The evolution with the ratio of E_J/E_C together with the corresponding energy diagrams is demonstrated qualitatively.

In the current-voltage characteristics, the Bloch oscillation regime manifests as a region with negative differential conductance dI/dV where the voltage decreases while the current increases. This region follows the blockaded regime where a tunneling of Cooper pairs in unfavorable. The following so called Bloch nose arises because the quasi-charge is repeatedly driven to the boundary of the Brillouin zone, i.e., $q = e$ where it jumps to

$q = -e$ accompanied by the tunneling of a Cooper pair. Hereby the voltage is effectively decreased, resulting in the Bloch nose. At higher currents the system favors jumps from one band to the other band and the voltage starts to increase again. The gap between the bands is overcome by this so called Zener tunneling. An example for the resulting current-voltage characteristic is plotted in figure 2.9.

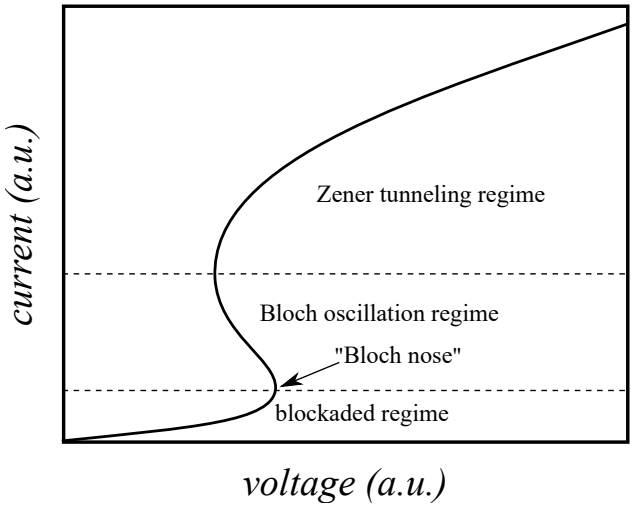

Figure 2.9.: Exemplary current-voltage characteristic of a Josephson junction with $E_C \gg E_J$. At sufficiently large current a Bloch nose appears and a region with a negative differential conductance where the voltage decreases while the current increases develops in the Bloch oscillation regime. Based on [61].

Dual to the appearance of voltage Shapiro steps in superconducting Josephson junctions, i.e., Josephson junctions with classical phase dynamics as presented in section 2.2.1 and 2.2.2, it should be possible to observe current Shapiro steps in QPS junctions and Josephson junctions in their capacitive regimes. For that purpose it is necessary to phase-lock the Bloch oscillations to an RF signal of frequency f. Consequently plateaus of constant current should be observable in the current-voltage characteristics at values $I_n = n2ef$ in dual to the familiar and well examined voltage Shapiro steps at constant values of the voltage $V_n = n\Phi_0 f$. This would give rise to a precise new definition of the current standard. An experimental realization is difficult though. Di Marco et al. [62] treated the problem of a QPS junction in a realistic resistive and inductive environment theoretically with an analytical and numerical approach in order to specify the origin of the obstacles that have to be overcome in the experiment. They found that the steps in the current-voltage characteristics are strongly smeared due to charge fluctuations that are induced by the environment. However in the nineties spikes were observed in the dV/dI curves of ultrasmall Josephson junctions as a function of current [63, 64, 65] which can be interpreted as a signature of Bloch oscillations as they were predicted in 1985 [59, 60].

2.3.3. Dual Ivanchenko-Zil'berman Relation

The duality relations presented in the previous sections easily allow for the derivation of the dual form to the Ivanchenko-Zil'berman current-voltage relation presented in section 2.2.3. By substituting $I \to V$, $V_{B_{IZ}} \to I_{B_{IZ}}$, $I_0 \to V_0$, $1/R \to R$, $E_J \to E_S$ and $2e \to \Phi_0$ we obtain

$$V(I_{B_{IZ}}) = V_0 \,\mathrm{Im}\left[\frac{\mathcal{I}_{1-i\beta e I_{B_{IZ}} R_B/\pi}(\beta E_S)}{\mathcal{I}_{-i\beta e I_{B_{IZ}} R_B/\pi}(\beta E_S)}\right]. \tag{2.39}$$

The relation can also be derived analytically based on the Langevin equation of the quasi-charge [59, 60, 66]. Again $\mathcal{I}_\nu(z)$ is the modified Bessel function with argument z and complex order ν and $\beta = 1/k_B T$ the inverse temperature. As also can be derived from duality arguments, R_B is a resistance in parallel to the junction and the current through the junction I_{IZ} therefore can be recalculated from the bias current $I_{B_{IZ}}$ as $I_{IZ} = I_{B_{IZ}} - V/R_B$.[6]

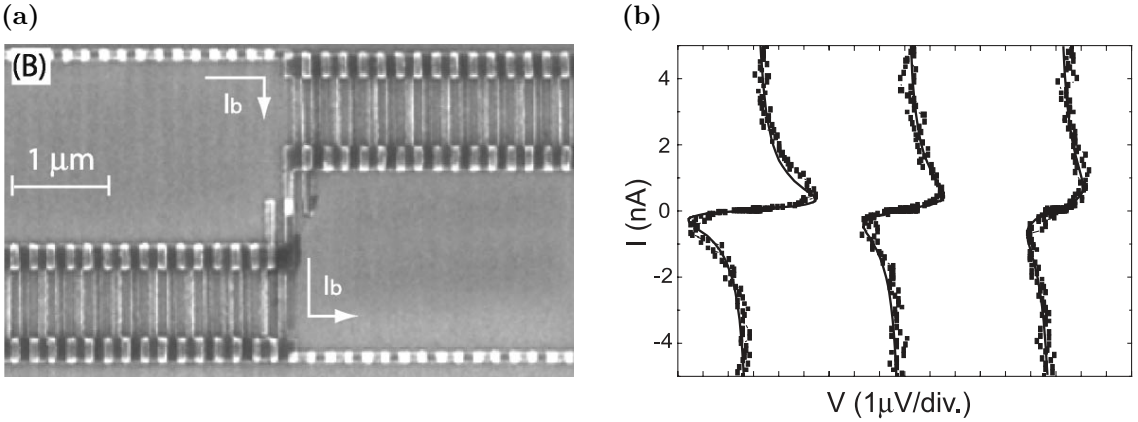

Figure 2.10.: (a) SEM image of the $Al/AlO_x/Al$ single junction configuration embedded in a high impedance SQUID-array environment as investigated by Corlevi et al. [67]. **(b)** Current-voltage characteristics obtained for this configuration (squares). The fits (solid lines) correspond to the dual Ivanchenko-Zil'berman relation. The noise temperature was introduced as a fit parameter. From left to right the data corresponds to a noise (and cryostat) temperature of $T = 160\,\mathrm{mK}$ (50 mK), 250 mK (260 mK), 400 mK (300 mK). From [67].

The Ivanchenko-Zil'berman theory describes the behavior of a junction in the overdamped phase regime under the influence of thermal noise. Due to duality arguments the dual form corresponds to the regime of overdamped quasi-charge dynamics, i.e., underdamped phase dynamics. In 2006 researchers successfully modeled the current-voltage characteristics obtained for a single $Al/AlO_x/Al$ junction embedded in a high impedance SQUID-array

[6] As we did in section 2.2.3, we added the index "IZ" to the current variables I_B and I with regard to a later disambiguation when applying the theory to our experiment.

environment (see figure 2.10(a)) [67]. Their data and the fits obtained from the dual Ivanchenko-Zil'berman relation is shown in figure 2.10(b). As a fit parameter they used an effective temperature that exceeds the set cryostat temperature.

2.4. Superconductor-Insulator Transition

One of the astonishing features that can be observed in two-dimensional superconducting films is the superconductor-insulator transition (SIT). The nature of this quantum phase transition is still not fully understood and under intense debate. Generally speaking, the community distinguishes between two basic types of transitions: fermionic and bosonic scenarios depending of what is happening at the transition point. In the first case the modulus of the order parameter becomes zero. In the latter case it is assumed that electron pairs exist on both sides of the transition. Therefore the modulus of the order parameter may not become zero but the amplitude of the fluctuations of the order parameter's phase reaches a critical value [68].

2.4.1. Disorder- and Magnetic-Field-Driven SIT

In 1989, an SIT was reported for amorphous bismuth thin films deposited onto germanium underlayers [69]. The corresponding data is shown in figure 2.11(a). The different curves display the behavior of several films varying in their thickness and correspondingly in their resistance at room temperature. On the y-axis the sheet resistance $R_\square = R/\text{number of squares} = R/(l/w)$ with l and w being the length and width of the samples is plotted. It is observed that above a certain critical thickness, in this case 6.73 Å, the film switches abruptly from an insulating to a superconducting behavior. For thicker films, the transition temperatures are found at increasingly higher values. The almost horizontal separatrix between the two families of curves processes very close to the quantum resistance of Cooper pairs $R_Q = h/4e^2 \approx 6.45\,\text{k}\Omega$ and the sheet resistance at room temperature can be considered as a control parameter for the SIT. The quantum resistance of Cooper pairs as a universal sheet resistance threshold for the onset of superconductivity was also observed in other investigations on granular metallic films [70] independent on other sample characteristics like for example the film thickness.
Another example for an SIT is presented in figure 2.11(b) (data from [1]). The $R(T)$ measurement was started with an untreated TiN thin film residing on the superconducting side with a transition temperature $T_c \approx 0.5\,\text{K}$ (curve S4). Subsequently the film was continuously disturbed by means of soft plasma etching (curve S3, S2,...) involving an

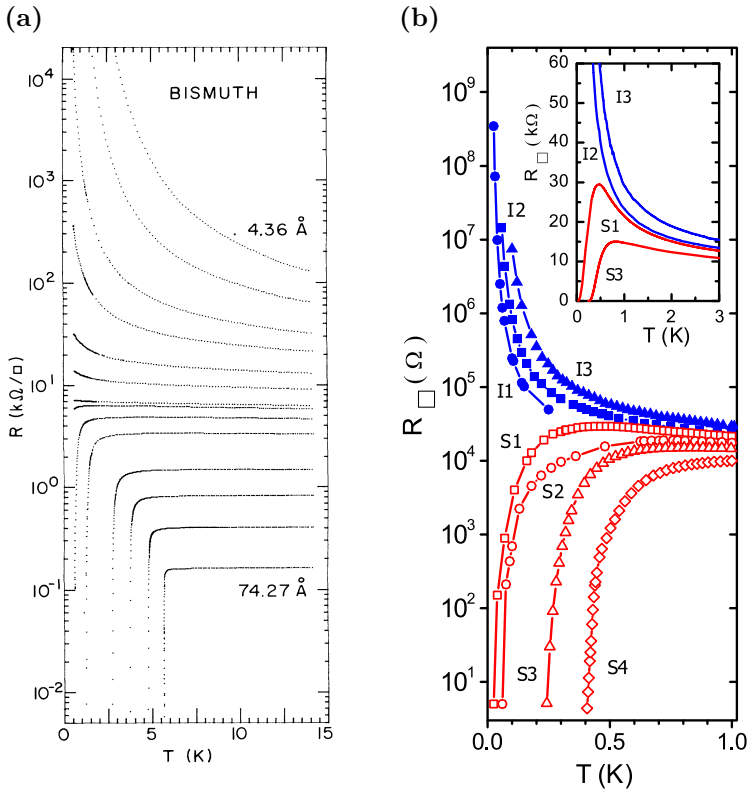

Figure 2.11.: (a) SIT in bismuth thin films varying in their thicknesses. After [69]. **(b)** SIT in a TiN thin film (initial state S4) where the disorder was increased continuously by soft plasma etching. After [1]. In both cases, the room temperature resistance of the particular film is an indicator for the behavior at low temperatures.

increase of the room temperature sheet resistance of the sample. At the same time, T_c progresses to smaller values until at some point the film shows a dramatic increase of the resistance at small temperatures instead of behaving superconducting (curve I1). Increasing the disorder of the film further leads to a continuously more pronounced insulating behavior. The transition from superconducting to insulating behavior occurs very sharply and no intermediate metallic state is observed. This kind of SIT is referred to as a disorder-driven superconductor-insulator transition (D-SIT). A D-SIT can be studied in various quasi two-dimensional material systems with different types of crystal structures like for example homogeneously disordered polycrystalline films (TiN) [1], granular films (Pb grains) [71] and amorphous films (InO_x) [72].

For weakly superconducting films there is another way to trigger the SIT which is by applying a magnetic field [73]. Hence, this is called the magnetic-field-driven superconductor-insulator transition (B-SIT). The resulting insulating state is identical to the one induced by disorder.

Although TiN and InO_x thin films exhibit different kinds of crystal structures, the SIT in the two systems is characterized by a strikingly similar behavior. An interesting feature that is observed in both films is the activated behavior of the insulating state at low temperature following an Arrhenius law $R \propto \exp(T/T_0)$. Typical for both materials is also a huge positive magnetoresistance at small fields.

2.4.2. Josephson Junction Array Model and Electronic Granularity

A model system which is often used for a theoretical description of the superconductor-insulator transition in thin disordered films is the two-dimensional Josephson junction array. It is composed of superconducting islands with each of them coupled to their nearest neighbors by weak links (see figure 2.12). The Josephson junction array has been studied intensely in both theoretical and experimental works [5, 7, 8, 74, 75]. Similar to the basic module of the array, the Josephson junction, the behavior of the network is again governed by the Josephson coupling energy E_J and the charging energy E_C as competing energy scales. Depending on the ratio of those energies, the array will be found in the superconducting or in the insulating state.

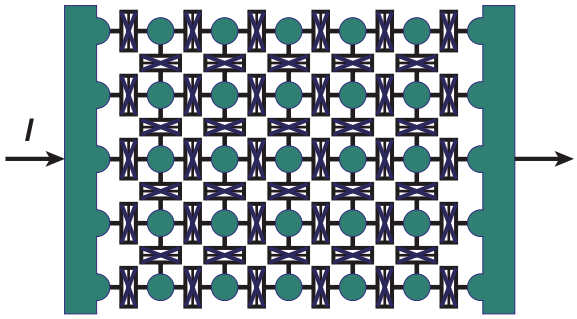

Figure 2.12.: Illustration of a two-dimensional Josephson junction array. Superconducting islands (green circles) are each connected to their nearest neighbors by weak links (crossed rectangles). From [76].

The use of Josephson junction networks as model systems for the behavior of disordered thin films is supported by corresponding scanning tunneling microscopy (STM) experiments. In 2008 STM measurements performed on TiN films at temperatures around $T = 50\,\mathrm{mK}$ revealed spatial inhomogeneities of the superconducting gap Δ (see figure 2.13) [2]. It was also observed that superconducting fluctuations exist well above the critical temperature T_c which gives rise to the idea that superconductivity plays an important role also within the insulating state. A commonly used term in that context is the Cooper pair insulator. Theoretical work based on disorder-induced electronic granularity is capable of explaining

various phenomena observed in disordered films, like for example the activated resistance of the insulating state and the huge positive magnetoresistance at small fields that was mentioned before [77, 78]. Besides it was predicted by numerical simulations that homogeneously disordered thin films may dissociate into superconducting islands embedded into an insulating sea [79, 80, 81]. This again invites for the idea of the Josephson junction network as a suitable model system.

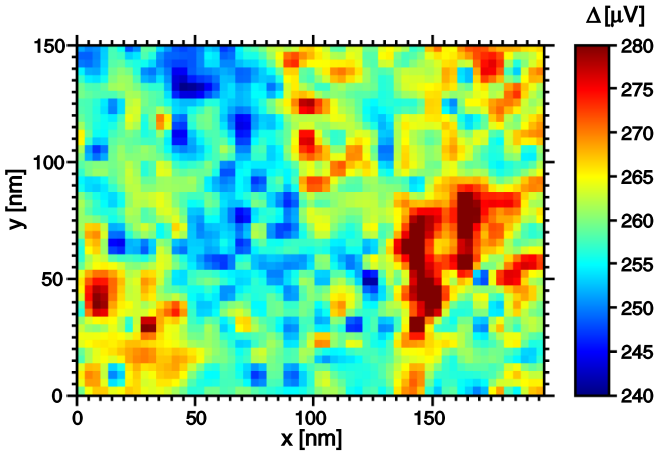

Figure 2.13.: Color map revealing the spatial fluctuations of the superconducting gap Δ in a TiN thin film with a thickness of 3.4 nm over an area of 200×150 nm. The characteristic scale of the observed inhomogeneities is about a few tens of nanometers. From [2].

In the following chapter when the film material is introduced it will be shown that TiN films display a polycrystalline structure with a typical size of the crystallites of about 5 nm. This might mislead to the conception that the structural inhomogeneities of the film are related to the electronic inhomogeneities. It is therefore important to mention that the two observations are not correlated but that the emerging electronic granularity results from a self-organization of the disordered film. The inhomogeneities of the superconducting gap appear on a scale which is about ten times larger than the scale of the topographic pattern of the film. Only recently STM investigations by C. Carbillet et al. on disordered NbN thin films directly demonstrated that there is no relation between film structure and electronic granularity [3]. The cross-correlation (see figure 2.14(c)) between the topographic map (see figure 2.14(a)) and the corresponding map of the superconducting gap variations (see figure 2.14(b)) at a temperature of $T = 300$ mK turned out to be flat displaying the absence of any correlation. Figure 2.14(d) shows the autocorrelation of the superconducting gap map which allows for the estimation of the typical size of the domains with a constant gap value (~ 50 nm) as well as for the typical distance between them (~ 100 nm). Again the size of the superconducting grains turns out to be about ten times larger than the scale of the topographic pattern.

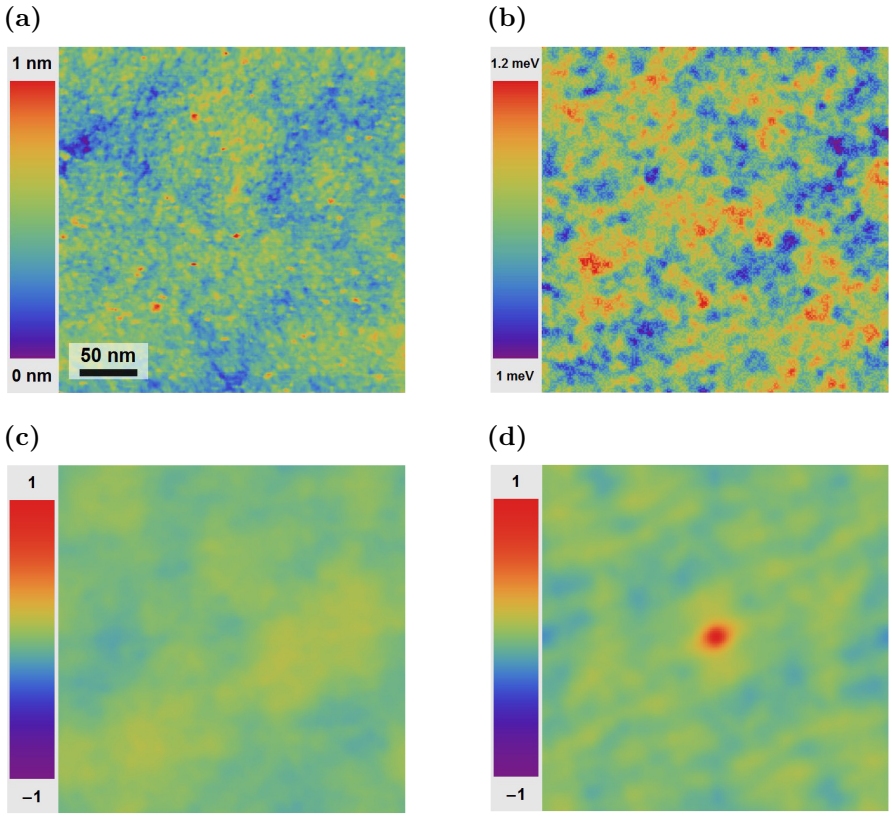

Figure 2.14.: **(a)** Topographic map of a NbN film. **(b)** Corresponding map of the superconducting gap fluctuations. **(c)** Flat cross correlation between (a) and (b) illustrating that there is no correlation between both. **(d)** Auto correlation of (b) allowing for the estimation of the superconducting grain size and the distance between the grains. From [3].

CHAPTER 3

Sample Processing and Experimental Methods

This chapter is intended to give an insight into the processing of micro and nanostrips from TiN thin films as a starting material. The film characteristics, the several sample fabrication steps as well as the detailed properties of the processed structures will be presented. Furthermore we regard the experimental methods which were applied for the electronic characterization of the samples. We briefly introduce the layout of the deployed dilution refrigerator which provides the necessary low temperatures and explore the physical concepts of its cooling mechanism. The last section of this chapter is dedicated to the measurement instrumentation part of the experimental setup.

3.1. Fabrication of TiN nanowires

In the following the reader is introduced to the film properties which is the starting point for the preparation of samples. Afterwards crosslinking of PMMA as a method to produce high-resolution structures down to the size of a few nanometers is presented. Unless stated differently, the proceedings compiled by Kelly and Weisbuch [82] as well as the book by Stepanova and Dew [83] served as sources for the collected information. In the last part the sample fabrication process is illustrated. Detailed preparation recipes including all necessary devices, materials, steps and parameters can additionally be found in appendix A.

3.1.1. Film Properties

The TiN film used for the preparation of micro and nanostructures was grown by Prof. Dr. Mikhail R. Baklanov onto a Si/SiO_2 wafer by atomic layer deposition (ALD) in Leuven, Belgium and is referred to as D03. The film shows a polycrystalline structure with a typical size of the crystallites of about 5 nm. This can be seen in the high-resolution transmission electron microscope (TEM) image shown in figure 3.1 which was taken by Prof. Dr. Tatyana Baturina in Novosibirsk, Russia. The film thickness is 3.6 nm. The untreated material shows a room temperature resistance of $R_{300} = 2.52\,\mathrm{k}\Omega$ and behaves superconducting with a critical temperature of $T_c = 1.29\,\mathrm{K}$ and a coherence length of $\xi_d(0) = 8.9\,\mathrm{nm}$. The charge carrier density was estimated to be $1.5 \cdot 10^{22}\,\mathrm{cm}^{-1}$. These and further parameters can be found in [84].

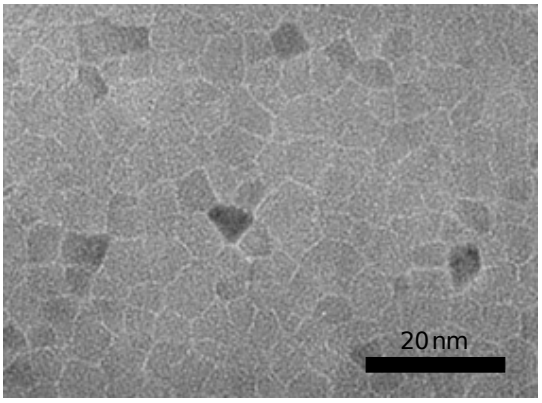

Figure 3.1.: High-resolution TEM image of a TiN film [85]. The film shows a polycrystalline structure with a typical size of the crystallites of about 5 nm. Their boundaries are clearly visible in the image as white lines.

3.1.2. Crosslinked PMMA as a High-Resolution Negative Resist

Electron beam lithography (EBL) is commonly the method of choice for the patterning of micro and nanostructures. A resist layer which is sensitive to the irradiation by electrons is deposited on top of the material and subsequently exposed to a computer-controlled focused electron beam. The irradiation changes the solubility properties of the resist so that in the following development process either the exposed (positive tone resist) or the non-exposed areas (negative tone resist) can be removed by a suitable chemical. Thus the material is prepared for the actual patterning step which can be subtractive (e.g., etching) or additive (e.g., material deposition).

A widely used positive tone resist for EBL is polymethyl methacrylate (PMMA) which consists of long polymer chains. The exposure to an electron beam leads to a scission of the molecules. The remaining fragments can then be dissolved and removed in a liquid developer, typically composed of methyl isobutyl ketone (MIBK) and isopropyl alcohol. For certain purposes (e.g., the subtractive processing of nanostrips) a negative EBL process is very utile. However, the application of most of the known negative tone resists involves certain difficulties, i.e., poor resolution, extremely high or low sensitivity to the process parameters, unstableness during processing or an expansion during the development process [86]. The use of PMMA as a negative tone resist avoids these challenges. In contrast to moderate doses of 50–500 $\mu C/cm^2$ leading to the breaking of polymer chains, high doses of more than 5000 $\mu C/cm^2$ (depending on the resist, the substrate and the structure size) cause a crosslinking of the polymer chains, i.e., the formation of larger molecules. The crosslinked PMMA is resistant to most solvents, which is why for example acetone and isopropyl alcohol can be used as developers to remove the unexposed PMMA [87]. This method allows for the fabrication of high resolution structures down to about 10 nm. Besides the easy handling, the fact that the crosslinking increases the PMMA's resistance to dry etching is beneficial [88] since it implicates the fact that a comparatively thin layer can be used to protect the material during the etching process which additionally increases precision.
In the context of this work, several fabrication tests have been performed before the actual sample preparation. The first step was to identify the necessary dose to obtain a satisfying degree of crosslinking in the PMMA. The development in acetone and isopropyl alcohol should not significantly affect the resist layer, i.e., its thickness should not decrease. By means of an atomic force microscope (AFM) this has been demonstrated to be the case at a dose of 30000 $\mu C/cm^2$ for the utilized PMMA 50K at 3 %. Its thickness both directly after the spin-coating and later after the development is about 35 nm. Furthermore it has been verified that this thickness is enough to protect the TiN film during the argon ion beam etching. It was found that the applied etching process removes approximately 10–15 nm of the crosslinked PMMA. This means that the TiN layer underneath the resist can be considered to remain unaffected by etching.

3.1.3. Sample Patterning

Before starting with the patterning, the wafers are cut into quadratic pieces with an edge length of 4.3 mm. The fabrication is subsequently divided into two parts: the application of metal contacts on top of a TiN film (see figure 3.2(a) - figure 3.2(f)) and the subtractive processing of a TiN strip between two opposing contacts (see figure 3.2(g) - figure 3.2(k)).

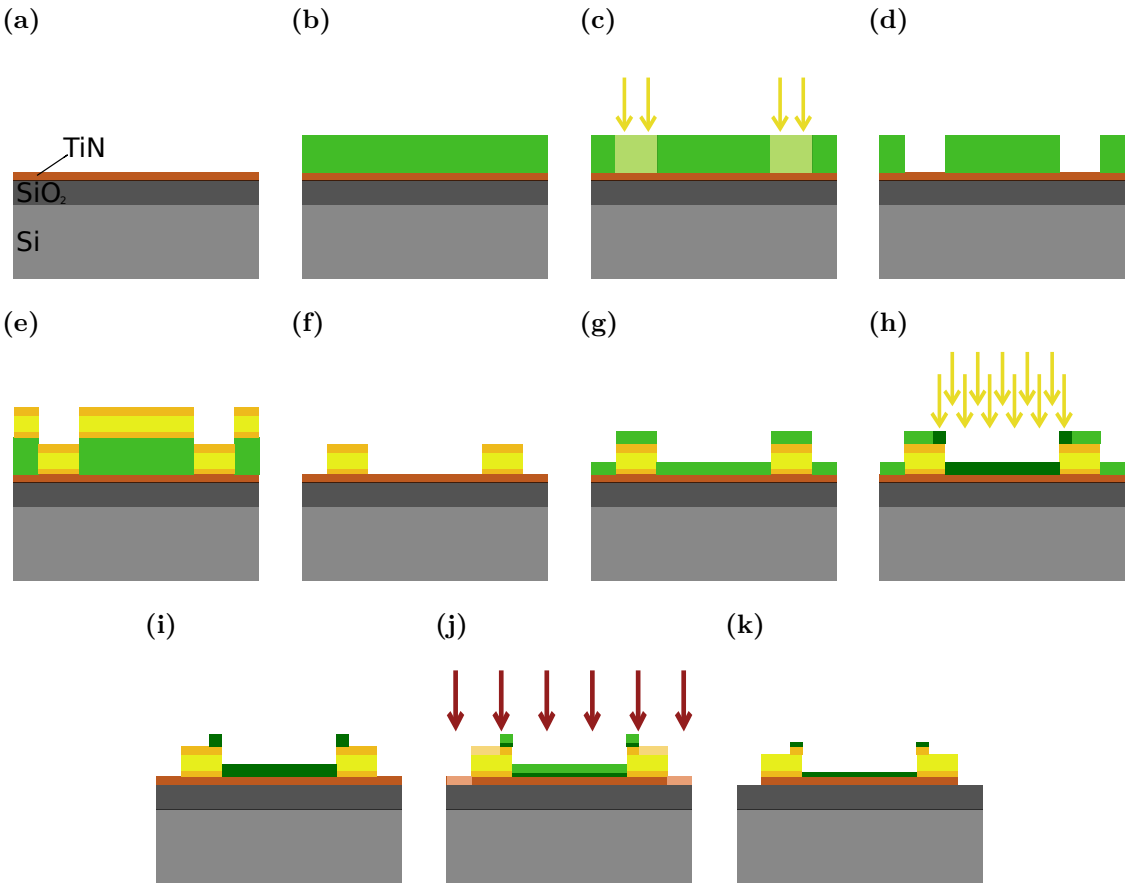

Figure 3.2.: The different steps of sample fabrication: **(a)** Untreated wafer. **(b)** Application of PMMA. **(c)** Electron-beam lithography. **(d)** Development of PMMA. **(e)** Deposition of a Ti-Au-Ti layer. **(f)** Lift-off. **(g)** Application of PMMA. **(h)** Crosslinking the PMMA by EBL. **(i)** Removing the non-crosslinked PMMA in a solvent. **(j)** Ion beam etching. **(k)** Finished sample.

At the beginning, the chip is coated with PMMA (see figure 3.2(b)) and the bonding pad and lead structures are drawn by means of an automated electron-beam lithography process (see figure 3.2(c)). The exposed areas of the resist can then be removed by means of a developer composed of MIBK and isopropyl alcohol (see figure 3.2(d)). In the following metal evaporation process a thin adhesion layer of titanium ($\sim 10\,\mathrm{nm}$) and a layer of gold ($\sim 120\,\mathrm{nm}$) are deposited onto the chip (see figure 3.2(e)). In order to protect the gold layer during the later etching process, a thin capping film of titanium ($\sim 16\,\mathrm{nm}$) is deposited on top. The thickness is chosen in such a way that the titanium just gets removed by etching. Gold is much less resistant to argon ion beam etching than titanium and would almost be removed completely without any protection layer as has been tested before. Now the chip is placed in an acetone bath until all resist comes off with the gold layer (see figure 3.2(f)). After spin coating the chip again (see figure 3.2(g)), strip-like areas of PMMA between

the metal contacts are exposed to an electron beam at a very high dose whereby the resist becomes crosslinked as described in the previous section (see figure 3.2(h)). The non-crosslinked PMMA is then removed in an acetone and subsequent isopropyl alcohol bath (see figure 3.2(i)). In the last step the actual subtractive processing of the wire is performed. This is done by argon ion beam etching (see figure 3.2(j)). The duration of it is chosen in such a way that the etching process stops within the SiO_2 layer underneath the TiN film. An SEM image of an exemplary finished sample is shown in figure 3.3.

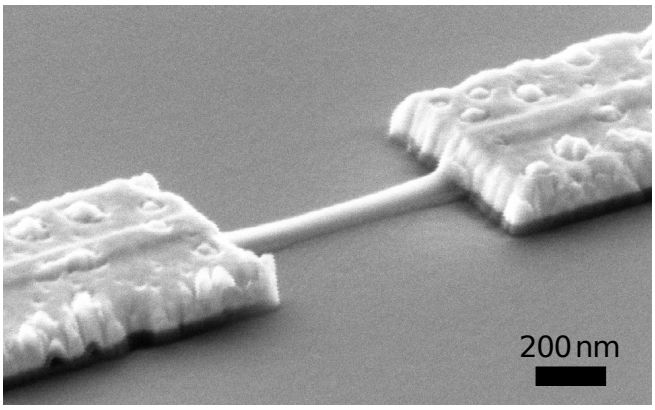

Figure 3.3.: SEM image of an exemplary sample. Between two gold contacts with a thickness of $\sim 120\,\text{nm}$ a wire of TiN was defined by subtractive processing of a plain TiN film. The wire width is $\sim 98\,\text{nm}$ and the wire length is $\sim 780\,\text{nm}$. On top of the wire, the remaining crosslinked PMMA strip overlapping with the gold contacts is visible.

3.1.4. Sample Properties

Same Aspect Ratio Chip "D03-sar"

In the matter of sample fabrication the first objective was to pattern a series of differently sized TiN strips but all with the same aspect ratio of $l/w = 10$ where l is the length and w is the width of the structure with w varying from $1\,\mu\text{m}$ down to about $16\,\text{nm}$. These efforts showed that it is rather hard to achieve a certain desired width of the structures in the range below $100\,\text{nm}$. It was found that the nominal width, i.e., the structure as is was drawn in the EBL software, differs strongly from the width determined using scanning electron microscope (SEM) after the fabrication. Even the patterning of nominally equally sized strips does not result in equal actual sizes but shows a certain variance which is why the problem cannot be solved simply by adjusting the length or the nominal width of the structure. In addition the crosslinked PMMA strips protecting the TiN broadened for narrow structures during the etching process. This is illustrated in the SEM images shown

in figure 3.4. In contrast also a narrowing was seen once in the case of the nominally 100 nm wide structure. The origin of these observations is unclear. Because of these difficulties the fabrication of samples with a reliably fixed aspect ratio was only possible for wires with a width of 100 nm or greater. For narrower wires the deviations from the intended geometry of ten squares are too high and additionally we are not able to determine the width of the actual TiN structure underneath the crosslinked PMMA which changes its appearance during the etching process.

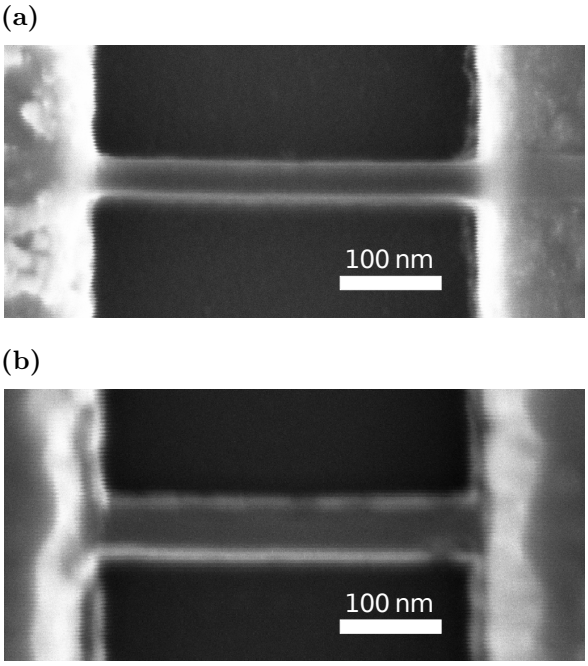

Figure 3.4.: SEM images of the same structure **(a)** before and **(b)** after etching. Before etching, the TiN film is still intact, only the strip of crosslinked PMMA with a width of about 35 nm is visible. After etching it is broadened to about 50 nm. The precise width of the TiN structure underneath can therefore not be determined precisely.

Besides the survey of the structures using SEM, the room temperature resistance R_{300} can also give an indication for the actual width given the sheet resistance $R_\square$ of the film and assuming that the total resistance scales linearly with the number of squares of the structure, meaning that $R_{300} = \text{number of squares} \cdot R_\square = \frac{l}{w} \cdot R_\square$. For large structures in the µm range, this relation is certainly sufficiently true. However, since we deal with an inhomogeneous film we have to expect deviations from this rule for small structures with a width of a few tens of nanometers.
After all we could not achieve the goal of fabricating a sample series with the same aspect ratio as a common feature for all of the structures with sufficient accuracy. The deviations from this demand are too large and the uncertainties are to high in order to be able to compare their behavior in relation to their size. Nevertheless, certain TiN strips of this

chip series yielded interesting measurement results. Whenever presented, we refer to it as D03-sar (short for "same aspect ratio") and state the nominal width of the particular structure.
The sample characteristics are listed in table 3.1. A detailed explanation for the different lines can be found in the caption. Here the widths and number of squares as they were determined using SEM and as they were calculated on the basis of the room temperature resistance can be compared. The differing values resulting from calculations based on different assumptions once again illustrate the difficulties and uncertainties in the estimation of the precise width for narrow wires with $w \lesssim 100\,\mathrm{nm}$. In the estimations based on the room temperature resistance a distinction is made since the chip was measured three times. The second measurement was in contrast to the first one carried out with additional bias resistors. Because of a quite long time period of a few months between these measurements, the TiN structures were subject to oxidation and the room temperature resistance was rising as a consequence. Therefore it was not clear if changes in the measurement results originated from the change of the environment or from a change of the sample properties. To be able to compare the results of the measurements with and without additional bias resistors, the sample was measured a third time shortly after the second measurement. This time again without the resistors. There was no change of the room temperature resistance between the second and the third measurement. Therefore for the first measurement we refer to the chip as D03-sar1 (lines g)-i) in table 3.1) and for the two later measurements as D03-sar2 (lines j)-l) in table 3.1).
A peculiarity is found when we compare the results of the width estimation for the two narrowest wires resulting from the SEM survey (lines c) and e) in table 3.1) with the calculations based on the room temperature resistance (lines i) and l) in table 3.1). From the latter method we obtain larger widths which is in contradiction to the idea that edge effects in the wires caused by the etching process lead to an effectively higher resistance, i.e., an effectively narrower wire, as the width measured using SEM suggests. It was not possible to clarify the origin of this observation.

a) nominal width	16 nm	50 nm	100 nm	500 nm	1000 nm
b) measured length	210 nm	380 nm	788 nm	4800 nm	9850 nm
c) measured width before etching (only crosslinked PMMA strip)	14 nm	36 nm	82 nm	500 nm	986 nm
d) calc. corresp. number of squares	15.0	10.6	9.6	9.6	10.0
e) measured width after etching	28 nm	53 nm	68 nm	500 nm	986 nm
f) calc. corresp. number of squares	7.5	7.2	11.6	9.6	10.0
g) R_{300} of D03-sar1	8 kΩ	10 kΩ	27 kΩ	27 kΩ	27 kΩ
h) calc. corresp. number of squares (assuming $R_\square = 2.7\,\mathrm{k\Omega}$)	3.0	3.7	10.0	10.0	10.0
i) calc. corresp. width	70 nm	103 nm	79 nm	480 nm	985 nm
j) R_{300} of D03-sar2	—	11 kΩ	36 kΩ	39 kΩ	—
k) calc. corresp. number of squares (assuming $R_\square = 3.9\,\mathrm{k\Omega}$)	—	2.8	9.2	10.0	—
l) calc. corresp. width	—	136 nm	86 nm	480 nm	—

Table 3.1.: Characteristics of chip D03-sar. Line a) displays the nominal width of the strip, i.e., the width of the structure as it was drawn in the EBL software. We use this nominal width also later in this work for referring to the different samples. Line b) displays the length as it was determined by means of the SEM. Line c) specifies the width of the baked PMMA strip that was estimated using SEM before the etching process. In line d) we calculate the number of squares based on this width, i.e., we divide line b) by line c). Line e) displays the width of the structure as it was estimated by means of the SEM after the etching process. It shows deviations from the width of the baked PMMA strip as it was measured before the etching process. Line f) specifies the number of squares corresponding to the width after the etching process, i.e., we divide line b) by line e). Line g) shows the resistance values of the samples measured at room temperature before the first measurement run. From the widest sample we assume the sheet resistance to be $R_\square = 2.7\,\mathrm{k\Omega}$ and estimate the number of squares corresponding to the room temperature resistance in line h), i.e., we divide line g) by $R_\square = 2.7\,\mathrm{k\Omega}$. Based on this number we calculate the corresponding width in line i), i.e., we divide line b) by line h). In lines j)-l) we do the same procedure as in the three previous lines but based on the room temperature resistance values that were measured before the two later measurements after the sample was exposed to air for quite a long time whereby the sheet resistance increased due to oxidation. The narrowest and widest structure have not been subject of these measurements. We therefore estimate the sheet resistance for the calculations from the nominally 500 nm wide sample as $R_\square = 3.9\,\mathrm{k\Omega}$. The varying results obtained through the different kinds of estimations for the narrow wires illustrate the difficulties and uncertainties in the precise evaluation of their widths.

Width Dependent Chip "D03-wd"

Since it turned out that the length of the structure, i.e., the distance between the gold contacts, can be defined reliably and without significant variance, a width dependent sample series was fabricated subsequently as a second attempt with a fixed length of 780 nm and nominal widths varying from 800 nm down to 50 nm. We refer to this chip as D03-wd (short for "width dependent") and state the nominal width of the particular structure. While it is again not possible to define or determine the actual width of the TiN strip precisely because of the issues explained above, we fix the length of the structures as a common feature for all of the structures this time.

a) nominal width	50 nm	80 nm	100 nm	200 nm	500 nm	800 nm
b) measured length	780 nm	780 nm	780 nm	780 nm	780 nm	780 nm
c) measured width	36 nm	61 nm	83 nm	173 nm	473 nm	780 nm
d) calc. corresp. number of squares	21.7	12.8	9.4	4.5	1.6	1
e) R_{300}	44 kΩ	29.3 kΩ	25.4 kΩ	13.5 kΩ	7.2 kΩ	4.3 kΩ
f) calc. corresp. number of squares (assuming $R_\square = 4.3\,\mathrm{k\Omega}$)	10.2	6.8	5.9	3.1	1.7	1
g) calc. corresp. width	76 nm	115 nm	132 nm	252 nm	459 nm	780 nm

Table 3.2.: Characteristics of chip D03-wd. The measured widths and lengths in line b) and line c) respectively have been determined using SEM. All structures on this chip feature a length of $l = 780\,\mathrm{nm}$. The calculated number of squares in line d) results from these measurements, i.e., we divide line b) by line c). Line e) shows the room temperature resistance of the structures. From the widest almost square-like sample we assume the sheet resistance to be $R_\square = 4.3\,\mathrm{k\Omega}$ and use this value for the calculation of the number of squares in line f), i.e., we divide line e) by $4.3\,\mathrm{k\Omega}$. Line g) displays the corresponding width where line b) is divided by line f).

We can again estimate the width of the structures either by measuring it by means of SEM (see lines c) and d) in table 3.2) or by calculating it on the basis of the room temperature resistances (see lines e)-g) in table 3.2). The phenomenon of a broadening or narrowing of the crosslinked PMMA strips was not observed this time. However, we again observe the phenomenon for the four narrowest wires that the calculations based on the room temperature resistances of the structures yield larger widths compared to the survey in the SEM which is in contradiction to the idea that edge effects caused by the etching process lead to the observed deviations.

3.2. Measurement Setup

This section depicts the cryogenic environment, the experimental techniques and the measurement equipment used for the electronic characterization of the fabricated TiN micro and nanostructures.

3.2.1. Cryogenics

In order to generate temperatures below $T = 0.3\,\mathrm{K}$ a ^{3}He-^{4}He dilution refrigerator is deployed. A brief insight into the cooling mechanism of a dilution refrigerator is given in the following. For more details we refer to the technical literature of Enss and Hunklinger [17] and Pobell [89].
The cooling principle of a dilution refrigerator is based on the specific properties of ^{3}He/^{4}He mixtures. When the ratio of ^{3}He is higher than 6.6 % the mixture undergoes a spontaneous phase transition when cooled below $T = 0.87\,\mathrm{K}$. This results in a ^{3}He-poor phase (the dilute phase) and a ^{3}He-rich phase (the concentrated phase), the latter floating on top because of its lower density. At temperatures close to zero the concentrated phase consists of pure ^{3}He. However in the diluted phase the concentration of ^{3}He does not drop to zero but reaches a constant value of 6.6 % at saturated vapor pressure - a fact which is very important for dilution refrigeration technology. The ^{3}He atoms in the concentrated phase have a lower entropy than those in the diluted phase. Therefore the transfer of ^{3}He atoms from the concentrated into the diluted phase requires entropy that is provided by the surrounding environment which is cooled down as a consequence. This process is comparable to the evaporation of gases where the necessary latent heat leads to a cooling of the system.
To ensure an uninterrupted cooling, ^{3}He atoms have to be transferred continuously from the ^{3}He-rich into the ^{3}He-poor phase. In a dilution refrigerator this is happening in the so called mixing chamber. Gaseous ^{3}He is pumped into the system from room temperature. Before it enters the mixing chamber, it is therefore passing several heat exchangers for the purpose of pre-cooling and finally condenses at a temperature stage of about $T = 1.5\,\mathrm{K}$. In the cryostats of the working group this is carried out by a Joule-Thomson gas expansion stage, other types of dilution refrigerators use 1 K-pots instead. The gas flows through further heat exchangers before it finally enters the mixing chamber where it is passed into the concentrated phase on top of the mixture. The still is connected to the diluted phase in the mixing chamber by a tube. It is at a temperature of about $T = 0.8\,\mathrm{K}$ where the vapor pressure of ^{3}He is much higher than that of ^{4}He. Because of this, pumping at the still leads very effectively to the almost exclusive evaporation of ^{3}He from the diluted phase.

In order to maintain the concentration of ^{3}He in the diluted phase, atoms of this isotope continuously move from the ^{3}He-rich to the ^{3}He-poor phase. However, the ratio of ^{3}He in the liquid in the still is only at about 1 %. Figure 3.5 shows a photograph of one of the dilution systems that is applied in our working group.

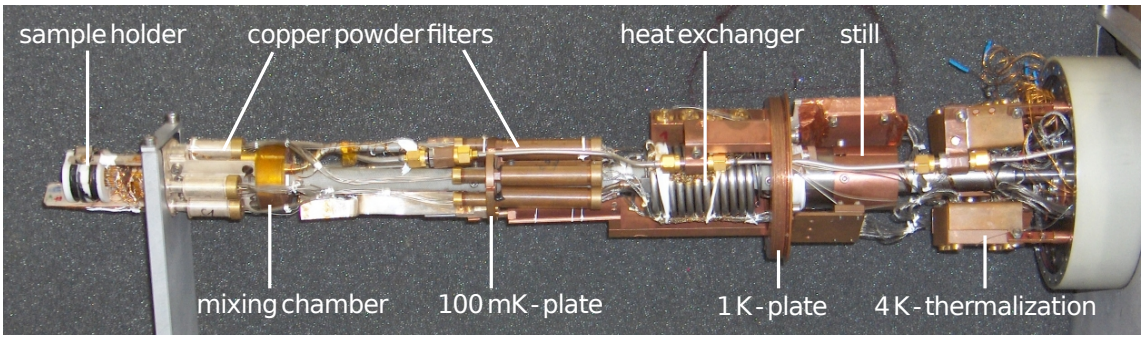

Figure 3.5.: Photograph of the cold part of one of the ^{3}He-^{4}He dilution systems applied in our working group with the vacuum shield removed.

The whole apparatus is surrounded by vacuum and is additionally immersed in a ^{4}He bath inside of a Dewar vessel. The sample to be measured is thermally coupled to the mixing chamber. Typically bath temperatures around $T = 20$–$25\,\mathrm{mK}$ can be reached with the deployed cryostats. A heating resistor installed close to the sample allows for the adjustment of the temperature.

3.2.2. Measurement Instrumentation

All measurement results presented in this thesis were recorded in a standardized two-point dc voltage bias setup, no matter whether the sample is found to be in the insulating or in the superconducting regime. At first glance this might appear unusual. Normally a four-point current bias setup is the method of choice when examining very low resistive or even superconducting samples since this technique eliminates contact and lead resistances from the measurement. However the focus of this work was not in particular the very precise estimation of small resistances. The two-point voltage bias setup offers advantages on the contrary that were indispensable for certain objectives of this work. One of these objectives was to gain insight into the full evolution of the current-voltage characteristics also on the superconducting side in only one single sweep. When the $I(V)$ curve is a non-injective function, jumps would show up when using a current-bias setup and certain parts of it remain hidden. Nonetheless, the lead resistances have to be known and kept in mind for a correct analysis of the measurement results.

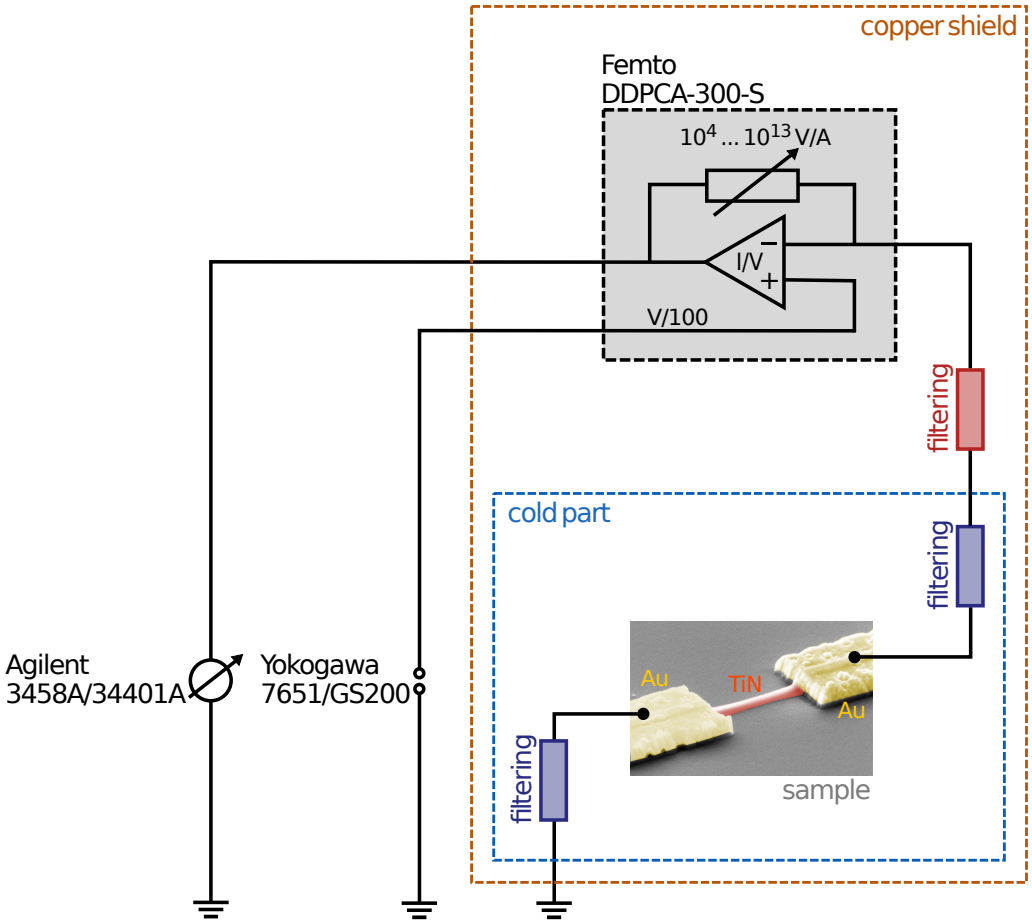

Figure 3.6.: Sketch of the applied two-point dc voltage bias setup. The voltage provided by the *Yokogawa* voltage source is divided by a factor of 100 internally in the *Femto DDPCA-300-S* transimpedance amplifier and is then applied to the non-inverting input of the operational amplifier. Its input is connected directly to the sample and the other side of the sample is terminated with a grounding cap. An *Agilent* multimeter is connected to the output of the amplifier. Filtering at room temperature is provided by π filters, filtering in the cold part is provided by copper powder filters.

A sketch of the applied setup is shown in figure 3.6. A *Yokogawa*, either type *7651* or *GS200*, serves as a dc voltage source. We use a *Femto DDPCA-300-S* transimpedance amplifier, a customized component which internally divides the provided voltage by a factor of 100. This voltage is then applied to the non-inverting input of the operational amplifier. The *Femto DDPCA-300-S* allows for a very compact installation. Because of their small design, several amplifiers can be employed in order to measure several samples in the same measurement run with their inputs directly connected to the terminal box on top of the cryostat. No additional cabling is necessary in between which helps to reduce noise. The other side of the sample simply needs to be terminated with a grounding cap.

The transimpedance of the *Femto* can be adjusted between $10^4\,\mathrm{V/A}$ and $10^{13}\,\mathrm{V/A}$. An *Agilent* multimeter, either type *3458A* or *34401A*, is connected to the output of the *Femto DDPCA-300-S* and is used to detect the resulting voltage.
The measurements were performed in two different dilution cryostats. One of them is placed in a grounded copper box in order to shield it from radiation. Both cryostats feature π filtering of the measurement lines at room temperature (drawn in red in figure 3.6) in order to reduce high frequency noise generated by the equipment and the environment and to lower the effective electron temperature at the sample. Additionally copper powder filters with a cutoff frequency of about 500 MHz are installed in the cold part of the cryostat (drawn in blue in figure 3.6). In both cryostats, the copper powder filters are mounted at the mixing chamber stage. The cryostat which is placed in the copper box additionally provides copper powder filters at the 100 mK stage. Magnetic fields up to $B = 8\,\mathrm{T}$ (in case of the copper box shielded cryostat) or $B = 15\,\mathrm{T}$ (in case of the other employed cryostat) are provided by a superconducting magnet coil.
The wiring at room temperature between the measurement devices and the cryostat line connectors is established by coaxial cables terminated by BNC connectors. GPIB cables are used to connect voltage sources and multimeters to the measurement computer. In order to electrically decouple the computer from the measurement setup, optocouplers are employed.
For some measurements the sample was requested to be embedded between two additional bias resistors of each $50\,\mathrm{k\Omega}$. For that purpose a spacer was designed by our chair technician Michael Weigl as shown in figure 3.7 and subsequently built by the mechanics workshop. SMD (surface-mount device) resistors can be fitted into the provided slits of the spacer. They are thereby inserted between the gold pogo pins pointing into the slits of the spacer from the upper part of the sample holder and the gold contacts on the backside of the chip carrier which is pressed against the spacer from the bottom together with the lower part of the sample holder.

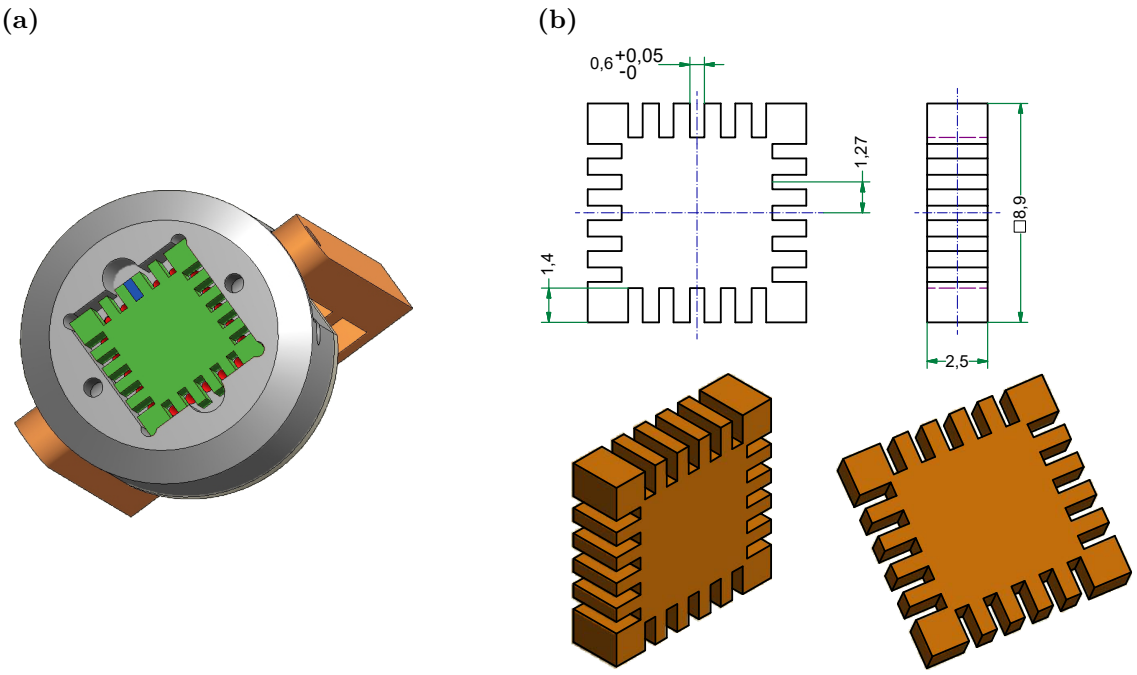

Figure 3.7.: (a) Upper part of the sample holder with inserted spacer (indicated in green). The gold pogo pins (indicated in red) point into the slits. SMD resistors (an exemplary one is indicated in blue) can be fitted into the slits so that they are placed between the pogo pins and the gold contacts on the backside of the chip carrier which is pressed against the spacer from the bottom together with the lower part of the sample holder. **(b)** CAD drawing of the spacer. The dimensions in the sketch are specified in mm.

CHAPTER 4

Experimental Results

4.1. Chip D03-wd – Zero Field Behavior and the Superconducting State

4.1.1. R(T) Dependence

With the two-point voltage bias setup described in chapter 3.2.2, current-voltage characteristics are measured. For a fixed temperature T and a fixed magnetic field B, the resistance of the specific structure can be extracted from the slope of the $I(V)$ curve in the linear range around zero voltage. Figure 4.1 shows this linear resistance of several TiN strips of chip D03-wd (varying width, equal length of 780 nm) versus the temperature T at zero field on a logarithmic scale. The line resistance of the cryostat has been subtracted and for a better comparison, the sheet resistance $R_\square$ is plotted. Here the number of squares was estimated by the room temperature resistance of the particular structures (see line f) in table 3.2). It has to be mentioned that the jump showing up in the data at $T = 2\,\mathrm{K}$ is not an effect arising from the sample but an artifact resulting from a thermalization problem in the measurement setup.
It is seen that all strips are in the superconducting regime. However while R tends towards zero for the widest samples, it clearly saturates for the narrower ones with a finite

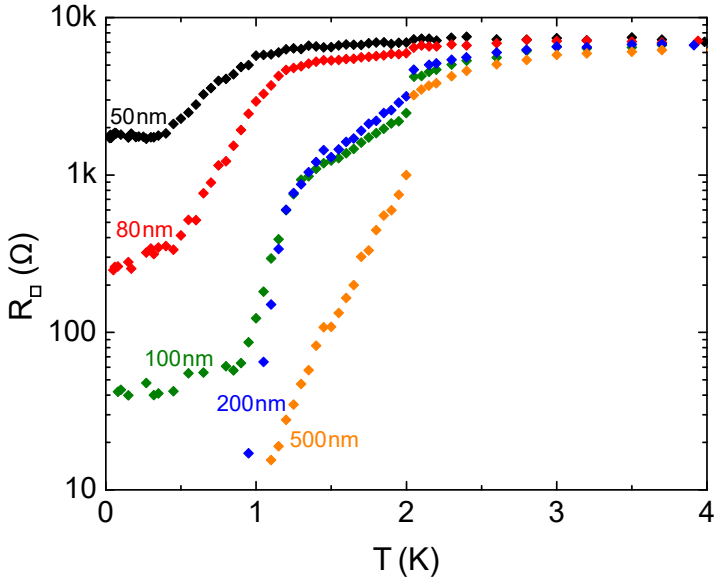

Figure 4.1.: $R_\square(T)$ behavior for TiN strips of chip D03-wd at zero field on a logarithmic scale. The nominal widths are indicated. For the calculation of the sheet resistance $R_\square$ the number of squares was estimated by the room temperature resistance (see line f) in table 3.2). The widest wires tend to zero resistance for $T \to 0$ while the resistance saturates for the narrower samples. The saturation resistance becomes higher with shrinking wire width since phase slip events happen more rapidly. The jump at $T = 2\,\mathrm{K}$ is due to a thermalization problem in the measurement setup.

resistance at $T \to 0$ that increases with decreasing width of the structure. This saturation of the resistance for narrower samples is an indication of the global phase coherence of the superconducting state being suppressed. Our observation is in agreement with earlier measurements on MoGe [90, 91] and Al [92, 93] nanowires. When a proper shielding is provided, the resistive "tail" in the $R(T)$ characteristic of a narrow wire is usually attributed to the presence of quantum phase slips [94, 95]. Thermally activated phase slips are suppressed in this low temperature regime [56]. Each quantum phase slip event by 2π creates a voltage peak where the value of the corresponding integral $\int V dt$ is identical to the magnetic flux quantum ϕ_0. The sum of these voltage peaks results in a finite average voltage. The phase slip rate saturates for $T \to 0$ causing a saturation behavior of the resistance whereby the residual resistance is expected to become higher for shrinking wire width because phase slip events take place more frequently.

For higher temperatures we observe a crossover to a regime where the resistance of the samples is decreasing approximately exponentially with cooling. This broadening of the superconducting phase transition in narrow superconducting wires is usually attributed to the appearance of thermally activated phase slips. In contrast to quantum phase slips, it is thermal activation that allows the system to pass over a free-energy barrier that is proportional to the cross-sectional area of the wire. The corresponding theory was put

forward by J. S. Langer, V. Ambegaokar, D. E. McCumber and B. I. Halperin and is known as LAMH theory [96, 97]. They demonstrated that in the regime of thermally activated phase slips the corresponding temperature dependence of the resistance is given by

$$R(T) = \frac{\pi\hbar^2\Omega}{2e^2k_BT}\, e^{-\Delta F(T)/k_BT} \tag{4.1}$$

where $\Delta F(T)$ is the free energy barrier. In particular it was McCumber and Halperin that complemented the theory by introducing a temperature dependent term Ω that enters the prefactor as

$$\Omega = \frac{L}{\xi}\left(\frac{\Delta F(T)}{k_BT}\right)^{1/2}\frac{1}{\tau_s},\quad \frac{1}{\tau_s} = \frac{8k_B(T_c - T)}{\pi\hbar}. \tag{4.2}$$

L/ξ is the wire length in terms of the coherence length and $1/\tau_s$ the characteristic relaxation rate within the time dependent Ginzburg-Landau theory [98, 99, 100, 101, 102].
It is hardly surprising that our observed temperature dependence shows deviations from the predictions of the LAMH theory that was established for conventional thin superconducting wires. In particular the temperature dependence of the prefactor leads to the observed discrepancies between the theory and our experimental findings. However we obtain satisfying results when we replace the temperature dependent prefactor appearing in equation 4.1 by a constant parameter R_0:

$$R_\square(T) = R_0\, e^{-\Delta F(T)/k_BT}. \tag{4.3}$$

Within the Ginzburg-Landau theory $\Delta F(T)$ is given by

$$\Delta F(T) = \underbrace{\frac{\xi_{GL}wt}{\mu_0}\left(\frac{\hbar}{4e\kappa\xi_{GL}^2}\right)^2}_{k_BT_0}\left(1 - \frac{T}{T_c}\right)^{3/2} \tag{4.4}$$

where ξ_{GL} is the Ginzburg-Landau coherence length ($\xi_{GL} = 8.9\,\mathrm{nm}$, see section 3.1.1), κ the Ginzburg-Landau parameter (see section 2.1.3), w the wire width and t the wire thickness ($t = 3.6\,\mathrm{nm}$, see section 3.1.1).[1] As a fitting function for the $R_\square(T)$ curves, we use

$$R_\square(T) = R_0\, e^{-\frac{T_0}{T}\left(1-\frac{T}{T_c}\right)^{3/2}}. \tag{4.5}$$

[1] The expression for $\Delta F(T)$ can be obtained by a multiplication of the free energy density which is given by $\frac{B_c(T)^2}{2\mu_0} = \frac{1}{\mu_0}\left(\frac{\hbar}{4e\kappa\xi_{GL}^2}\right)^2\left(1 - \frac{T}{T_c}\right)^2$ with the volume $w \cdot t \cdot \xi(T)$, $\xi(T) = \xi_{GL}\left(1 - \frac{T}{T_c}\right)^{-1/2}$, in which the superconducting order parameter is suppressed.

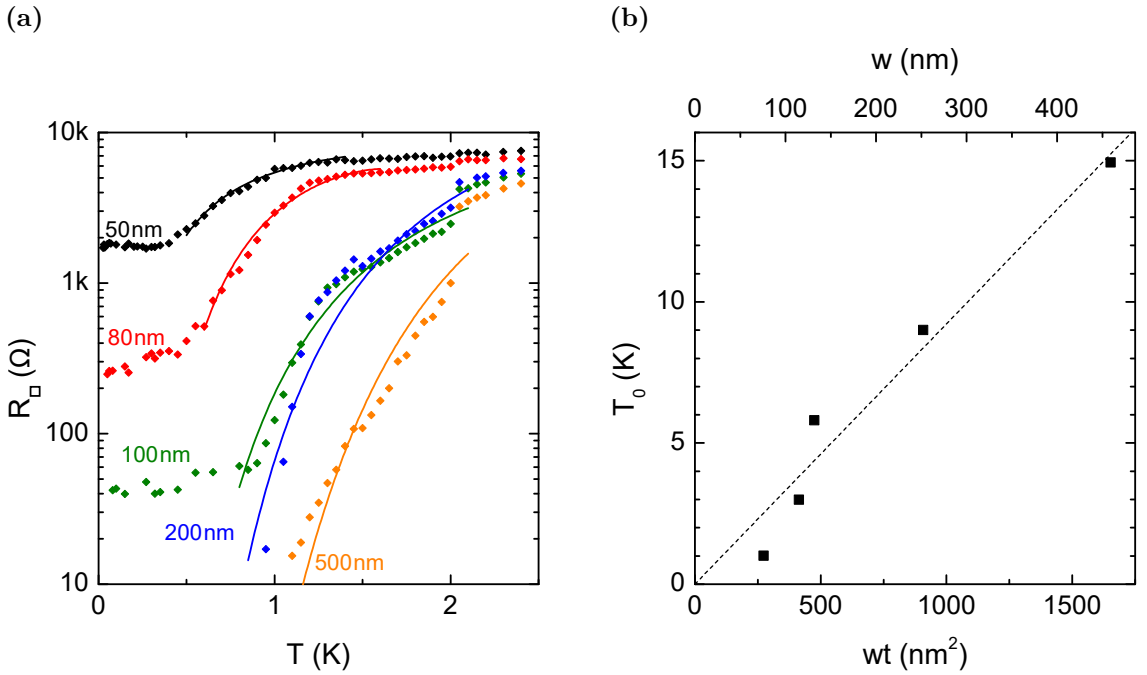

Figure 4.2.: (a) Temperature dependence of the resistance obtained in our experiment (diamonds) compared to the fit curves (lines) based on the LAMH theory but with an adapted constant prefactor. **(b)** Obtained fit parameters T_0 that show an almost proportional dependence on the cross sectional area wt of the wires. The wire width w is additionally assigned on the upper x-axis. The dashed line corresponds to the linear fit of the points. The slope allows for the estimation of the Ginzburg-Landau parameter. We obtain $\kappa = 490 \pm 15$.

From the values of T_0 that the fits yield for the different wire widths, the Ginzburg-Landau parameter κ can be estimated from the slope of the resulting $T_0(wt)$ curve according to

$$T_0 = \underbrace{\frac{\xi_{GL}}{\mu_0}\left(\frac{\hbar}{4e\kappa\xi_{GL}^2}\right)^2\frac{1}{k_B}}_{\text{slope } a} \cdot wt, \tag{4.6}$$

$$\Rightarrow \kappa = \sqrt{\frac{\frac{\xi_{GL}}{\mu_0}\left(\frac{\hbar}{4e\xi_{GL}^2}\right)^2\frac{1}{k_B}}{a}}. \tag{4.7}$$

The resulting fit curves are presented in figure 4.2(a). With $R_0 = (6.72 \pm 1.05)\,\mathrm{k\Omega}$ we find prefactors close to the quantum resistance of Cooper pairs $R_Q = h/4e^2 \approx 6.45\,\mathrm{k\Omega}$.
For the critical temperature the fits yield $T_c = (2.6 \pm 0.8)\,\mathrm{K}$ which deviates by a factor of ~ 2 from the critical temperature $T_c = 1.29\,\mathrm{K}$ specified for the film (see [84] and section 3.1.1). However the $R_\square(T)$ curve corresponding to the nominally 500 nm wide sample suggests that in fact the critical temperature obtained by the adapted LAMH fit is in good agreement

with the experimentally observable value for our chip. A deviation to the value observed in [84] is thinkable, since the film behavior is always affected by external influences like for instance oxidation processes and thermal cycling.
The values obtained for T_0 are plotted as a function of the cross sectional area wt of the wires in figure 4.2(b). On the upper x-axis the wire width w is assigned additionally. The observed progression is in good agreement with the expected proportional dependence on the wire cross section. The dashed line shows the corresponding linear fit of the points. From the slope of the curve the Ginzburg-Landau parameter κ can be estimated (see equation 4.7). This yields $\kappa = 490 \pm 15$. Our values deviate from $\kappa = 191$ that was obtained by Postolova et al. [84] by a factor ~ 2.5.

4.1.2. Temperature Dependence of the Current-Voltage Characteristics and the Critical Current

Figure 4.3 shows the temperature-dependent current-voltage characteristics of the TiN strips of chip D03-wd from wide (figure 4.3(a): 800 nm) to narrow (figure 4.3(f): 50 nm) at zero field corresponding to the resistance values plotted in figure 4.1. As mentioned in chapter 3.2.2 we are able to access the descending parts of the curves since we deploy a voltage bias setup. The characteristics were measured in both directions and no hysteresis was observed. In the legend of each plot, the temperature corresponding to the $I(V)$ curve where we observed the smallest slope at zero voltage, i.e., the highest resistance, is boxed in order to simplify the assignment. For higher temperatures, the slope increases meaning that the resistance drops. The corresponding $I(V)$ curves cross the ones measured for smaller temperatures.
A clear evolution is found with shrinking wire width. The slope around zero voltage of the $I(V)$ curve measured for the three widest wires corresponds to the line resistance of the cryostat meaning the sample is completely in the superconducting state. When we go to narrower wires the saturation regime of the resistance is entered and the slope in the linear range gradually decreases. At the same time the critical current is becoming smaller and the current peak is getting less pronounced until it disappears completely for the narrowest sample. These observations are consistent with a phase slip scenario and a phase slip rate that increases for narrower strips.
The two widest samples display a behavior similar to the one observed in macroscopic TiN films: a sharp current peak at small voltages followed by a distinct current plateau and a jump to the normal state characteristic [103]. In macroscopic TiN films the plateau appears more flat and pronounced. We believe that the emergence of the plateau can be explained by the occurrence of relaxation oscillations as they were also reported in [104].

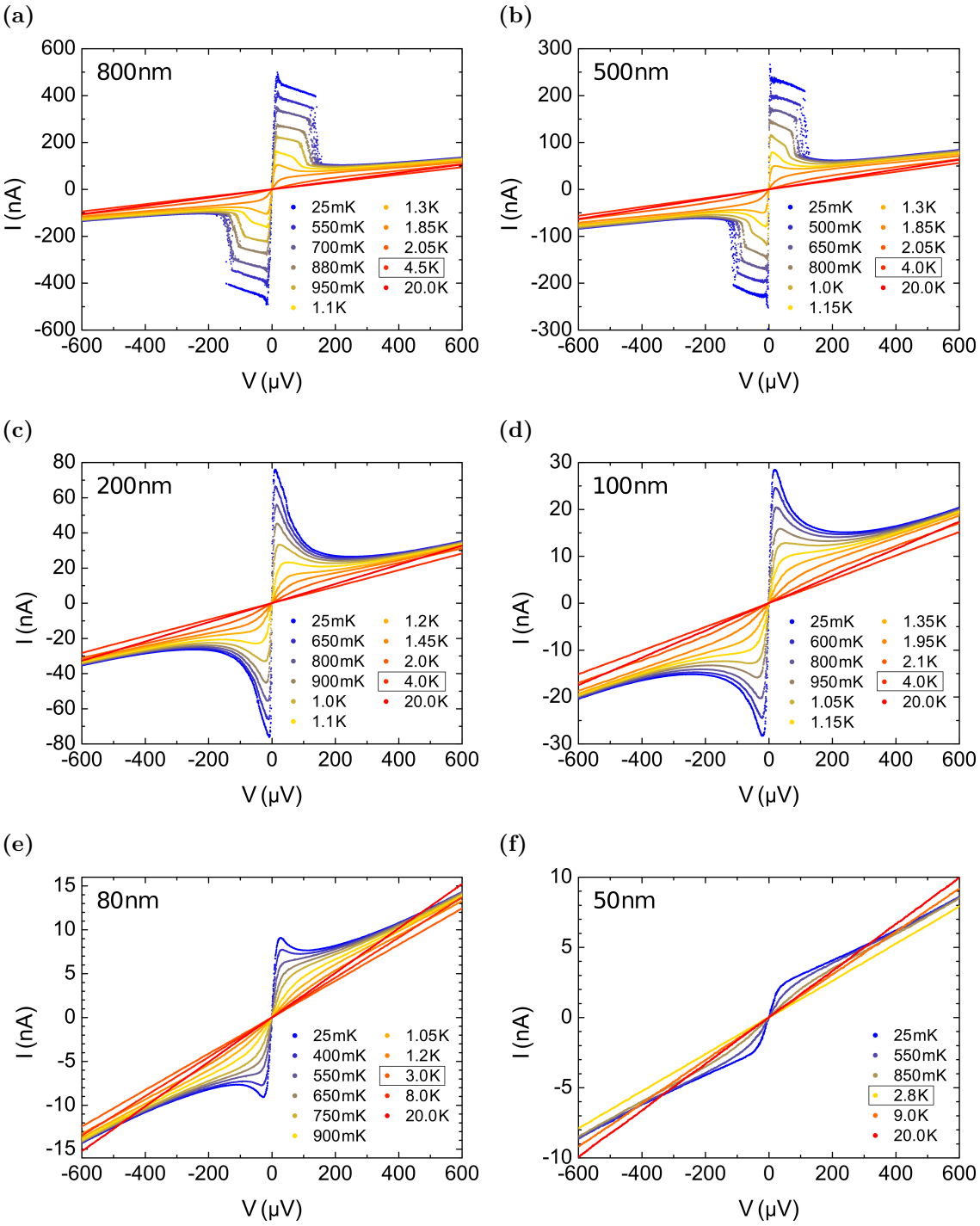

Figure 4.3.: Temperature dependence of the current-voltage characteristics of chip D03-wd for wires with nominal widths of **(a)** 800 nm, **(b)** 500 nm, **(c)** 200 nm, **(d)** 100 nm, **(e)** 80 nm, **(f)** 50 nm at zero magnetic field. The slope at zero voltage and the critical current decrease for shrinking wire width. For a better assignment, in the legend of each plot the temperature corresponding to the $I(V)$ curve where we observed the smallest slope at zero voltage, i.e., highest resistance, is boxed. For higher temperatures, the slope increases monotonically, i.e., the resistance drops, and the $I(V)$ curves cross the ones measured for smaller temperatures.

The phenomenon results from a sharp negative differential resistance which leads to oscillations similar to the effect observed in tunnel diodes. For the narrower samples the plateau feature is lost and the sharp current spike turns into a smooth peak.
Interestingly at small voltages the $I(V)$s of the 50 nm to 200 nm wide wires resemble a behavior very similar to that of ultrasmall Josephson junctions as presented in reference [47] which is explained and modeled in the framework of the Ivanchenko-Zil'berman theory [44] (see section 2.2.3). We will analyze this behavior more closely later in this chapter (see section 4.1.4). At higher voltages the current is gradually taken over by the normal state resistance of the wires.

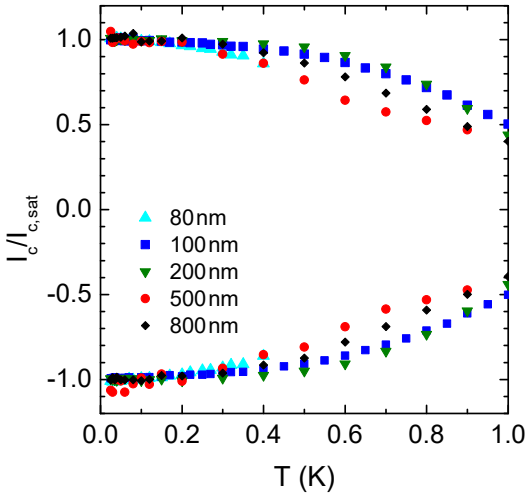

Figure 4.4.: Critical current at zero field normalized to the saturation values that are reached at the lowest accessible temperatures for the different wires plotted as a function of temperature. The nominal widths of the wires are indicated in the legend.

We can extract the critical current observed in the $I(V)$ curves and plot it as a function of temperature (see figure 4.4). For all wires we observe a saturation behavior of the critical current at temperatures below $T = 200\,\mathrm{mK}$. For higher temperatures the critical current gradually decreases whereby we do not see any significant systematic dependence on the wire width. For a better comparison, in figure 4.4 the critical current is normalized to the saturation value that is reached at low temperatures for each of the wires.

4.1.3. Width Dependent Critical Current

The critical current I_c of the wires at $T = 35\,\mathrm{mK}$ is extracted from the maximum of the current-voltage characteristics and is plotted vs. the wire width w in figure 4.5(a). The dashed line indicates a linear progress from the data point obtained for the widest

sample towards zero which would correspond to a proportional relation between wire width and critical current. One would expect this kind of relation for the case of a simple superconducting strip in the absence of any width dependent phenomena like quantum phase slips where the critical current density J_c is constant independently of the wire width. We see a clear deviation from this kind of relation. The critical current decreases more rapidly than one would expect from the wire width.

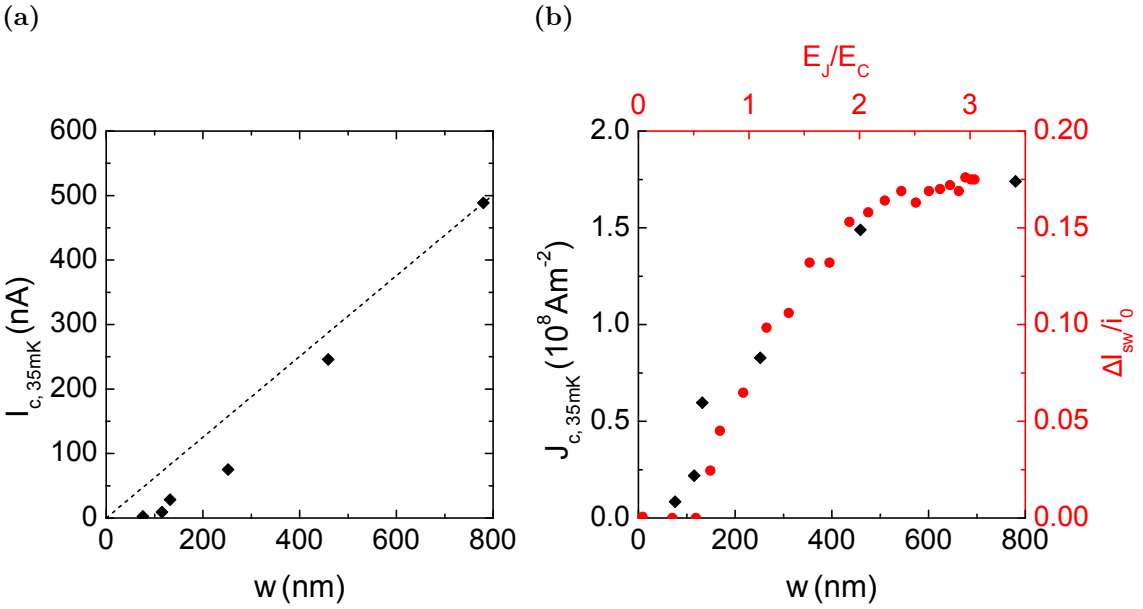

Figure 4.5.: (a) Critical current vs. sample width. The wire width was calculated based on the room temperature resistance of the structures (see line f) in table 3.2). The dashed line indicates a linear progress from the widest wire towards zero, i.e., a constant critical current density. Our observation shows a clear deviation from this correlation. **(b)** shows the corresponding critical current densities (black diamonds and black axes) for a better illustration of the strong deviation from a constant critical current density as it is expected for a simple superconducting strip. Our data is compared to the data from [105] (red dots and red axes) where the variation of the switching current ΔI_{SW} in a chain of six Josephson junctions in units of the critical current of a single SQUID i_0 is plotted vs. the ratio E_J/E_C. The axes are scaled freely.

For a better illustration the critical current density $J_c = I_c/(wt)$ at $T = 35\,\mathrm{mK}$ with $t = 3.6\,\mathrm{nm}$ being the wire thickness is plotted in figure 4.5(b) (black diamonds and black axes). It dramatically decreases with shrinking wire width indicating that the supercurrent is strongly impeded by phase fluctuations.

For the data plotted in figure 4.5 the wire width is again estimated from the room temperature resistance of the samples (see line f) in table 3.2). It has to be mentioned that the observed deviation from a constant critical current density is also observed when the wire width is estimated in a different way, like for example by a geometric characterization

using SEM. This was checked in order to exclude the possibility that the observed behavior only results from a general mistake in the estimation of the wire width.
We can compare the width dependent behavior of the critical current density in our wires to the data from [105] where quantitative measurements on a chain of six Josephson junctions are presented. The junctions are realized by SQUIDs (superconducting quantum interference devices) which allows for the tuning of the E_J/E_C ratio by varying the magnetic flux through the SQUIDs and thereby changing the strength of quantum phase fluctuations. The amplitude of the corresponding switching current ΔI_{SW} in units of the critical current of a single SQUID i_0 was determined. The wire width of our samples should correlate linearly with a variation of E_J. The data from [105] is added to our data plot in figure 4.5(b) (red axes and red dots) and a good agreement can be observed. This is a strong indication that the suppression of the critical current in our wires is controlled by the occurrence of quantum phase slips.

4.1.4. Ivanchenko-Zil'berman Modeling

The current-voltage characteristics of the four narrowest wires of chip D03-wd (see figure 4.3(c)-4.3(f)) resemble the behavior of small Josephson junctions [47] which can be modeled with the Ivanchenko-Zil'berman theory [44] presented in section 2.2.3. Before the actual fitting routine can be done, the ohmic part of the $I(V)$ curve, i.e., the normal state current I_N through the normal state resistance R_N, must be subtracted. R_N behaves as a parallel resistance and the current axis has to be recalculated as

$$I = I_\mathrm{det} - I_N = I_\mathrm{det} - \frac{V}{R_N} \tag{4.8}$$

where I_det denotes the total current detected in the experiment as it was plotted in figure 4.3. For the sake of an easier notation, other than in the previous presentations of the measurement data, I will always denote the measured current after the subtraction of the normal state current I_N within this section.
Figure 4.6 exemplarily shows this procedure for the current-voltage characteristic obtained for the 200 nm wide wire at a temperature of $T = 100\,\mathrm{mK}$. The black curve shows the measured original characteristic, i.e., $I_\mathrm{det}(V)$. The gray dashed line corresponds to the normal state current I_N which is subtracted from the original $I_\mathrm{det}(V)$ in order to obtain the green $I(V)$ curve. This curve is then subject to the actual Ivanchenko-Zil'berman fitting routine that yields the red curve and which we will address later on.
The normal state resistance R_N is not treated as a fixed value but as a free parameter in the fitting procedure. In figure 4.7(a) we compare the values obtained for R_N to the $R(T)$

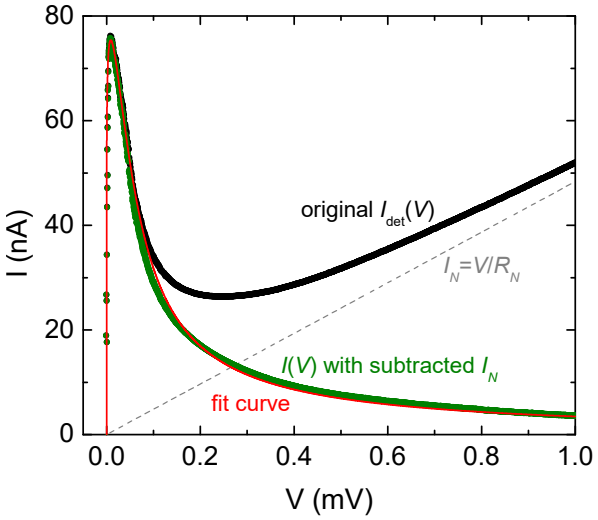

Figure 4.6.: Demonstration of the subtraction of the normal state current I_N for the 200 nm wide wire of chip D03-wd at a temperature of $T = 100$ mK. The black curve is the original current-voltage characteristic as it was recorded in the measurement. The gray dashed line represents the ohmic part of this curve corresponding to the current I_N through the normal state resistance R_N of the sample. A subtraction of this current contribution from the original characteristic yields the green curve. The red line depicts the fit curve obtained by Ivanchenko-Zil'berman modeling.

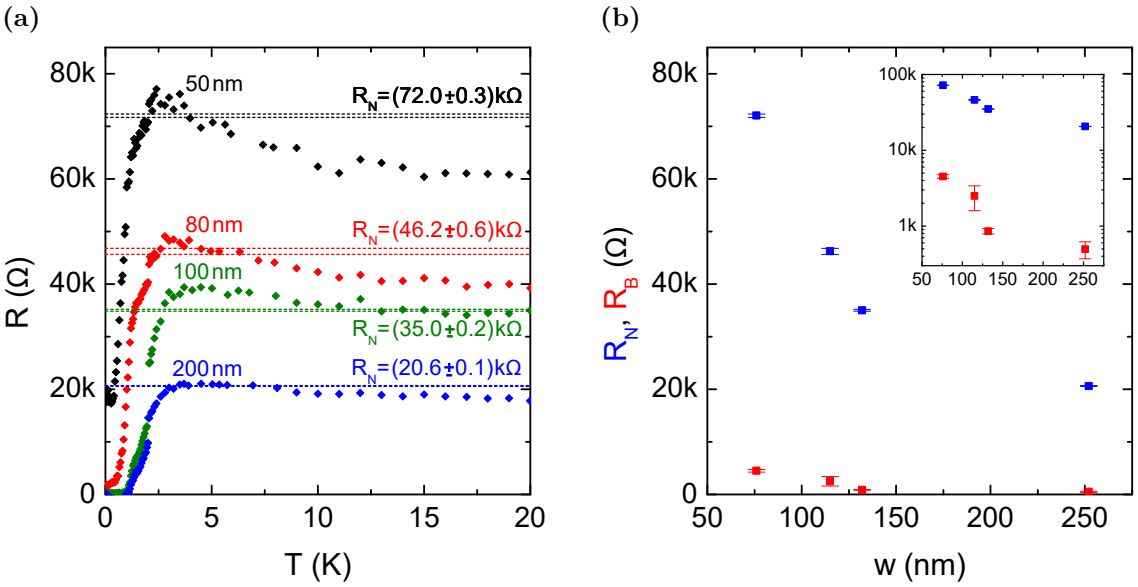

Figure 4.7.: **(a)** $R(T)$ behavior of the four narrowest wires of chip D03-wd compared to the mean value of the parameter R_N plus/minus standard deviation (range indicated by dashed lines) resulting from the fitting process. We see that the values of R_N correspond to the temperature range of 2–3 K where the current-voltage characteristics begin to display a linear behavior. **(b)** Normal state resistance R_N (blue squares) compared to the values obtained for the parameter R_B (red squares) as a function of the wire width as it was estimated by the room temperature resistance of the samples. The error bars indicate the standard deviation of the obtained values in the fitted temperature range. The inset shows the same data on a logarithmic resistance scale for a better illustration.

behavior of the different samples. The dashed lines indicate the ranges where the normal state resistance values are found. It is seen that they roughly correspond to the resistance value which is found between $T = 2\,\mathrm{K}$ and $T = 3\,\mathrm{K}$ for each of the wires, which is where the nonlinearities in the current-voltage characteristics disappear and the curves start to exhibit a linear behavior.

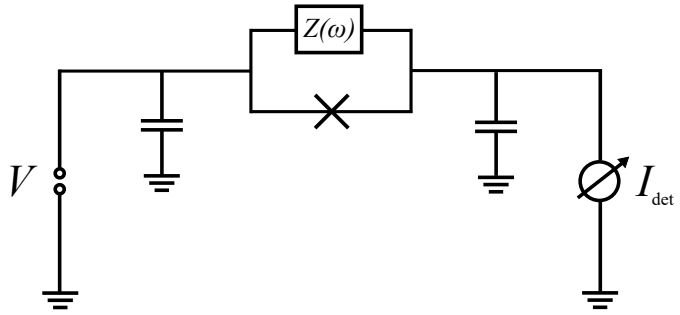

Figure 4.8.: Equivalent circuit for our experiment. The resistance of the environment is sketched as a frequency dependent impedance $Z(\omega)$ in parallel to the junction.

The sequence of the fitting procedure and how it is implemented in *Mathematica* and *Origin* is described in detail in appendix B. In the following we want to explain in particular the adaptations we need for the Ivanchenko-Zil'berman model in order to properly describe our system. Within the Ivanchenko-Zil'berman theory and the work of Steinbach et al. [44, 47], R_B is a fixed external series resistance, e.g., the internal resistance of the voltage source. For the curve that is produced by equation 2.36, R_B causes a broadening of the current peak and at the same time a decrease of the zero voltage slope. However within the Ivanchenko-Zil'berman theory an ideal ohmic environment is assumed where R_B is a fixed series resistance which is constant over the whole frequency range ($R_B(\omega) = const.$). Such an environment was experimentally realized by Steinbach et al. for the first time. This is certainly not the case in our experiment where we have to assume that the impedance provided by the environment is frequency dependent. This frequency dependent environment is illustrated as an impedance $Z(\omega)$ in parallel to the junction in the equivalent circuit sketched in figure 4.8. In the case of $\omega = 0$, the real part of this impedance is identical to our normal state resistance R_N which is a parallel dc resistance:

$$\mathrm{Re}(Z(\omega = 0)) = R_N. \tag{4.9}$$

On the other hand, the broadening of the current-voltage characteristic is caused by the dissipation near the plasma frequency ω_p of the junction. For $\omega = \omega_p$ the real part of Z is identical to R_B which is a parallel ac resistance:

$$\mathrm{Re}(Z(\omega = \omega_p)) = R_B. \tag{4.10}$$

In the case of $\omega = 0$, there is no series resistance. This means that in order to correctly model the behavior of our experiment we have to subtract the voltage drop across a series resistance R_B from the $I(V_{B_{IZ}})$ curve resulting from the Ivanchenko-Zil'berman relation in equation 2.36.

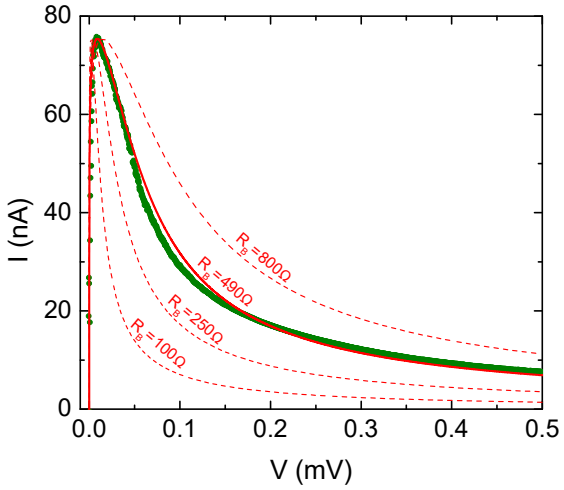

Figure 4.9.: Current-voltage characteristic measured for the 200 nm wide wire at a temperature $T = 200\,\mathrm{mK}$ (green) compared to various fit curves resulting from the adapted Ivanchenko-Zil'berman relation for several values ob R_B which influence the broadening of the current peak (red). The solid red curve for $R_B = 490\,\Omega$ matches the progression of the experimental data.

In figure 4.9 we compare the measurement curve obtained for the 200 nm wide wire at a temperature of $T = 100\,\mathrm{mK}$ (green) to the fit curves resulting from the Ivanchenko-Zil'berman relation with the described adaptation for various values of R_B (red) which influence the broadening of the current peak. The solid red curve corresponding to $R_B = 490\,\Omega$ exhibits the correct zero voltage slope and the correct broadening. The width dependence of the obtained values for the parameter R_B is plotted in figure 4.7(b) (red squares). We oppose them to the values obtained for the normal state resistance R_N (blue squares). The inset shows the same data but on a logarithmic scale for a better illustration. For all wires, the dc resistance R_N exceeds R_B by one to two orders of magnitude.
In our fitting routine we further adapt the Ivanchenko-Zil'berman formula from equation 2.36 by introducing an effective temperature T_{eff} that replaces the set bath, i.e., sample temperature T. The intrinsic critical current I_0 has to be a constant value in the low temperature limit but may decrease for higher temperatures. Together with the adaptations that we explained earlier, the Ivanchenko-Zil'berman relation then transforms to

$$I(V_{B_{IZ}}) = I_0 \,\mathrm{Im}\left[\frac{\mathfrak{I}_{1-i\beta\hbar V_{B_{IZ}}/2eR_B}(\beta E_J)}{\mathfrak{I}_{-i\beta\hbar V_{B_{IZ}}/2eR_B}(\beta E_J)}\right],\ \beta = \frac{1}{k_B T_{\mathrm{eff}}},\ V = V_{B_{IZ}} - R_B I. \qquad (4.11)$$

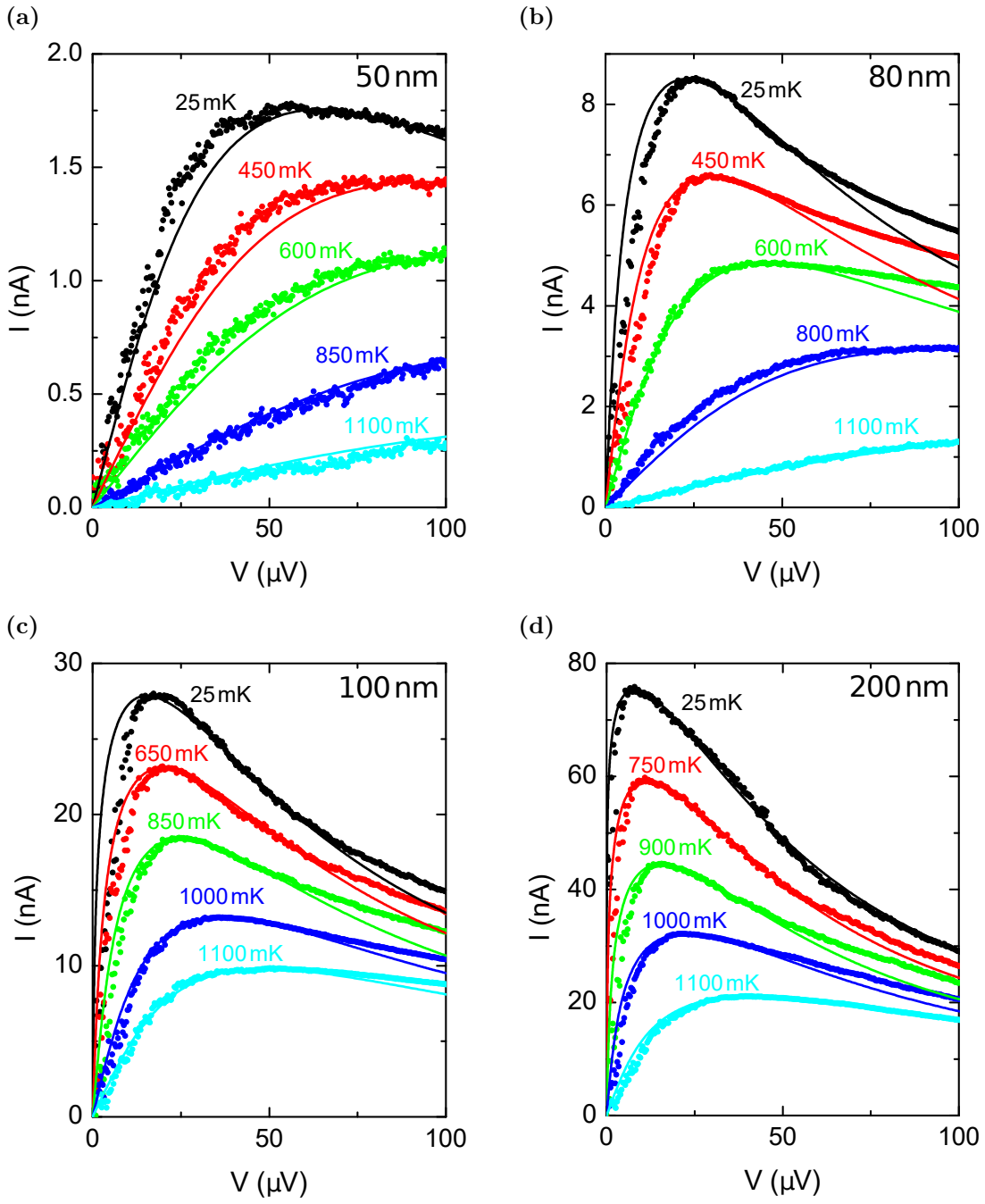

Figure 4.10.: Ivanchenko-Zil'berman fits for wires of chip D03-wd with nominal widths of **(a)** 50 nm, **(b)** 80 nm, **(c)** 100 nm and **(d)** 200 nm for various temperatures between $T = 25$ mK and 1.1 K. The dotted graphs are the measurement curves after the subtraction of the normal state resistance. The solid lines are the fit curves.

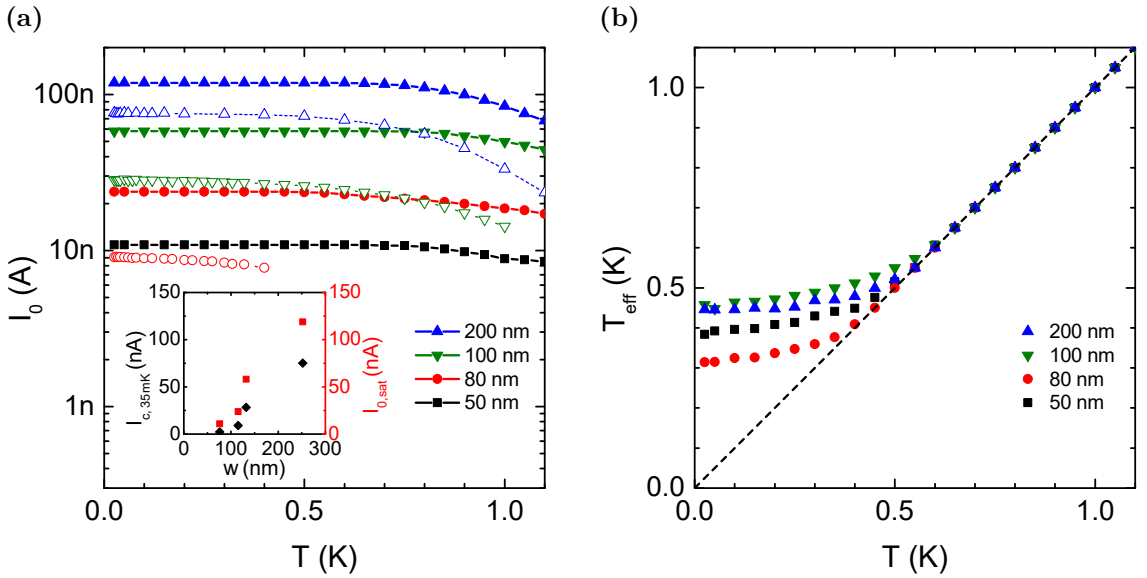

Figure 4.11.: Fitting parameters obtained by Ivanchenko-Zil'berman modeling: **(a)** Intrinsic critical current I_0 as a function of temperature. I_0 is constant up to a temperature of $T \sim 600\,\mathrm{mK}$ and decreases for higher temperatures. For comparison the open symbols show the measured values of the critical current I_c. The intrinsic values of I_0 obtained through the fitting routine are about 1.6 to 2.6 times larger than the values observed for I_c in the experiment. The inset additionally shows a comparison of the obtained saturation value of I_0 (red squares) with the measured critical current at $T = 35\,\mathrm{mK}$ (black diamonds) as it was already shown in figure 4.5(b). Both values scale in the same way with the wire width. **(b)** Effective temperature T_{eff} vs. bath temperature T. A saturation is found around $T_{\mathrm{eff}} \sim 400\,\mathrm{mK}$ without any clear observable dependence on the wire width.

The fitting procedure can be carried out well up to a temperature of $T \sim 1.1\,\mathrm{K}$. For higher temperatures the measurement curves after the subtraction of the normal state current I_N show a progression which is too flat for a reasonable adjustment of the fit curve. The Ivanchenko-Zil'berman fits for the four samples for various temperatures between $T = 25\,\mathrm{mK}$ and $T = 1.1\,\mathrm{K}$ are shown in figure 4.10. The parameters I_0 and T_{eff} resulting from these fits are presented in figure 4.11. The fits yield an I_0 (see filled symbols in figure 4.11(a)) which is constant up to a temperature of $T \sim 600\,\mathrm{mK}$ and decreases for higher temperatures which is consistent with a decrease of the energy gap Δ above $T_c/2$ as we extract it from the measurements on the 500 nm wide sample. We added the measured values of the critical current I_c as open symbols. The intrinsic values of I_0 obtained through the fitting routine are about 1.6 to 2.6 times larger than the values observed for I_c in the experiment. The inset shows a comparison of the obtained saturation value of I_0 (red squares) with the measured critical current at $T = 35\,\mathrm{mK}$ (black diamonds) as it was already presented in figure 4.5(b). Both values scale in the same way with the wire width.

We further observe that the effective temperature T_{eff} saturates at temperatures around $T = 400\,\text{mK}$ (see figure 4.11(b)) with deviations depending on the wire width but without any systematic dependence on it. This value is far too high to be explained with extrinsic impacts like insufficient filtering, i.e., an offset between the bath temperature and the electron temperature. We believe that it is very likely another manifestation of quantum phase slips which are not contained in the simple Ivanchenko-Zil'berman model.

4.2. Chip D03-wd – Magnetic Field Behavior and the Insulating State

4.2.1. Magnetic Field Dependence of the Current-Voltage Characteristics and the Critical Current

In the last section it was demonstrated that in zero magnetic field, the TiN strips experience a crossover from the typical behavior of a two-dimensional film to that of a small Josephson junction when their width is continuously decreased. In the following we want to study the properties of the strips in an out-of-plane magnetic field.
Figure 4.12 gives an overview of the magnetic field evolution of the current-voltage characteristics obtained for the TiN strips of chip D03-wd from wide (figure 4.12(a): 800 nm) to narrow (figure 4.12(f): 50 nm) at a temperature of $T = 35\,\text{mK}$. In the legend of each plot, the magnetic field corresponding to the $I(V)$ curve where we observed the smallest slope at zero voltage, i.e., the highest resistance, is boxed in order to simplify the assignment of the curves. For higher magnetic fields, the slope increases again slightly, meaning that there is a weak decrease in resistance. However, except for the smallest wire the curves corresponding to the two highest plotted magnetic fields are barely distinguishable on the chosen scales.
By comparison to figure 4.3 we notice on first sight that increasing the magnetic field has a similar influence on the evolution of the curves as increasing the temperature: generally the critical current is suppressed and the slope at zero voltage decreases. However, when we have a closer look by plotting the critical current as a function of the magnetic field (see figure 4.13(a)), we see that in fact the 80 nm and 100 nm wide wires display a slight increase of the critical current up to $B \sim 200\,\text{mT}$ before it starts to decrease. For a better comparison we plot the critical current normalized to the critical current at zero field here. For the two widest wires, the critical current is highly sensitive to the magnetic field. Already at a field of $B = 20\,\text{mT}$ it is reduced by a factor of ~ 2. This behavior manifests as a sharp peak in figure 4.13(a). The narrower samples do not show this strong

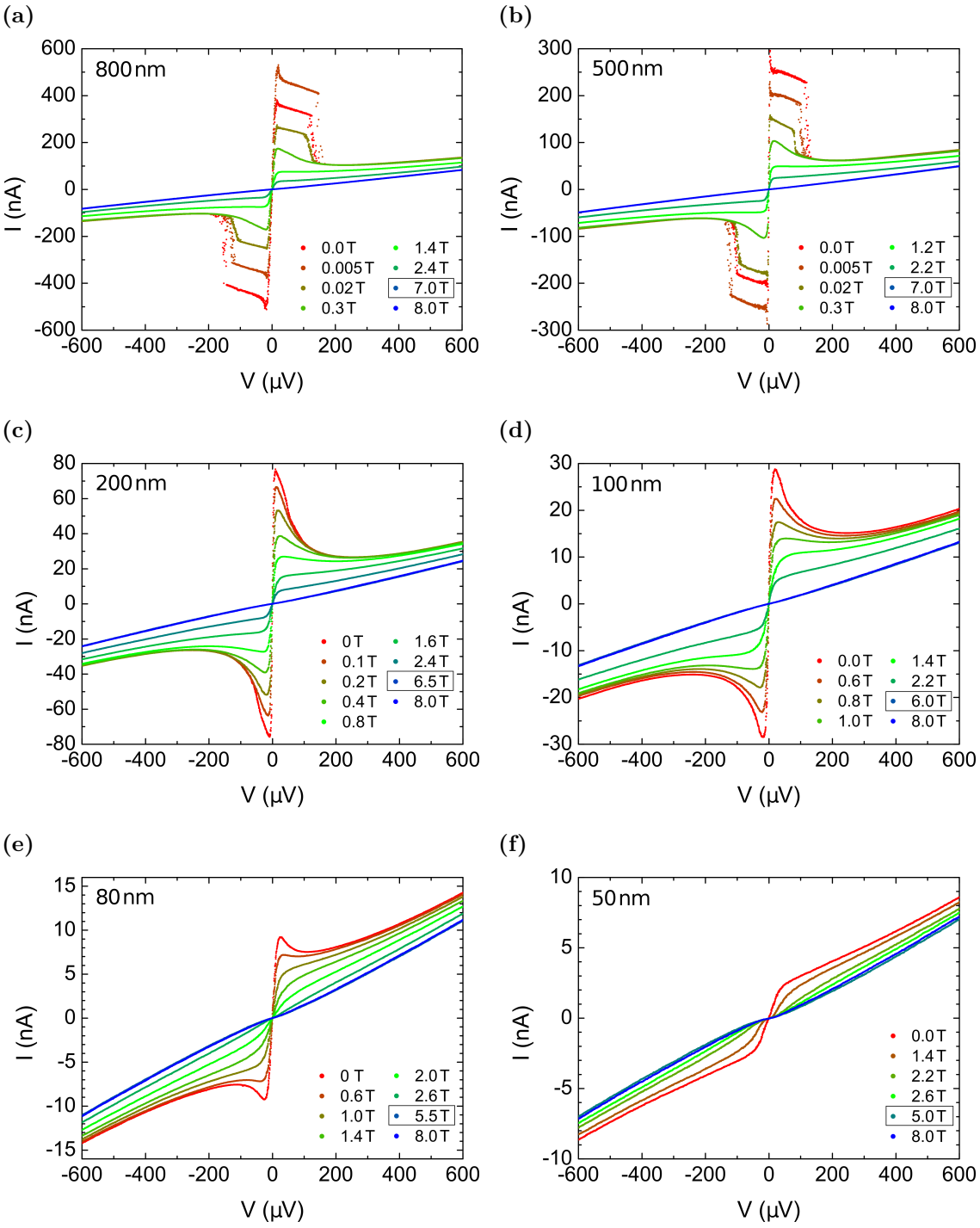

Figure 4.12.: Magnetic field dependence of the current-voltage characteristics of chip D03-wd for wires with nominal widths of **(a)** 800 nm, **(b)** 500 nm, **(c)** 200 nm, **(d)** 100 nm, **(e)** 80 nm, **(f)** 50 nm at a temperature of $T = 35$ mK. For a better assignment, in the legend of each plot the magnetic field corresponding to the $I(V)$ curve where we observed the smallest slope at zero voltage, i.e., highest resistance, is boxed. However, except for the smallest wire the curves corresponding to the two highest plotted magnetic fields are barely distinguishable on the chosen scales.

sensitivity to small magnetic fields and we dot see the peak feature in the $I_c(B)$ dependence. Figure 4.13(b) shows a zoom into the small field range for the two widest wires where the precise shape and position of the peaks becomes visible. Clearly they are shifted from zero to small finite fields ($\sim 3\,\mathrm{mT}$ for the 500 nm wide wire and $\sim 1\,\mathrm{mT}$ for the 800 nm wide wire) and the shift happens towards opposite directions for the two different wires. Also for each wire the positive critical current values (extracted at positive bias voltages) are shifted in the opposite direction in comparison to the negative ones (extracted for negative bias voltages). The shift is therefore not due to a remanent field in the magnet. Also we checked and excluded that the shift directions are inverted when the sweep direction of the bias voltage is reversed. The effect therefore is also not a hysteresis arising from the sweep direction but produced by the sample itself.

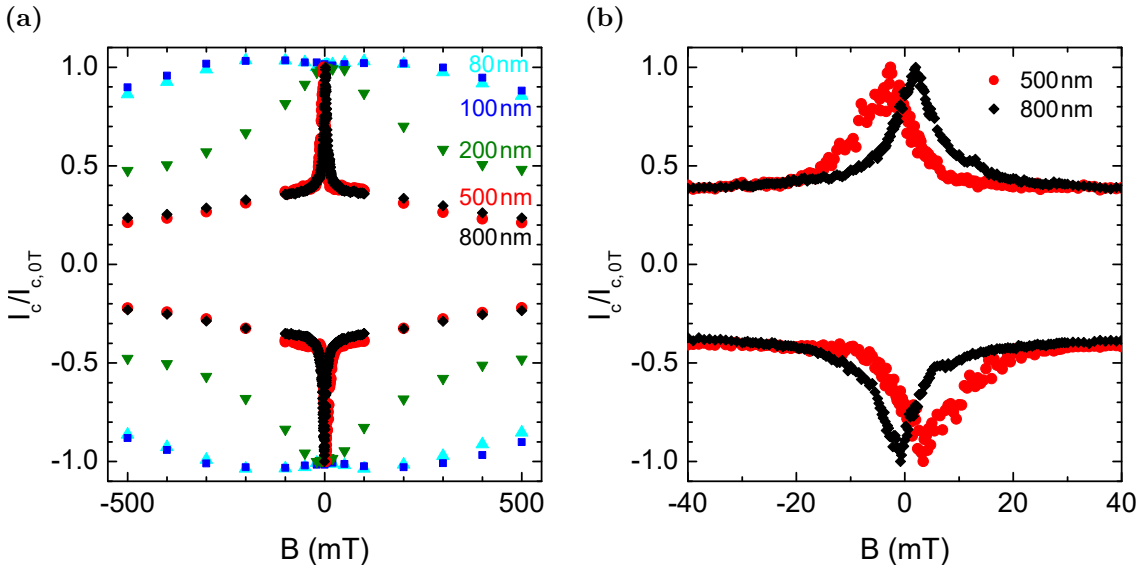

Figure 4.13.: **(a)** Normalized critical current at $T = 35\,\mathrm{mK}$ as a function of the magnetic field for wires with nominal widths of 80 nm, 100 nm, 200 nm, 500 nm, and 800 nm. **(b)** Zoom into a small field range for the two widest wires where the precise shape and position of the peaks becomes visible.

On closer inspection of the current-voltage characteristics of the narrowest wire (see figure 4.12(f)) we observe a behavior that was not present in zero field. We see that in a certain field range a blockade-like area with reduced current develops within the superconducting branch around zero voltage. On the chosen scale in figure 4.12(f) this is already clearly visible. This observations will be inspected more closely in the upcoming sections.

4.2.2. Wide Samples in the Magnetic Field

We will start with a brief survey of the behavior of the wide wires in the magnetic field. Figure 4.14 shows the $R(T)$ characteristics of the 100 nm, 200 nm and 500 nm wide wires of chip D03-wd on a logarithmic scale for magnetic fields ranging between $B = 0\,\mathrm{T}$ and $B = 8\,\mathrm{T}$. The 500 nm wide sample (see figure 4.14(a)) displays the typical behavior of a TiN film on the superconducting side: the resistance tends to zero for zero magnetic field as already presented before and the critical temperature is gradually suppressed for increasing magnetic field. Down to the lowest achievable temperatures of $T \sim 25\,\mathrm{mK}$ we find a drop in the resistance up to a magnetic field of $B = 3\,\mathrm{T}$ without any saturation behavior. For higher magnetic fields a slight increase of the resistance is observed. This high field behavior is visible for all samples. For the 200 nm wide wire we still find a drop to zero resistance for very small magnetic fields. For $B > 0.2\,\mathrm{T}$ a saturation of the resistance arises. For the 100 nm wide wire this saturation behavior is already observed for zero field.

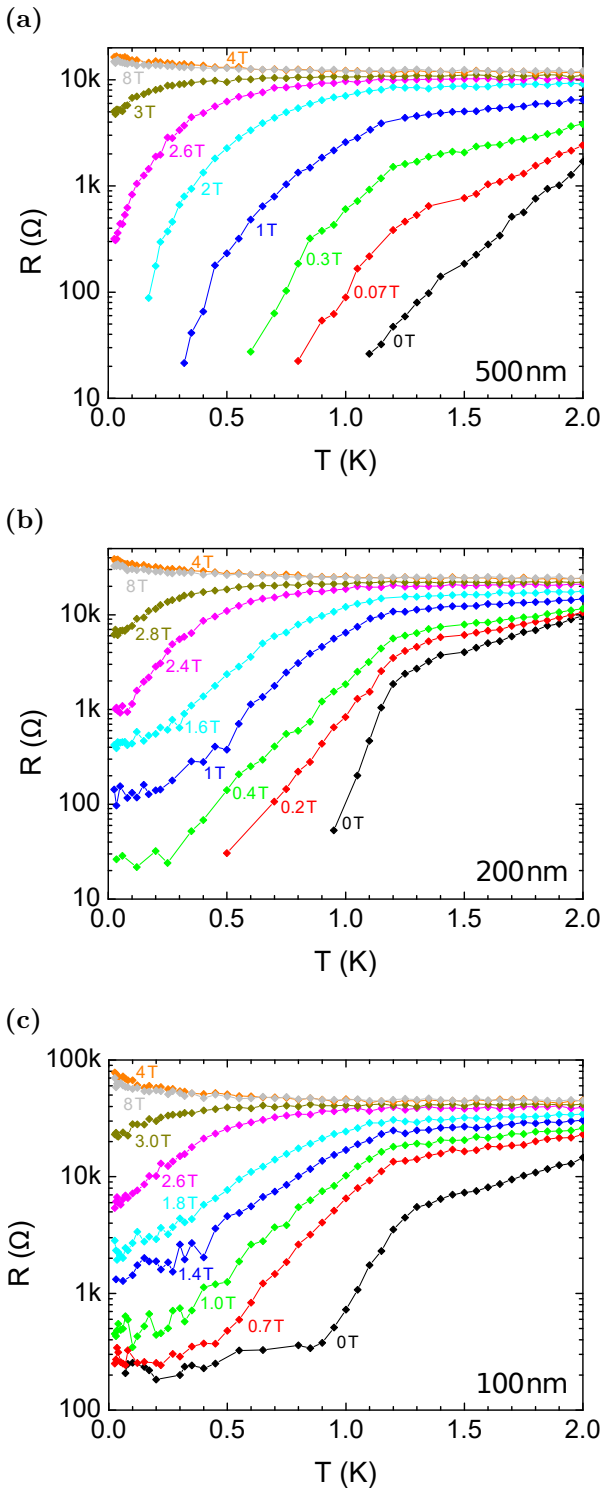

Figure 4.14.: $R(T)$ characteristics of the nominally **(a)** 500 nm, **(b)** 200 nm and **(c)** 100 nm wide samples of chip D03-wd for magnetic fields ranging between $B = 0\,\mathrm{T}$ and $B = 8\,\mathrm{T}$. For the widest sample the typical behavior of a TiN film on the superconducting side with a suppression of T_c for increasing magnetic field is observed. A saturation behavior of the resistance is found for narrower wires.

4.2.3. 50 nm Wide Wire in the Magnetic Field

The behavior of the 50 nm wide wire of chip D03-wd differs generally from the one observed for the wider wires. Figure 4.15(a) shows the $R(T)$ characteristics for several magnetic fields between $B = 0\,\mathrm{T}$ and $B = 8\,\mathrm{T}$. For zero magnetic field an indication of superconductivity appears but then a saturation of the resistance occurs as we also found it in the 100 nm and 200 nm wide samples. When we look at the $B = 0.4\,\mathrm{T}$ curve we still see an indication of superconductivity but interestingly the curve shows a slight upturn when the temperature is decreased below $T \sim 300\,\mathrm{mK}$. Upon increasing the magnetic field this insulating re-entrance behavior becomes more distinct and the resistance at the lowest temperatures finally exceeds the room temperature resistance by about an order of magnitude for magnetic fields between $B \sim 1.4\,\mathrm{T}$ and $B \sim 4\,\mathrm{T}$. However, above $B \sim 2.0\,\mathrm{T}$ the sample resistance shows a monotonic increase for decreasing temperature.

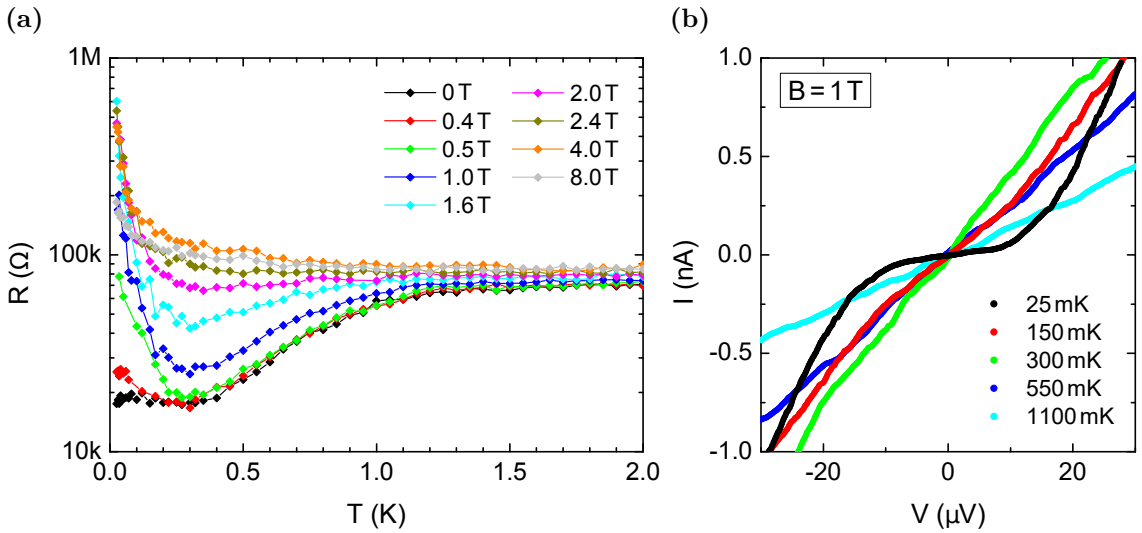

Figure 4.15.: **(a)** $R(T)$ characteristics of the 50 nm wide wire of chip D03-wd for magnetic fields ranging between $B = 0\,\mathrm{T}$ and $B = 8\,\mathrm{T}$. An insulating re-entrance meaning an indication of superconductivity followed by an increase of the resistance upon decreasing the temperature can be observed for certain magnetic fields. **(b)** Temperature evolution of the current-voltage characteristics at $B = 1\,\mathrm{T}$ where the insulating re-entrance is strongly pronounced. A blockaded regime is clearly visible at low temperatures. The curves were smoothed by adjacent averaging of 40 points.

Figure 4.15(b) exemplarily demonstrates for a magnetic field of $B = 1\,\mathrm{T}$ how the insulating re-entrance evolves as a function of temperature in the current-voltage characteristics. When the temperature is decreased the slope of the curves increases as we observe it in superconducting samples. Below a certain temperature a slight bending emerges in the $I(V)$ curves at small voltages. In figure 4.15(b) this is already weakly visible for the red

curve corresponding to $T = 150\,\mathrm{mK}$. Going to lower temperatures the bending becomes more distinct and a blockade-like range with reduced voltage is distinctly visible (see black curve in figure 4.15(b) corresponding to $T = 25\,\mathrm{mK}$).

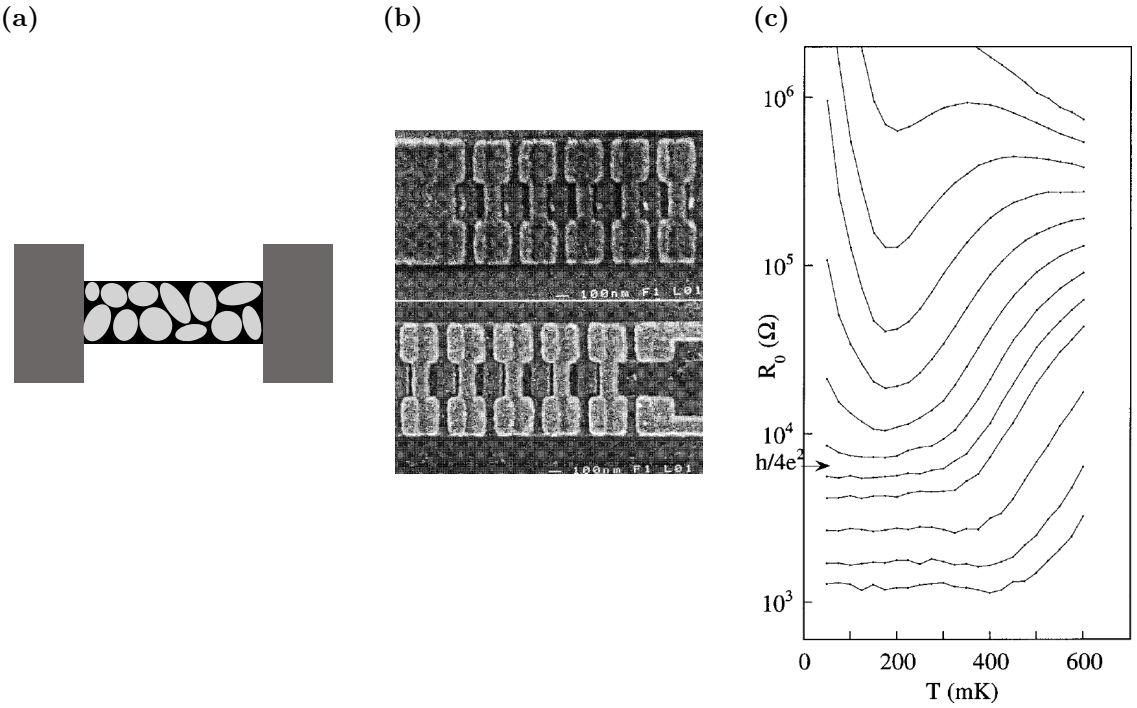

Figure 4.16.: (a) TiN wire modeled as a spontaneously formed random Josephson junction network. The light gray areas represent the superconducting islands which are embedded into an insulating sea indicated in black. **(b)** SEM image of two different arrangements of artificial SQUID arrays as examined by Haviland et al. (from [9]). Al electrodes are connected by Al_2O_3 tunnel barriers. **(c)** $R(T)$ characteristics taken on a one-dimensional artificial Josephson junction array at several values of the magnetic field ranging between $B = 0\,\mathrm{T}$ and $B = 0.64\,\mathrm{mT}$ as presented by Haviland et al. (from [9]). An insulating re-entrance very similar to our data was observed for certain values of the magnetic field.

We can relate our observations to the scenario of random Josephson junction networks and model our wire as a spontaneously formed network of superconducting islands embedded into an insulating sea (see figure 4.16(a)). The insulating re-entrance can then be understood in terms of a magnetic field tuned Josephson coupling energy E_J [106]. The magnetic field effectively reduces the Josephson coupling energy E_J, i.e., the ratio of E_J and the charging energy E_C so that the sample behavior may change from the superconducting to the charging side.

Our data can be compared to the observations on one-dimensional artificial networks realized by serially connected SQUIDS (see figure 4.16(b)). By applying a magnetic flux the phase shift between the neighboring superconducting electrodes was varied which effectively

allows for the tuning of the Josephson coupling energy E_J. For a one-dimensional chain, Haviland et al. [9] found a saturation behavior for zero field and an insulating re-entrance for certain finite fields where E_J is reduced (see figure 4.16(c)). These observations are very similar to our data.

4.3. Chip D03-sar2, 100 nm – The Insulating State and the Influence of a High Impedance Environment

As it was described in section 3.1.4, the chip D03-sar was measured both in a low impedance environment and in an external high impedance environment that was implemented by the use of two additional bias resistors as described in section 3.2.2. In the following we briefly want to present how the change of the environment strongly influences the behavior of the sample, particularly the insulating state, before going over to a detailed analysis of the results obtained for the nominally 100 nm wide of chip D03-sar2 in the external high impedance environment.

4.3.1. Influence of a High Impedance Environment on the Sample Behavior

In the measurements of Haviland et al. on artificial Josephson junction networks [9], a high impedance environment was generally necessary in order to observe an insulating behavior of the arrays. It is argued that quantum fluctuations of the Josephson phase are controlled by the electrodynamic environment which determines whether the samples are on the superconducting or on the insulating side. For our samples we were able to show that an external high impedance environment may strongly enforce the insulating behavior when it already begins to show in a low impedance environment. We deliberately refer to the additional bias resistors as *external* high impedance environment, since we were able to show that it is only a necessary but not a sufficient prerequisite for the observation of highly insulating blockade-like states. The insulating re-entrance of the 50 nm wide wire of chip D03-wd described in the previous sections could for example not be significantly influenced, i.e., enhanced, by a change of the external environment. We will later in this chapter argue and explain that the second necessary part of the required high impedance environment must be developed in the wire itself as a sort of on-chip high impedance environment analog to the on-chip high impedance environment as it was used by Haviland et al [9]. We believe that due to the capacitance to ground of the cryostat leads, the additional bias resistors serve for the filtering of noise from the transimpedance amplifier and therefore create the necessary conditions for an observation of the blockaded regime.

Furthermore, the external high impedance environment allows us to gain access to sections of the current-voltage characteristics where the voltage decreases while the current increases. With the use of two additional bias resistors of each 50 kΩ we are able to resolve such regions as long as $dI/dV > -1/100\,\mathrm{k\Omega}$ despite the application of a voltage bias setup.

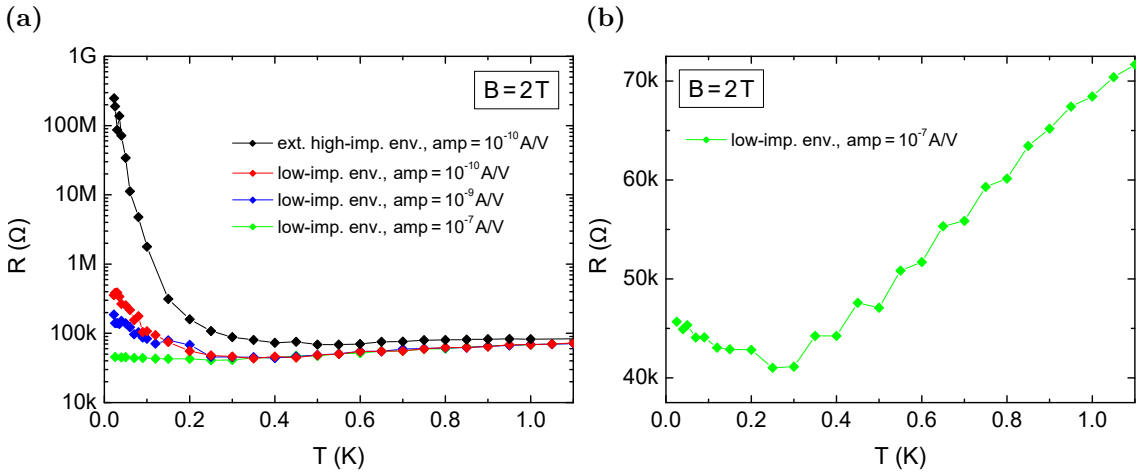

Figure 4.17.: (a) $R(T)$ characteristics of the 100 nm wide wire of sample D03-sar2 at a magnetic field of $B = 2\,\mathrm{T}$. The results obtained with and without additional bias resistors and at several values of the amplification factor are compared. When the sample is embedded in an external high impedance environment, i.e., between two additional bias resistors, the amplification factor has no influence on the sample behavior. **(b)** Zoom in on a linear scale for the curve recorded without additional bias resistors measured with an amplification factor of $10^{-7}\,\mathrm{A/V}$. A slight increase of the resistance at temperatures below $T = 300\,\mathrm{mK}$ is already visible.

Figure 4.17(a) compares the observations without (colored curves) and with additional bias resistors (black curve) in terms of the $R(T)$ characteristics at a magnetic field of 2.4 T for the 100 nm wide wire of chip D03-sar2. Since without additional bias resistors the sample behavior is also considerably influenced by the applied amplification factor of the transimpedance amplifier (see section 3.2.2), we also plot the corresponding obtained curves. We see that an increase of the amplification strongly enforces the insulating behavior and believe that the amplifier noise is responsible for the reduction of the observed phenomena since the noise decreases with higher amplification. For the lowest applied amplification of $10^{-7}\,\mathrm{A/V}$ (green curve) the curve appears flat, i.e., saturated at low temperatures. Figure 4.17(b) shows the behavior of this curve on a smaller and linear scale. We can see that in fact at temperatures below $T = 300\,\mathrm{mK}$ a small but visible rise of the resistance, i.e., a weakly pronounced insulating re-entrance appears. This insulating re-entrance becomes more distinct for higher amplification. For an amplification factor of $10^{-10}\,\mathrm{A/V}$ (red curve in figure 4.17(a)) the resistance at the lowest temperatures exceeds the minimum of the $R(T)$ curve already by an order of magnitude. The effect is by far more pronounced for the black

curve obtained in the external high impedance environment. Here we observe an increase of the resistance by four orders of magnitude in comparison to the curve minimum. The pictured curve was measured at an amplification factor of 10^{-10} A/V. However the samples measured in an external high impedance environment are almost completely insensitive to a change of the amplification. Together with the observation that the amplification factor has a strong influence on the sample behavior, this substantiates our perception that the external bias resistors in combination with the capacitance to ground of the cryostat leads serve for the filtering of the noise from the amplifier.

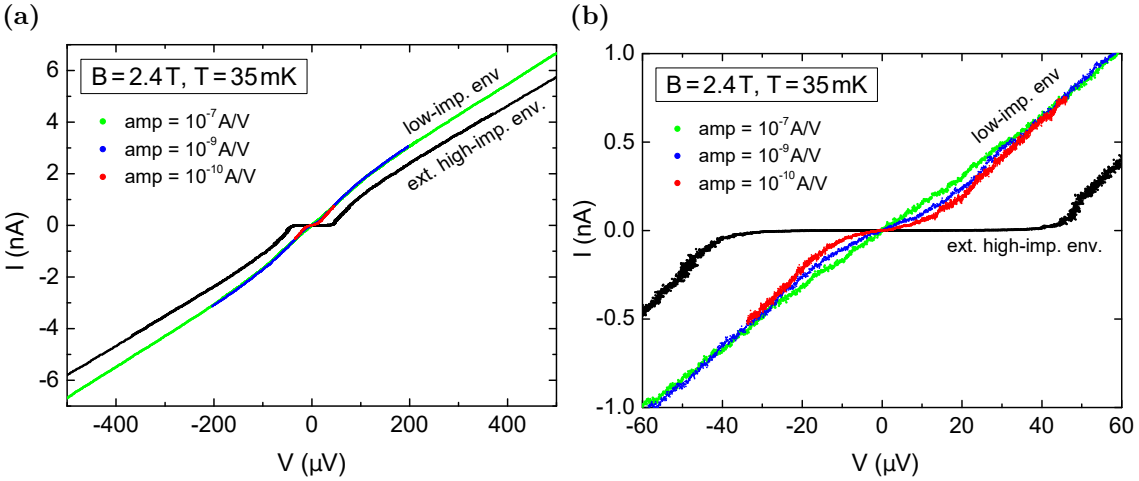

Figure 4.18.: (a) Comparison of the current-voltage characteristics of the 100 nm wide wire of sample D03-sar2 at a magnetic field of $B = 2.4\,\mathrm{T}$ and a temperature of $T = 35\,\mathrm{mK}$ in low and external high impedance environment and for several values of the amplification factor. **(b)** Zoom into the small voltage range. The very pronounced blockaded range showing up in the external high impedance environment becomes strongly washed out in the low impedance environment and appears only as a slight bending in the current-voltage characteristics. The bending becomes more distinct when the amplification factor is increased.

We can also have a look at how the insulating state emerges in the current-voltage characteristics measured in the low impedance and in the external high impedance environment. Figure 4.18(a) shows the $I(V)$ characteristics of the 100 nm wide wire of sample D03-sar2 at a magnetic field of $B = 2.4\,\mathrm{T}$ and a temperature of $T = 35\,\mathrm{mK}$. The black curve presents the measurement in the external high impedance environment. Here the total resistance of the applied series resistors is $100\,\mathrm{k\Omega}$. Hence the voltage axis was recalculated according to

$$V = V_{\mathrm{appl}} - I \cdot 100\,\mathrm{k\Omega} \tag{4.12}$$

in order to obtain the voltage that drops across the wire. V_{appl} is the total applied voltage. This procedure was carried out for all current-voltage characteristics that will be shown in

the following sections. For the low impedance results we again plot the curves obtained for various amplification factors (colored curves). At high voltages the curves measured in the different environments progress almost parallel. The blockade at small voltages appears by far more pronounced when the sample is measured in the external high impedance environment. The blockaded range is much wider and the current is much more suppressed leading to the substantially higher resistances in the $R(T)$ plot. In the low impedance measurement the blockade is washed out and only indicated as a slight bending around zero voltage in the $I(V)$ curves (see enlarged voltage range in figure 4.18(b)). Here the influence of the amplification factor is again visible. The higher the amplification is, i.e., the lower the noise from the amplifier is, the stronger pronounced is the bending of the curve leading to a smaller slope and a higher extracted resistance.

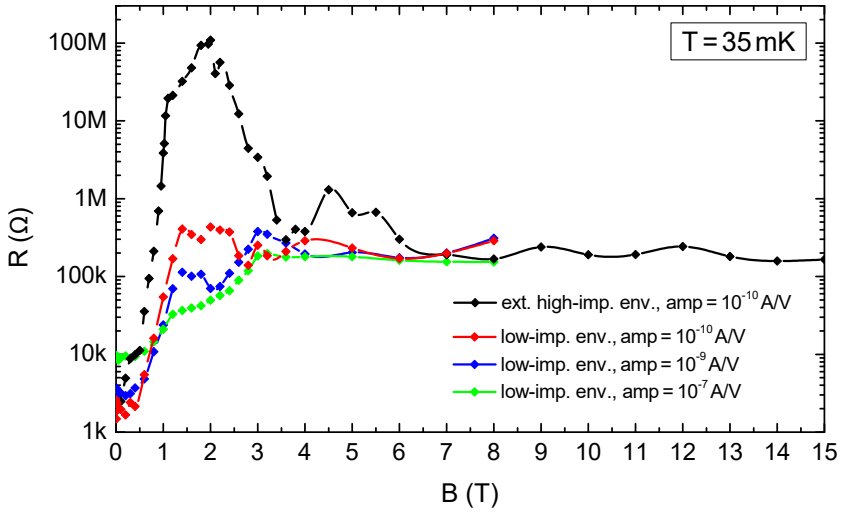

Figure 4.19.: Magnetoresistance curves for a temperature of $T = 35\,\mathrm{mK}$ for the 100 nm wide wire of chip D03-sar in a low (colored curves) and in an external high impedance environment (black curve). In the external high impedance environment a pronounced peak shows up around $B = 2\,\mathrm{T}$ where the resistance exceeds the one observed at zero field by almost five orders of magnitude. This peak is strongly suppressed in the low impedance environment. Here the suppression is the stronger the lower the amplification is.

A comparison of the magnetoresistive behavior of the wire in the different environments (see figure 4.19) also demonstrates impressively the huge impact of the additional bias resistors. From zero field to $B \sim 2\,\mathrm{T}$ the linear resistance measured in the external high impedance environment (black curve) rises by almost five orders of magnitude. The pronounced peak that we observe is suppressed in the low impedance environment. The suppression is the stronger, the lower the amplification is. For an amplification factor of $10^{-10}\,\mathrm{A/V}$ an indication of the peak is still visible. At this point we want to mention that the amplification factor also reflects in the behavior of the sample on the superconducting side, i.e., the

low field behavior of the sample. For higher amplification smaller resistances are reached. The green curve in figure 4.19 obtained at an amplification factor of $10^{-7}\,\mathrm{V/A}$ saturates at $R \sim 10\,\mathrm{k\Omega}$ for low fields instead of dropping to lower resistance values like the other curves. This is a general observation that we also made on wider samples that are fully on the superconducting side. In general we can say that both the superconducting and the insulating behavior is suppressed and less distinct when small amplification factors are employed.

4.3.2. The Insulating Re-Entrance and the Duality of the Current-Voltage Characteristics

The 100 nm wide wire of chip D03-sar2 qualitatively displays a very similar temperature evolution of the resistance in zero and finite magnetic field (see figure 4.20(a)) as the 50 nm wide wire of chip D03-wd that we discussed in section 4.2.3: at zero field an indication of superconductivity appears but the resistance remains finite and saturates around $R \sim 4\,\mathrm{k\Omega}$. Also for finite magnetic fields up to $B \sim 2.4\,\mathrm{T}$ superconducting correlations develop in an intermediate temperature regime of $T \sim 0.3\,\mathrm{K} - 1\,\mathrm{K}$ with decreasing temperature. For lower temperatures an upturn of the resistance and a very similar re-entrant insulating phase as described previously for the other sample is visible. However for the 100 nm wide wire of chip D03-sar2 we were able to strongly enhance the insulating behavior by the employment of the external high impedance environment which was not possible for the other wire. For magnetic fields around $B \sim 2\,\mathrm{T}$ the resistance at the lowest temperatures exceeds the minimum of the $R(T)$ curve by four orders of magnitude. Again our observations strongly resemble the current-voltage characteristics observed for artificial one-dimensional Josephson junction arrays (see figure 4.16(c)) [9].
The degree of insulation and also the capability of an enhancement by an external high impedance environment varies strongly from device to device. Even though it is more common in the narrower wires there is no systematic dependence on the wire width or geometry. This observation suggests that the insulating behavior is not solely controlled by the wire size but also by sample specific fluctuations resulting from different spatial distributions of the superconducting order parameter (see section 2.4.2).
The blue curve in figure 4.20(b) exemplarily depicts for a magnetic field of $B = 2.4\,\mathrm{T}$ and a temperature of $T = 35\,\mathrm{mK}$ how dramatic the highly insulating state emerges in the current-voltage characteristics as a strongly blockaded voltage regime up to $V \sim 40\mu\mathrm{V}$. The black Josephson curve measured in zero field with the missing maximum of the current is similar to the zero field current-voltage characteristics obtained for the 50 nm wide wire of chip D03-wd (see section 4.1.2) that we discussed earlier. The comparison of the two

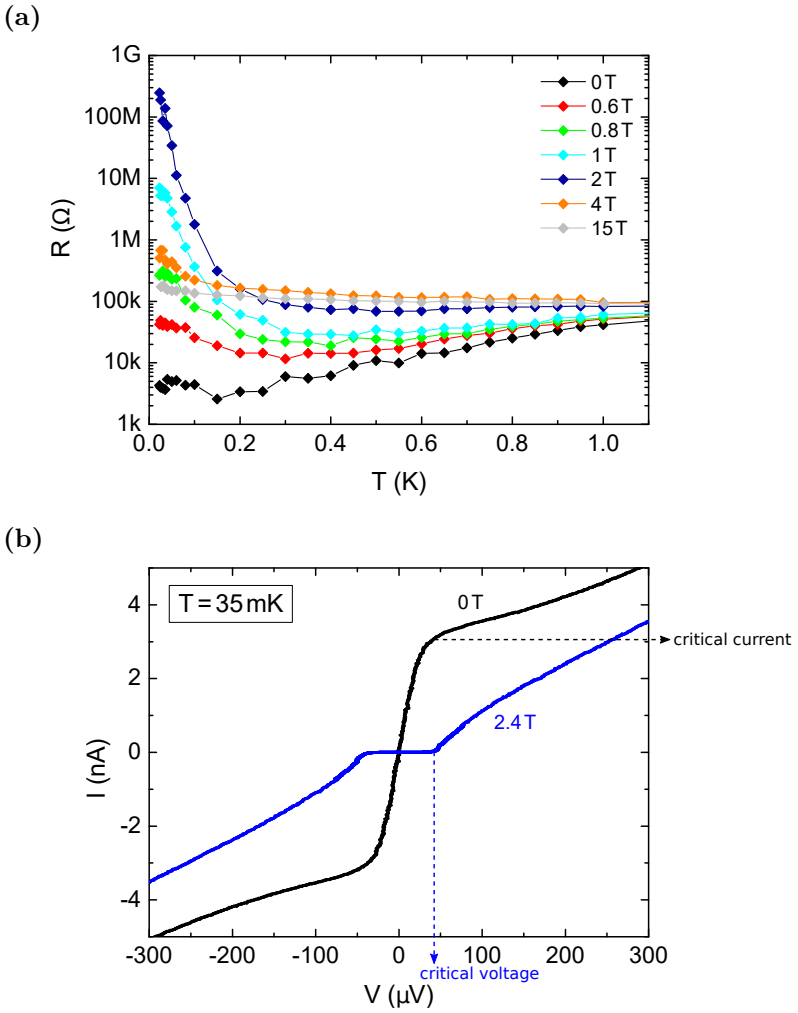

Figure 4.20.: **(a)** $R(T)$ characteristics of the 100 nm wide wire of sample D03-sar2 for magnetic fields ranging from $B = 0\,\mathrm{T}$ to $B = 15\,\mathrm{T}$. Qualitatively the sample shows a similar behavior as the 50 nm wide wire of chip D03-wd (see section 4.2.3). For certain magnetic fields we observe an insulating re-entrance with an indication of superconductivity followed by an increase of the resistance when the temperature is lowered. The insulation was strongly enhanced by the employment of an external high impedance environment. **(b)** Duality between a superconducting current-voltage characteristic measured at $B = 0\,\mathrm{T}$ (black curve) and an insulating one measured at $B = 2.4\,\mathrm{T}$ (blue curve). Dual to the supercurrent branch in the Josephson like curve which is characterized by a critical current we observe a blockaded range in the insulating $I(V)$ type which is characterized by a critical voltage.

curves illustrates the duality between the superconducting and the insulating states with regard to their manifestations in the observed $I(V)$ curves. The blockaded voltage range observed for $B = 2.4\,\mathrm{T}$ which is characterized by a critical voltage has the dual character to the supercurrent branch observed at zero field which is characterized by a critical current. This duality of the current-voltage characteristics was also observed by Haviland et al. in their data obtained for artificial one-dimensional Josephson junction arrays [9]. They very clearly demonstrated the expected duality of charge and flux that originates from the uncertainty relation that is valid for these quantum variables. A sharply defined number difference of Cooper pairs across the junction involves large quantum fluctuations of the phase and vice versa. The quantum fluctuations of the phase are in turn controlled by the electrodynamic environment. The transition from Josephson-like to Coulomb blockade curves was induced by a variation of the Josephson coupling to charging energy ratio whereby the ratio required for the transition strongly depended on the array length. For long arrays, i.e., arrays with a large number of junctions, a Coulomb blockade was even observable for $E_J \geq E_C$.

4.3.3. Evolution of the Current-Voltage Characteristics and the Critical Voltage in the Magnetic Field

We want to have a closer look at the evolution of the current-voltage characteristics obtained in the external high impedance environment for the 100 nm wide wire of chip D03-sar with the temperature and with the magnetic field. Figure 4.21(a) shows the $I(V)$ curves for a temperature of $T = 35\,\mathrm{mK}$ and magnetic fields ranging from $B = 0\,\mathrm{T}$ to $B = 15\,\mathrm{T}$. We see that our current-voltage characteristics develop a nonlinearity in form of a slight bending around zero voltage at small but finite fields. At $B = 0.6\,\mathrm{T}$ this is already clearly visible. For higher fields $B \geq 0.9\,\mathrm{T}$ the bending turns into a distinct blockaded voltage range. This range increases upon further increasing the magnetic field and a maximum of the width is reached at magnetic fields around $B = 2\,\mathrm{T}$ to $B = 2.4\,\mathrm{T}$. At the same time the slope within the blockaded range decreases giving rise to the high extracted linear resistances presented in figure 4.19 and 4.20(a). For higher magnetic fields the blockade becomes smeared out and the slope around zero voltage increases again, i.e., the linear resistance decreases. Remarkably at the highest accessible magnetic field of $B = 15\,\mathrm{T}$ we still see a slight nonlinearity in the current-voltage characteristic.
At fields around $B = 1.8\,\mathrm{T}$ to $B = 2.4\,\mathrm{T}$ a pronounced Bloch nose (see section 2.3.2) appears as it was also observed in single Josephson junctions where the coupling of the junction to the electromagnetic environment was tuned by the flux through one-dimensional SQUID chain leads [67, 61]. Here a Coulomb blockade accompanied by a Bloch nose, which as

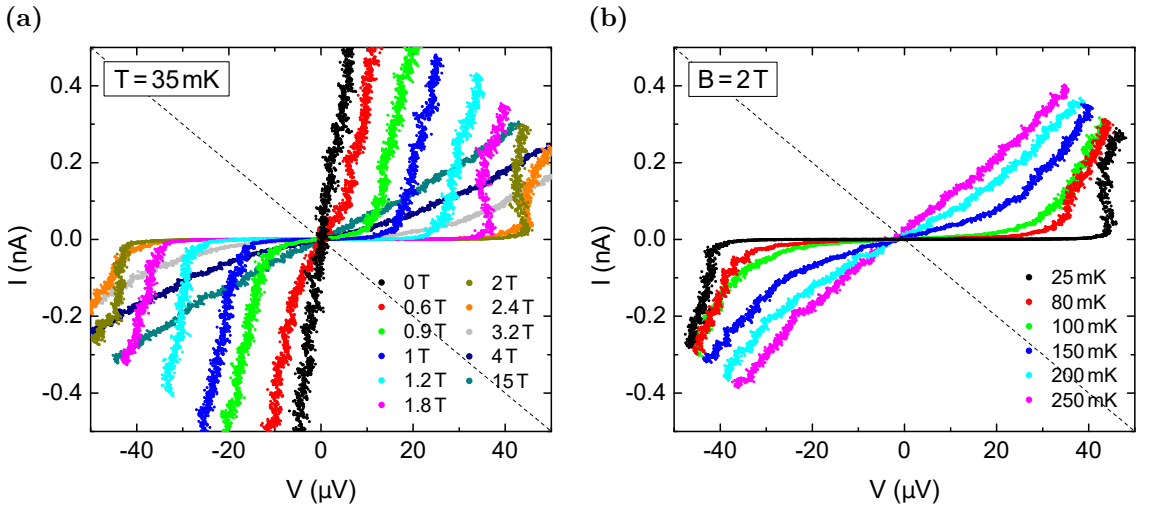

Figure 4.21.: (a) Evolution of the current-voltage characteristics with the magnetic field at a temperature of $T = 35\,\mathrm{mK}$. In the magnetic field a blockaded range develops which is most distinct at magnetic fields around $B = 2\,\mathrm{T}$ and $B = 2.4\,\mathrm{T}$. We observe a Bloch nose for magnetic fields between $B = 1.8\,\mathrm{T}$ and $B = 2.4\,\mathrm{T}$. The dashed line shows a slope of $-(100\,\mathrm{k\Omega})^{-1}$ and indicates the range where the negative differential resistance in the Bloch regime is made accessible by the use of the two external bias resistors of each $50\,\mathrm{k\Omega}$. **(b)** Evolution with the temperature at a magnetic field of $B = 2\,\mathrm{T}$. The blockaded range of the $I(V)$ curve is smeared out with increasing temperature. The dashed line again indicates the accessible Bloch regime.

Watanabe et al. quote gives evidence for single Cooper pair tunneling, was induced when the resistance of the SQUID arrays was sufficiently increased. As already explained, we can observe this Bloch nose in our voltage bias setup because of the use of the external high impedance environment. The dashed lines in figure 4.21(a) and 4.21(b) exhibit a slope of $-(100\,\mathrm{k\Omega})^{-1}$ and indicate the range of negative differential resistance in the Bloch regime that is made accessible by the use of the two external bias resistors of each $50\,\mathrm{k\Omega}$. Figure 4.21(b) shows the temperature evolution of the current-voltage characteristics at a magnetic field of $B = 2\,\mathrm{T}$, i.e., the maximum of the magnetoresistance. For increasing temperature the observed Bloch nose is gradually suppressed and the blockaded range is smeared out.

Dual to the superconducting side where we extracted a critical current (see figure 4.4 and 4.13(a)) we can extract a corresponding critical voltage from the insulating current-voltage characteristics. The temperature dependence of the critical voltage V_c is presented in figure 4.22(a) for three exemplary magnetic fields. With the saturation at low temperatures and the gradual decrease for higher temperatures, V_c shows a similar temperature evolution as the critical current I_c on the superconducting side as we also expect it for duality reasons. The magnetic field dependence of V_c qualitatively follows the evolution of the magnetoresistance (see figure 4.19) with the same position of maxima and minima. The

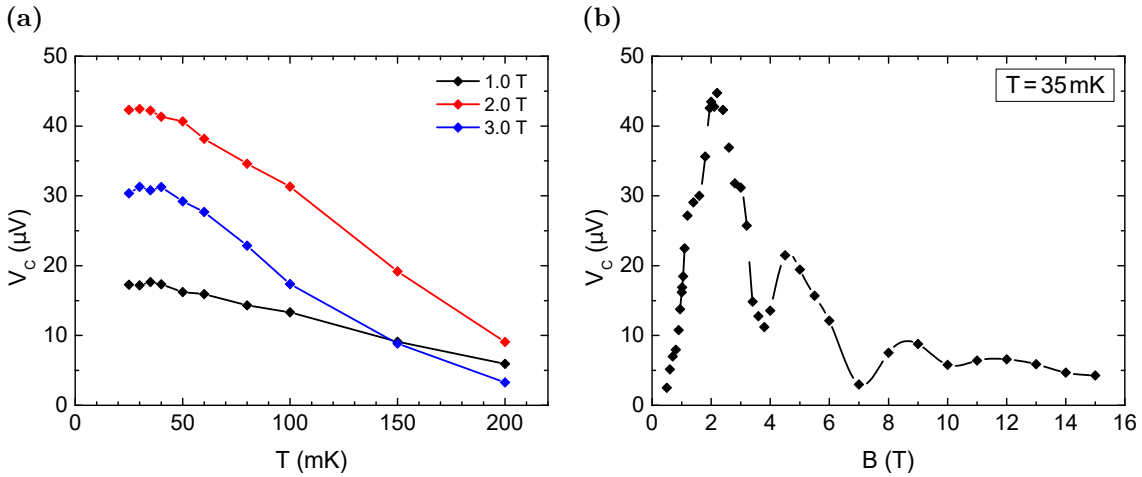

Figure 4.22.: (a) Temperature evolution of the critical voltage V_c as extracted from the current-voltage characteristics for three magnetic fields. The saturation at low temperatures and the gradual decrease for higher temperatures is similar to the temperature dependent evolution of the critical current on the superconducting side as we expect it from duality. **(b)** The magnetic field dependence of the critical voltage qualitatively follows the magnetoresistive behavior of the sample. It shows a typical modulation on a field scale of $\sim 3\,\mathrm{T}$ which corresponds to a size of a typical plaquette of $\sim 26\,\mathrm{nm}$ that encloses magnetic flux.

modulation happens on a typical fields scale of $\sim 3\,\mathrm{T}$. Based on this observation we can estimate the size of a typical plaquette that encloses magnetic flux as

$$\frac{\Phi_0}{(26\,\mathrm{nm})^2} \sim 3\,\mathrm{T}. \tag{4.13}$$

The obtained plaquette size of $\sim 26\,\mathrm{nm}$ is reasonable when we compare it to the wire width of $w = 100\,\mathrm{nm}$ which is about three times the coherence length of our material (see section 3.1.1).

4.3.4. Dual Ivanchenko-Zil'berman Modeling

Our observations on the 100 nm wide wire of chip D03-sar2 in the external high impedance environment in the insulating regime, strongly resemble the behavior of single Josephson junctions embedded between high impedance SQUID chains that serve as leads as it was presented by Corlevi et al. (see figure 2.10) [67]. Our obtained current-voltage characteristics, their temperature behavior as well as the $R(T)$ dependence observed for various values of the magnetic field, in particular the re-entrant insulating behavior, show strong similarities to what was observed in artificial systems. However, we were also able to demonstrate, that

the employment of an external high impedance environment is not necessarily sufficient to generate this kind of behavior since for example the nominally 50 nm wide wire of chip D03-wd did not show any enhancement of the insulating state when additional bias resistors were used even though it looked promising in the low impedance measurements. To explain this sample dependency we can tie in with our model of a spontaneously formed random Josephson junction network (see figure 4.16(a)). We now adapt it as presented in figure 4.23 with the biggest parts of the wire serving as additional but naturally formed high impedance leads which are directly coupled to a hot spot area in the wire. These sort of on-chip high impedance leads are necessary for the observation of a strong Coulomb blockade and are analog to the on-chip high impedance SQUID chains as they were used by Corlevi et al [67]. The applied magnetic field leads to a suppression of the local Josephson coupling whereby quantum phase slips are enabled that result in the observed strongly insulating behavior.

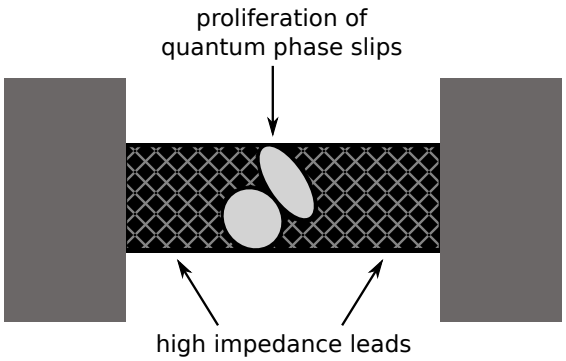

Figure 4.23.: TiN nanowire modeled as a spontaneously formed random Josephson network where the biggest parts of the wire serve as high impedance leads which are directly coupled to a hot spot area in the middle of the wire where quantum phase slips are proliferated. This concept forms the natural analog to the artificial systems of single Josephson junctions embedded between high impedance SQUID chains as it was investigated by Corlevi et al. [67].

Analog to the Ivanchenko-Zil'berman modeling that was done on the superconducting side at zero field (see section 4.1.4) we can fit our insulating current-voltage characteristics with the dual expression given in equation 2.39 as it was also done by Corlevi et al. for the data obtained on a single Josephson junction embedded in high impedance environments [67]. Dual to the subtraction of a current through a parallel resistor (see equation 4.8 and figure 4.6) we subtract a voltage drop across a series resistor R_N from our measured current-voltage characteristic now before doing the actual fitting routine. Thereby the voltage axis rescales to

$$V = V_{\text{total}} - V_N = V_{\text{total}} - IR_N \tag{4.14}$$

where V_{total} denominates the total voltage that was applied in our measurement setup.[2] Again we do not use a fixed value for R_N but keep it a free fit parameter. Dual to the notation used in section 4.1.4, V will always denote the voltage after the subtraction of the normal state voltage V_N within this chapter for an easier notation.

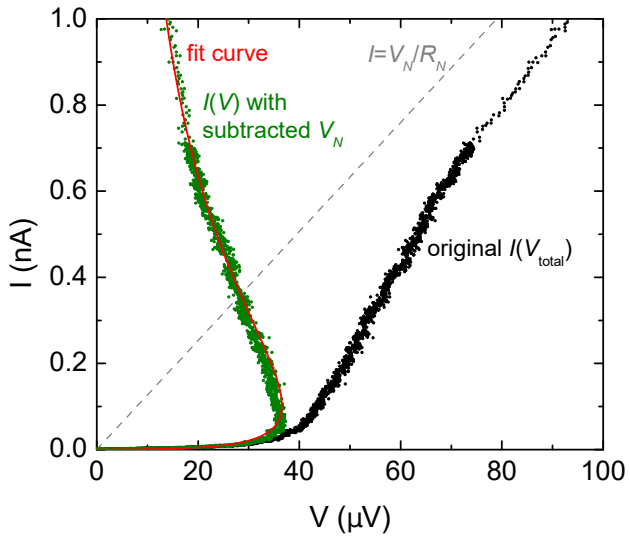

Figure 4.24.: Demonstration of the subtraction of the normal state voltage V_N for a magnetic field of $B = 2.4\,\text{T}$ and a temperature of $T = 40\,\text{mK}$. The black curve is the original current-voltage characteristic as it was recorded in the measurement (after the subtraction of the additional series resistors that serve for the high impedance environment). The gray dashed line represents the ohmic part of this curve corresponding to the normal state resistance R_N of the sample. A subtraction of this voltage contribution from the original characteristic yields the green curve. The red line depicts the fit curve obtained by the dual Ivanchenko-Zil'berman modeling.

The subtraction of V_N is demonstrated exemplarily for a magnetic field of $B = 2.4\,\text{T}$ and a temperature of $T = 40\,\text{mK}$ in figure 4.24. The black curve depicts the measured original current-voltage characteristic $I(V_{\text{total}})$. The gray dashed line corresponds to the normal state voltage V_N which is subtracted from the original $I(V_{\text{total}})$ in order to obtain the green $I(V)$ curve. This curve is then fitted by the Ivanchenko-Zil'berman routine which yields the red fit curve.
The magnetic field dependence of the values obtained for R_N is plotted in figure 4.25(a) as blue squares opposed to the magnetoresistance curve of the wire (black diamonds). In figure 4.25(b) we compare these values (dashed lines) to the temperature dependence of the sample for some selected magnetic fields (diamonds). The values resulting for R_N equal approximately the minimum of the $R(T)$ curves for the specific magnetic fields which is

[2] Note that V_{total} in fact refers to the total applied voltage *after* the subtraction of the voltage drop across the two employed external serial bias resistors of each $50\,\text{k}\Omega$.

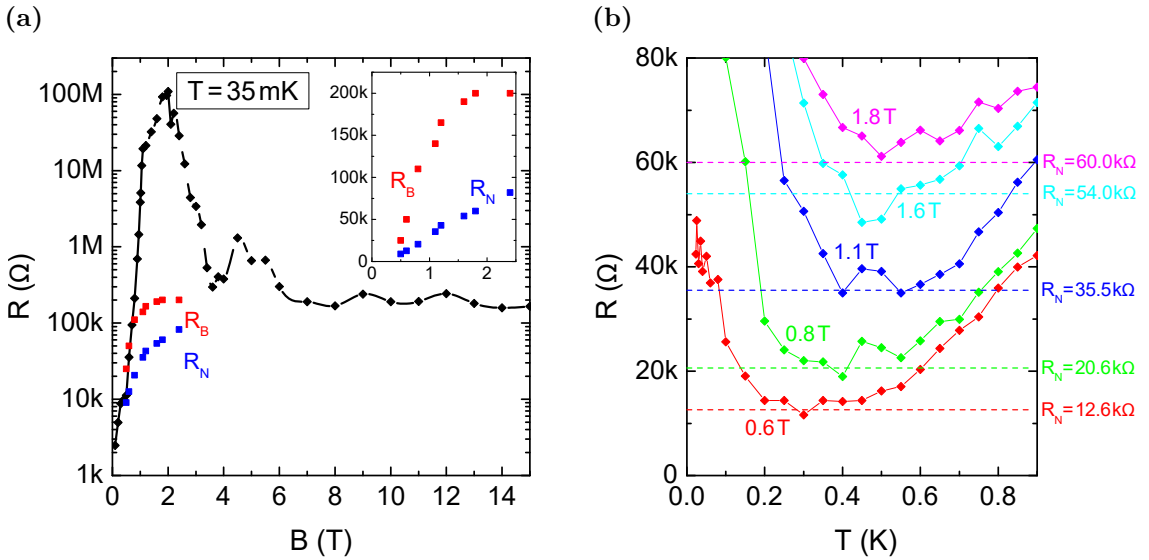

Figure 4.25.: (a) Magnetic field dependence of the fit parameters R_B and R_N obtained through the dual Ivanchenko-Zil'berman modeling. The parameters are compared to the magnetoresistance curve of the wire (black diamonds). The inset shows the magnetic field dependence of R_B and R_N but on a linear resistance scale. As we can see in **(b)** R_N equals approximately the minimum of the $R(T)$ curve for the specific magnetic field which is where the current-voltage characteristics start to display a linear behavior. This is analog to the values resulting for R_N from the Ivanchenko-Zil'berman fits on the superconducting side (see figure 4.7(a)). The temperature dependence of the wire resistance is plotted as diamonds and the associated values of R_N for the specific magnetic fields are sketched as dashed lines in the same color.

where the current-voltage characteristics start to exhibit a linear behavior. This is analog to the values of R_N resulting from the Ivanchenko-Zil'berman fits on the superconducting side (see figure 4.7(a)).

The fitting routine proceeds in a manner analogous to the superconducting side as presented in section 4.1.4 and appendix B. In the following we will explain the dual modifications of the theory which are necessary in order to properly model our system. As on the superconducting side, we may not assume a constant environmental impedance $Z(\omega) = const.$ over the whole frequency range as it was supposed by Ivanchenko and Zil'berman. In contrast we propose a frequency dependent environment which is modeled in dual to the superconducting side as an impedance $Z(\omega)$ in series to the junction as it is sketched in the equivalent circuit in figure 4.26. In the case of $\omega = 0$ the real part of this impedance is identical to the normal state resistance R_N which is a serial dc resistance. At the plasma frequency $\omega = \omega_p$ the real part of the impedance $Z(\omega)$ is identical to R_B which is a serial ac resistance:

$$\mathrm{Re}(Z(\omega)) = \begin{cases} R_N & \omega = 0 \\ R_B & \omega = \omega_p \end{cases} . \tag{4.15}$$

In order to correctly model the behavior of our experiment we therefore have to subtract a current through a parallel resistance R_B as it is implied in the Ivanchenko-Zil'berman relation from the $I_{B_{IZ}}(V)$ curve resulting from equation 2.39.

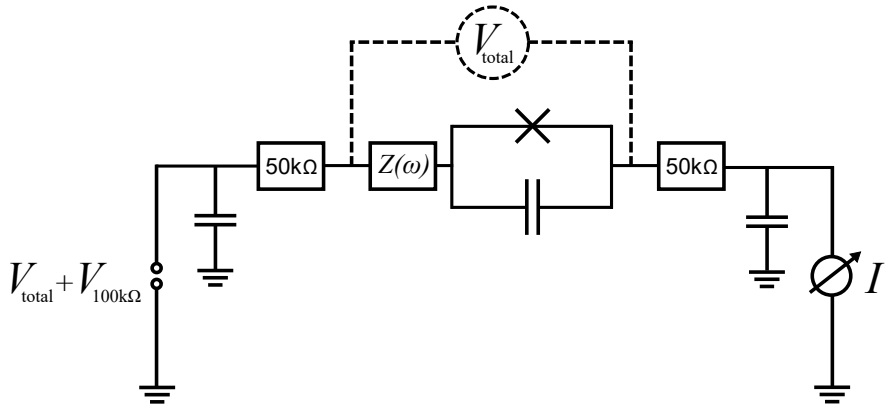

Figure 4.26.: Equivalent circuit for our experiment. The resistance of the environment is sketched as a frequency dependent impedance $Z(\omega)$ in series to the junction. V_{total} refers to the total applied voltage *after* the subtraction of the voltage drop across the two employed external serial bias resistors of each 50 kΩ.

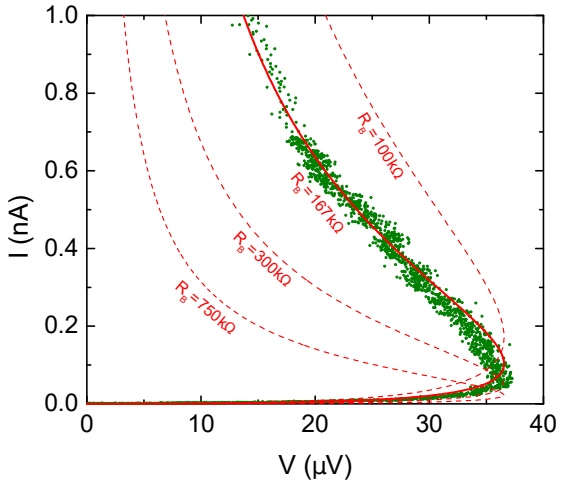

Figure 4.27.: Current-voltage characteristic measured at a magnetic field $B = 2.4\,\text{T}$ and a temperature $T = 40\,\text{mK}$ (green) compared to various fit curves resulting from the adapted Ivanchenko-Zil'berman relation for several values ob R_B which influence the broadening of the voltage peak (red). The solid red curve for $R_B = 167\,\text{k}\Omega$ matches the progression of the experimental data.

In figure 4.27 the influence of R_B within the modified Ivanchenko-Zil'berman model is illustrated. We compare the measurement curve obtained at a magnetic field $B = 2.4\,\text{T}$ and a temperature $T = 40\,\text{mK}$ (green) to the fit curves resulting from the dual Ivanchenko-

Zil'berman relation with the described adaptation for various values of R_B (red) which influence the broadening of the voltage peak. The solid red curve corresponding to $R_B = 167\,\mathrm{k\Omega}$ exhibits the correct zero voltage slope and the correct broadening. The obtained values for R_B are plotted as a function of the magnetic field in figure 4.25(a) (red squares) compared to the magnetoresistance curve of the wire (black dots) and the values obtained for the normal state resistance R_N (blue squares) on a logarithmic scale. The inset opposes the two parameters on a linear scale. In contrast to the superconducting side, R_B is now comparable to R_N.
In our fitting routine we again replace the actual temperature in the Ivanchenko-Zil'berman relation (equation 2.39) by an effective temperature and dual to the superconducting side the intrinsic critical voltage V_0 may now decrease for temperatures outside of the low temperature limit where it must stay constant. Together with the modifications that we explained earlier, the dual Ivanchenko-Zil'berman relation finally transforms to

$$V(I_{B_{IZ}}) = V_0\,\mathrm{Im}\left[\frac{\mathfrak{I}_{1-i\beta e I_{B_{IZ}} R_B/\pi}(\beta E_S)}{\mathfrak{I}_{-i\beta e I_{B_{IZ}} R_B/\pi}(\beta E_S)}\right],\ \beta = \frac{1}{k_B T_{\mathrm{eff}}},\ I = I_{B_{IZ}} - V/R_B. \tag{4.16}$$

When we apply the adapted dual Ivanchenko-Zil'berman model to our magnetic field dependent current-voltage characteristics recorded at a temperature $T = 35\,\mathrm{mK}$ we obtain good results starting at $B \sim 0.5\,\mathrm{T}$ in the ascending part of the magnetoresistance, i.e., up to $B \sim 2.4\,\mathrm{T}$. The measurement data (dots) and the curves resulting from the fitting procedure (lines) are presented in figure 4.28(a) for magnetic fields of $B = 0.8\,\mathrm{T}$, $1.2\,\mathrm{T}$ and $2.4\,\mathrm{T}$. As an effective temperature that corresponds to the set cryostat temperature of $T = 35\,\mathrm{mK}$ we obtain $T_{\mathrm{eff}} \sim 60\,\mathrm{mK}$ which is much less than in the Ivanchenko-Zil'berman fits on the superconducting side where a saturation of the effective temperature at the lowest reachable temperatures was observed around $T_{\mathrm{eff}} \sim 400\,\mathrm{mK}$. Here we attributed the high saturation values to the appearance of quantum phase slips which avoid the experimental observation of higher critical currents and actually increase the effective temperature emerging through the fitting procedure. Now on the insulating side the high impedance environment favors the occurrence of quantum phase slips which enables comparably high experimentally observable critical voltages and therefore lower saturation values of the effective temperature. The value of the effective temperature $T_{\mathrm{eff}} = 60\,\mathrm{mK}$ that we find in the dual Ivanchenko-Zil'berman modeling can most likely be attributed to an increased electron temperature compared to the bath temperature of the cryostat that results from insufficient filtering of the measurement lines.
Figure 4.28(b) shows the intrinsic critical voltage V_0 (filled circles) that emerges from the fitting procedure as far as we can determine it. It is opposed to the critical voltage V_0 that was directly extracted from the current-voltage characteristics (see also 4.22(b)). We

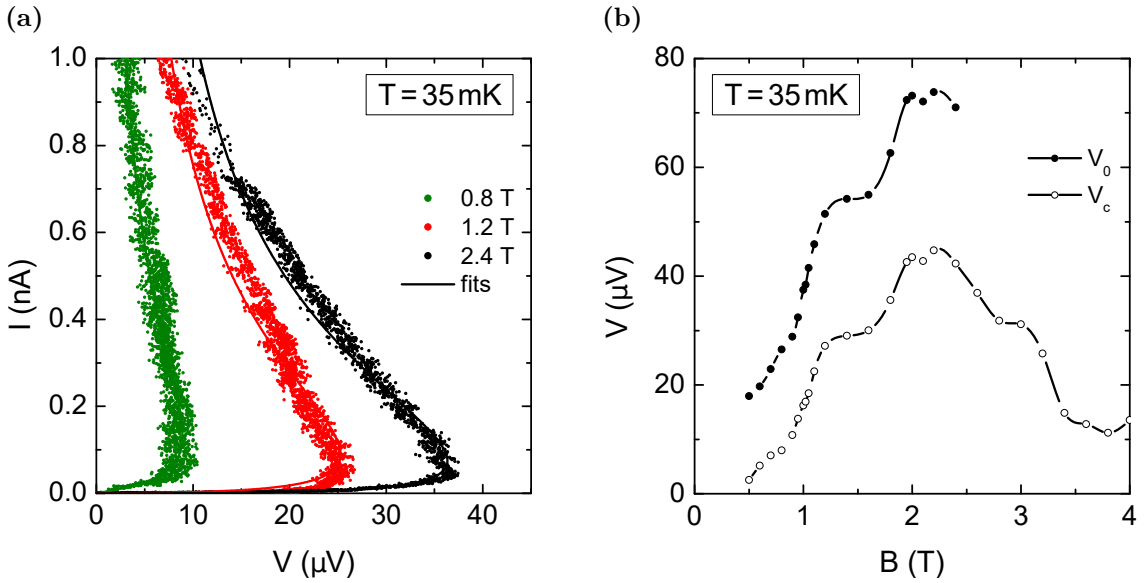

Figure 4.28.: (a) Measurement curves (dots) and corresponding dual Ivanchenko-Zil'berman fits (lines) for a temperature of $T = 35\,\mathrm{mK}$ and magnetic fields of $B = 0.8\,\mathrm{T}$, $1.2\,\mathrm{T}$ and $2.4\,\mathrm{T}$. Through the fitting procedure we obtain $T_{\mathrm{eff}} = 60\,\mathrm{mK}$ as an effective temperature which is considerably higher than the values of T_{eff} that were found for the lowest achievable temperatures on the superconducting side. **(b)** Magnetic field dependence of the resulting fit parameter V_0, i.e., the intrinsic critical voltage as far as it is determinable with comparison to the values of the critical voltage values that were directly extracted from the measurement data. V_0 is about two to four times higher, similar to the observations concerning the critical current on the superconducting side.

observe that the intrinsic critical voltage qualitatively follows the observable critical voltage but is about two to four times higher similar to what we observed on the superconducting side for the critical current and the intrinsic critical current (see figure 4.11(a)).

In addition we can fit the current-voltage curves at fixed magnetic fields as a function of temperature in the field range between $B \sim 0.5\,\mathrm{T}$ and $B \sim 2.4\,\mathrm{T}$. A selection of temperature dependent characteristics for $B = 0.8\,\mathrm{T}$, $1.1\,\mathrm{T}$ and $2.4\,\mathrm{T}$ (dots) with the corresponding fit curves (lines) is presented in figure 4.29. At $B = 2.4\,\mathrm{T}$ where the blockade is most strongly pronounced, reasonable results can be obtained up to $T \sim 350\,\mathrm{mK}$. For higher temperatures the measurement curves after the subtraction of the normal state voltage V_N show a progression which is too flat for a reasonable adjustment of the fit curve. For smaller fields the fits are limited to a smaller temperature range.

The effective temperature T_{eff} obtained through the dual fitting procedure it presented in figure 4.30(a) for the three exemplary fields as a function of the set cryostat temperature T. For all investigated magnetic fields the effective temperature equals the set cryostat temperature down to $T \sim 100\,\mathrm{mK}$ followed by a saturation of the effective temperature around $T_{\mathrm{eff}} \sim 60\,\mathrm{mK}$ which is consistent with the outcome on the magnetic field dependent fits

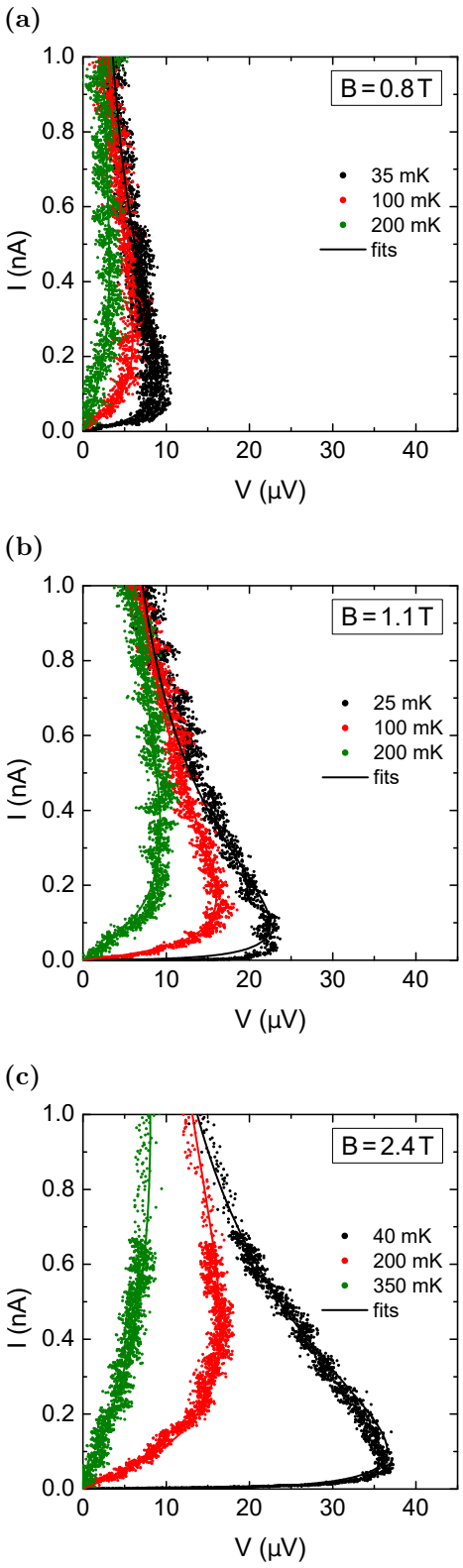

Figure 4.29.: Measured current-voltage characteristics (dots) and corresponding dual Ivanchenko-Zil'berman fits (lines) for magnetic fields of **(a)** $B = 0.8\,\mathrm{T}$, **(b)** $B = 1.1\,\mathrm{T}$ and **(c)** $B = 2.4\,\mathrm{T}$ each at various temperatures.

that were done for $T = 35\,\mathrm{mK}$ as presented before. For all magnetic fields the $T_{\mathrm{eff}}(T)$ dependence progresses in the same way without any significant deviations. This supports our understanding that the effective temperature here solely depends on extrinsic conditions like an increased electron temperature compared to the bath temperature. We present the temperature dependence of the intrinsic critical voltage V_0 (filled symbols) again for three different magnetic fields in figure 4.30(b) and compare it again to the experimentally observed values of the critical voltage V_c (open symbols). V_0 is constant up to temperatures of $T \sim 200\,\mathrm{mK}$. At magnetic fields where a fitting is possible up to higher temperatures a decrease of V_0 is observed similar to the behavior of the intrinsic critical current on the superconducting side (see figure 4.11(a)).

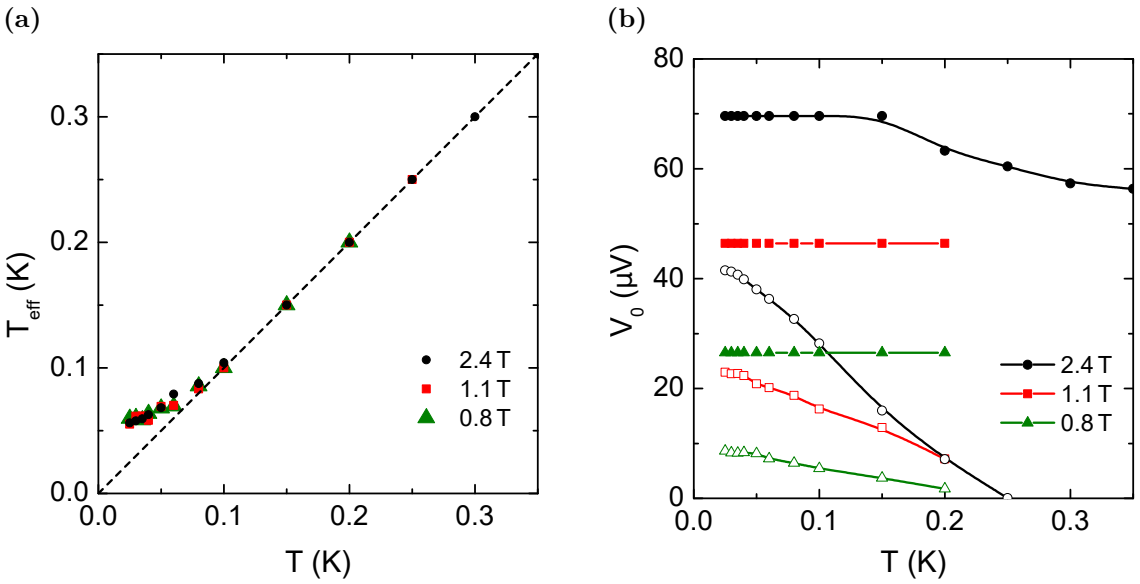

Figure 4.30.: (a) Effective temperature T_{eff} as a function of the set cryostat temperature T as we obtain it from the dual Ivanchenko-Zil'berman fits. For all magnetic fields the values progress in the same way and saturate at $T_{\mathrm{eff}} \sim 60\,\mathrm{mK}$. **(b)** Intrinsic critical voltage as a function of temperature (filled symbols) compared to the observed experimental values of the critical voltage V_c (open symbols). V_0 stays constant up to $T \sim 200\,\mathrm{mK}$ and descends for higher temperatures similar to what we observed for the instrinsic critical current on the superconducting side.

CHAPTER 5

Summary and Outlook

For the understanding of the behavior of polycrystalline TiN thin films that undergo a superconductor-insulator transition, the Josephson junction array is a possible model system [5, 6, 7, 8]. A naturally formed Josephson junction network may arise through an electronic fragmentation of the film and the formation of self-organized superconducting islands. One of the core motivations of this work was the question of what the consequences of such an electronic fragmentation are when the structure size is decreased to the submicron range. In our experiments, we observed a number of effects that were so far only limited to the experimental work on single Josephson junctions and artificial one-dimensional arrays. Furthermore we were able to demonstrate the striking duality between the behavior of narrow TiN wires on the superconducting and on the insulating side which is based on the duality of charge and phase. We want to sum up our results in the following.

Samples

In the framework of this thesis we investigated TiN nanostructures with widths between $\sim 780\,\mathrm{nm}$ and $\sim 50\,\mathrm{nm}$ close to the superconductor-insulator transition. The samples were fabricated from a TiN polycrystalline film with a thickness $t = 3.6\,\mathrm{nm}$. A processing method was developed that allows for the fabrication of high resolution TiN structures out of the film down to a width of about ten nanometers. We applied the technique of

crosslinking PMMA [87] where in our case the resist was exposed to electron beam doses of 30000 $\mu C/cm^2$. Hereby large molecules are composed in the PMMA whereby it becomes resistant to solvents and may protect the TiN during the later physical argon ion beam etching.
By means of this fabrication method several chips were processed where series of TiN nanowires and microstructures of various sizes were arranged. Two of these chips were the subject to the later measurements on the electric transport properties of the samples and a detailed analysis. On chip D03-wd (**w**idth **d**ependence) we processed TiN structures with a fixed length ($l \sim 780\,\mathrm{nm}$) but varying widths ($50\,\mathrm{nm} \lesssim w \lesssim 780\,\mathrm{nm}$). Keeping the length constant for all of the processed structures worked very satisfyingly in the fabrication process. The sample therefore allowed for the systematic study of the transition from a two-dimensional square-like film to a quasi one-dimensional wire, i.e., a structure with a width that is comparable to the coherence length of the material. For the second chip D03-sar (**s**ame **a**spect **r**atio) the original aim was to process TiN structures which vary in their size but which all feature the same number of squares, i.e., the same aspect ratio ($l/w \sim 10$, $16\,\mathrm{nm} \lesssim w \lesssim 1\,\mu\mathrm{m}$). We identified the problem that the processing of a wire with a precisely defined width in the requested order of a few tens of nanometers is difficult to achieve. We therefore could not guarantee for the same aspect ratio as a common feature for all of the samples which would have been the requirement for any reliable statement about the size dependency of the samples. However the chip was especially worthwhile since we obtained very interesting results especially for the 100 nm wide wire of this sample series which was a major contribution for this work.

Zero Field Behavior and the Superconducting State

The employed wafer D03 is of the superconducting film type. We were able to show that upon decreasing the wire width, in zero magnetic field the structures permit a transition from the typical behavior of macroscopic superconducting TiN films to that of small Josephson junctions. The current-voltage characteristics of the wider structures show very similar features as those observed on macroscopic films: a sharp current peak followed by a current plateau that can likely be attributed to relaxation oscillations resulting from a sharp negative differential resistance. As we also know it from macroscopic TiN films we see the typical broadened transition to the superconducting zero-resistance state in the $R(T)$ dependence of the wider structures at zero field with the transition temperature being continuously suppressed when a magnetic field is applied and increased. In contrast the narrower wires develop a finite resistance already in zero field down to the lowest achievable temperatures where they exhibit a saturation of the resistance. We interpret this as an

indication of the global phase coherence being suppressed by the appearance of a weakly pronounced quantum phase slip regime. The saturation value increases for decreasing wire width which we explain by an increased phase slip rate in the narrower wires. The low temperature range where the saturation of the resistance is observed for the narrow wires is followed by a regime where the resistance of the samples increases almost exponentially with increasing temperature. The behavior of our samples in this regime shows deviations from the LAMH theory for thermally activated phase slips which is hardly surprising since this theory was put forward for conventional thin superconducting wires. However we were able to observe a good agreement when the temperature dependent prefactor in the LAMH theory is replaced by a constant parameter R_0. The resulting values for the free energy barrier exhibit a nearly proportional dependence on the cross sectional area of the wire as it is expected from theory.

Ivanchenko-Zil'berman Modeling of the Josephson-like I(V) Characteristics

The current-voltage characteristics of the narrow wires display the behavior of small Josephson junctions as they were described theoretically by Ivanchenko and Zil'berman and experimentally realized by Steinbach et al. [43, 44, 47] with a supercurrent branch and a critical current. We were able to model the observed $I(V)$ curves with the corresponding Ivanchenko-Zil'berman theory that we adapted by introducing a frequency dependent environment in contrast to the frequency independent external series resistance as it was assumed in the original theory. The effective temperature that we introduced as a fitting parameter showed a saturation around $T_{\mathrm{eff}} \sim 400\,\mathrm{mK}$. We think that this rather high saturation temperature emerging from the fits is likely another manifestation of the occurrence of phase slips in our wires. Amazingly, the theory including the small conducted adaptations was in very good agreement with our experimental results, even though on first sight we have a very different system on our hands. Our findings therefore support the view that polycrystalline TiN films can be modeled as Josephson junction networks. For sufficiently narrow TiN wires, the samples act as single Josephson junctions. The good agreement between the adapted Ivanchenko-Zil'berman theory and our experiment strongly substantiates the assumption that polycrystalline TiN films show an electronic fragmentation which leads to the formation of self organized superconducting islands. To our best knowledge, we were the first ones to model the behavior of narrow wires fabricated from a thin polycrystalline TiN film with an adapted version of the Ivanchenko-Zil'berman theory that was proposed for small tunnel junctions.

Magnetic Field Behavior and the Insulating State

In perpendicular magnetic field a non-monotonic magnetoresistance with a pronounced peak around $B \sim 2\,\mathrm{T}$ occurs for the narrow wires. The $R(T)$ curves of these wires at finite magnetic fields corresponding to the ascending branch of the magnetoresistance curve show a re-entrant insulating behavior. We see an indication of superconductivity down to a few hundreds of Millikelvin but at low temperatures an upturn of the resistance arises. This observation resembles the data obtained on Coulomb-blockaded linear artificial Josephson junction arrays [9]. It is explained by a magnetic field tuned Josephson coupling energy between superconducting islands. Thus the magnetic field effectively shifts the ratio of Josephson coupling energy E_J and charging energy E_C so that the sample switches from the superconducting to the insulating side. In the current-voltage characteristics the upturn in the resistance manifests as a smeared out blockaded range around zero voltage at the particular magnetic fields at low temperatures. This nonlinearity disappears for higher temperatures so that the $I(V)$ curve recovers to the superconducting type.

Strongly Blockaded States

In a second step we made use of an external high impedance environment for our measurements that we implemented as two $50\,\mathrm{k}\Omega$ resistors that were mounted very close to and in series with the sample. Our experimental results showed that the external high impedance environment is a necessary but not a sufficient prerequisite for the observation of highly insulating blockade-like states in narrow TiN wires. We believe that in combination with the capacitance to ground of the cryostat leads, the additional bias resistors effectively serve for the filtering of noise arising for instance from the transimpedance amplifier. The external high impedance environment therefore creates the necessary conditions for the observation of the strongly blockaded regime. This perception is also substantiated by the fact that the chosen amplification factor of the amplifier which involves a change of the amplifier noise has a huge impact on the sample behavior when no additional bias resistors are used. The higher the amplification and the lower the noise, the stronger is the observed insulating behavior of the sample. When additional bias resistors are used, the noise is efficiently filtered and the amplification shows no more influence on the sample behavior.
For the 100 nm wide wire of chip D03-sar2 the application of the external high impedance environment resulted in the strong enhancement of the formerly smeared out Coulomb blockade and weakly pronounced insulating re-entrance. However, we were not able to observe any influence of the external high impedance environment for example on the 50 nm

wide wire of chip D03-wd even though it showed a behavior similar to the earlier mentioned sample in the low impedance environment. It is known that quantum fluctuations of the Josephson phase are controlled by the electrodynamic environment. In the measurements of Haviland et al. on artificial networks, a high impedance environment was necessary for the observation of a strong Coulomb blockade in a normally superconducting junction [9, 61]. It was implemented as high impedance on-chip SQUID chains that were directly coupled to the junction. We believe that in the case of the 100 nm wide wire of chip D03-sar2 this high impedance environment develops in the wire itself. This can be understood in terms of the TiN film showing an inhomogeneous electronic fragmentation. The possibility to observe a strong Coulomb blockade is therefore sample dependent. We model the 100 nm wide wire of chip D03-sar2 with a hotspot region in the middle where quantum phase slips are proliferated. The rest of the wire serves as high impedance leads that are directly coupled to the hotspot region and guarantee for the necessary environment. These leads are the natural analog to the high impedance on-chip SQUID chains which are coupled to an artificial Josephson junction in the experiments of Haviland et al. [9].

Charge-Phase Duality – Dual Ivanchenko-Zil'berman Modeling of the Blockade-like I(V) Characteristics

In the magnetic field we were able to observe highly insulating states for the 100 nm wide wire of chip D03-sar2 when the additional bias resistors were employed where the resistance exceeded the minimum of the $R(T)$ characteristic by four orders of magnitude. The current-voltage curves display a characteristic crossover from Josephson-like behavior with a supercurrent branch and a critical current observed in zero field to a Coulomb blockade behavior that is characterized by a sharp blockaded range defined by a critical voltage. The curves reveal an exact duality. They are equally shaped with the roles of current and voltage interchanged. Instead of a critical current, a well defined critical voltage showed up with a similar temperature dependence as it is expected from duality. Furthermore we succeeded in modeling the obtained curves with the dual Ivanchenko-Zil'berman theory which results from the replacement of the relevant parameters by their dual ones. In particular charge and phase change their roles for the dual states. Again we adapted the theory with regard to a frequency dependent environment exactly dual to the adaptations on the superconducting side. Amazingly this slightly adapted theory yielded a very good agreement with our experimental observations. Our sample thus resembles the behavior of a single Josephson junction that is placed in a high impedance environment [67]. We interpret these results by modeling our wire with a hotspot region in the middle where quantum phase slips are proliferated. The rest of the wire serves as high impedance leads that are

directly coupled to the hotspot region and guarantee for the necessary environment. The wire effectively resembles the behavior of a quantum phase slip junction in the insulating capacitive regime. The ratio of the relevant energy scales is tuned by the enclosed magnetic flux. The critical voltage shows an oscillating dependence on the magnetic field and the size of a typical plaquette enclosing magnetic flux was estimated from the field scale on which the critical voltage is modulated. This yielded a reasonable size of $\sim 26\,\mathrm{nm}$.

Conclusion and Outlook

Within this work we found a consistent explanation for our observations in terms of random Josephson networks that arise through an electronic fragmentation of the film and the formation of self-organized superconducting islands. Our work is to a large extent resembling the data that was obtained for small Josephson junctions and artificial one-dimensional networks. Therefore it strongly supports the conception of TiN thin films as Josephson junction arrays. We were able to observe several phenomena that were so far only proven for artificial systems and further illustrated the duality between the superconducting and the insulating state in narrow TiN wires.

We found that wires with a width below $\sim 200\,\mathrm{nm}$ fabricated from a superconducting TiN film resemble the behavior of small Josephson junctions. At finite magnetic fields narrow wires ($w \lesssim 100\,\mathrm{nm}$) display a behavior that is equal to the one that is found for Coulomb-blockaded one-dimensional Josephson junction arrays. When additionally an external high impedance environment is applied in order to filter external noise, one of the narrow wires reveals a sharply defined critical voltage and an exact duality to the Josephson-like superconducting current-voltage characteristics. This behavior is very similar to that of a single Josephson junction in a high impedance environment.

The phenomenology of our results reflects a magnetic field induced crossover from a weak to a strong emergence of quantum phase slips. In the weak QPS regime in zero magnetic field the quantum phase slips reflect in a width dependent residual resistance of the wires at the lowest achievable temperatures and an increased effective temperature compared to the set bath temperature of the cryostat arising in the Ivanchenko-Zil'berman modeling. In the strong QPS regime the local quantum phase slip rate dramatically increases. This leads to a strongly blockaded regime where the corresponding current-voltage characteristics can be modeled with the dual Ivanchenko-Zil'berman expression that results from the expected duality of charge and flux that originates from the uncertainty relation which is valid for these two quantum variables.

The highly insulating behavior and the sharply defined blockade is however not observable for all of the narrow wires. This is very likely a consequence of the inhomogeneous

fragmentation of the films. In order to observe a sharp Coulomb blockade, high impedance leads have to form in the wire itself in order to create the necessary environment that is usually implemented as high impedance on-chip SQUID chains in artificial systems. In order to fabricate wires from thin TiN films which reliably allow for closer investigations on strong Coulomb blockade, a future prospect is to equip the processed samples with an on-chip high impedance environment. This could be realized for instance by meandering lead structures which are directly coupled to the TiN wires. With regard to further investigations on such strongly blockaded TiN nanowires, the ultimate building block in the duality considerations between Josephson and quantum phase slip junctions lies in the observation of current Shapiro steps. An observation of this dual effect to the well known voltage Shapiro steps appearing in Josephson junctions would be a breakthrough and a proof of the quantum phase slip junction character of our highly insulating narrow samples.

APPENDIX A

Sample Preparation Recipes

Cleaning Procedure

- put chip into acetone bath and place the beaker in an ultrasonic bath for approximately one minute
- rinse chip with acetone
- put chip into fresh acetone bath for approximately one minute
- rinse chip with acetone
- put chip into fresh acetone bath for approximately one minute
- rinse chip with acetone
- put chip into isopropyl alcohol bath for approximately one minute
- blow-dry with nitrogen

Application of Bonding Pads and Leads

- **Spin coating**
  PMMA 950K at 4 % (solvent: chlorobenzene)
  standard spinning parameters (speed 3000 rpm, acceleration time 0 s, duration 5 s; speed 8000 rpm, acceleration time 9 s, duration 30 s)

- **Baking**
  150 °C, 9 min

- **Electron-beam lithography**
  dose: 295 $\frac{\mu C}{cm^2}$ (additional dose factor 1.1 for small alignment crosses)
  working distance: 12 mm
  aperture: 30 µm

- **Developing**
  36 s in MIBK : isopropyl alcohol = 3 : 1, 31 s in isopropyl alcohol, blow-dry with nitrogen

- **Metal deposition**
  UNIVEX, 10 nm Ti, 120 nm Au, 16 nm Ti

- **Lift-off**
  acetone bath at 60 °C, at least 20 min
  flush chip with acetone using a syringe until all resist comes off with metal layer

- **Cleaning procedure**
  see above (skip ultrasonic bath)

Preparation of TiN structures

- **Spin coating**
  PMMA 50K at 3 % (solvent: chlorobenzene)
  standard spinning parameters (see above)

- **Baking**
  150 °C, 9 min

- **Electron-beam lithography**
  dose: 30000 $\frac{\mu C}{cm^2}$
  working distance: 10 mm
  aperture: 30 µm

- **Removing non-cross-linked PMMA**
  20 s in acetone, 30 s in propanol, blow-dry with nitrogen

- **Ion beam etching**
  CAIBE, recipe 21, 15 % Ar, 145 s

- **Cleaning procedure** as described above (without ultrasonic bath)

Finishing

- Glue chip into standard chip carrier using PMMA

- Bond chip with aluminum wire bonder
  loop height: 96 steps
  bond 1: power 180, 100 ms, bond 2: power 110, 100 ms

APPENDIX B

Ivanchenko-Zil'berman Fitting Instructions

We exemplarily explain the fitting process for the superconducting type of curves within the adapted Ivanchenko-Zil'berman theory in this section. For the insulating side the fitting routine works according to the dual Ivanchenko-Zil'berman relation in an exactly analogous manner to the following instructions.

Start Temperature

1. Start with a current-voltage characteristic that was obtained at an intermediate temperature ($T \sim 0.7\,\mathrm{K}$) where we can be sure that the effective temperature is identical to the set bath temperature of the cryostat.

2. Chose R_N in such a way, that the adjusted $I(V)$ curve resulting from a recalculation of the current axis as $I = I_{\mathrm{det}} - V/R_N$ roughly approaches $I = 0$ asymptotically at high voltages.

3. Extract the critical current of the resulting curve.

4. The Ivanchenko-Zil'berman relation where we introduced an effective temperature is

given by

$$I(V_{B_{IZ}}) = I_0 \,\mathrm{Im}\left[\frac{\mathcal{I}_{1-i\beta\hbar V_{B_{IZ}}/2eR_B}(\beta E_J)}{\mathcal{I}_{-i\beta\hbar V_{B_{IZ}}/2eR_B}(\beta E_J)}\right],\ \beta = \frac{1}{k_B T_{\mathrm{eff}}},\ V = V_{B_{IZ}} - R_B I. \quad \text{(B.1)}$$

According to this relation, we want to generate a curve in *Mathematica* that matches the critical current obtained in step 3. The indexes of the Bessel functions have no influence on the value of the local maximum, i.e., the critical current of the curve. We can therefore define the simplified function

$$f(x,c) = y = I_0 \,\mathrm{Im}\left[\frac{\mathcal{I}_{1-ix}(c)}{\mathcal{I}_{-ix}(c)}\right] \quad \text{(B.2)}$$

in *Mathematica* and define $c = \beta E_J$ in the *Mathematica* workbook as

$$c = \frac{\hbar}{2ek_B}\,\frac{1}{T_{\mathrm{eff}}}\,I_0. \quad \text{(B.3)}$$

5. Since we chose an intermediate temperature where we can be sure that it is identical to the effective temperature, we pass the set bath temperature of the cryostat at which the $I(V)$ curve was recorded to the calculation as T_{eff}. Now we vary the intrinsic critical current I_0 in such a way that the local maximum of the generated curve in *Mathematica* matches the critical current that we extracted in step 3.

6. Import the resulting data into *Origin*.

7. Next we have to calculate the actual voltage from the x-values. The imported y-values are already identical to the current values I. When we compare equation B.2 to equation B.1 we see that

$$x = bV_{B_{IZ}} \quad \text{(B.4)}$$

with

$$\begin{aligned} b &= \frac{\beta\hbar}{2eR_B} \\ &= \frac{\hbar}{2ek_B}\,\frac{1}{T_{\mathrm{eff}}}\,\frac{1}{R_B}. \end{aligned} \quad \text{(B.5)}$$

Therefore we have to calculate the voltage according to

$$\begin{aligned} V &= V_{B_{IZ}} - R_B I \\ &= \frac{x}{b} - R_B I \\ &= \frac{x}{\frac{\hbar}{2ek_B}\frac{1}{T_{\text{eff}}}\frac{1}{R_B}} - R_B I \\ &= R_B \left(x\, T_{\text{eff}}\, \frac{2ek_B}{\hbar} - I \right). \end{aligned} \tag{B.6}$$

I denotes the y-values as they were generated in *Mathematica* and imported to *Origin* in step 6. For T_{eff} we again use the set cryostat bath temperature. The parameter R_B is now varied until the match between fit curve and the curve resulting from the measurement curve where the parallel resistance R_N has been subtracted (see step 2) is optimal.
The influence of our adaptation, i.e., the recalculation of the voltage V from $V_{B_{IZ}}$ according to $V = V_{B_{IZ}} - R_B I$ is illustrated in figure B.1(a). The blue dashed line shows the $I(V_{B_{IZ}})$ curve resulting from the Ivanchenko-Zil'berman relation (see equation 2.36). The resulting curve matches the broadening but not the slope of our measurement curve (green). Our adaptation, i.e., the subtraction of a voltage drop across a serial resistance R_B (see section 4.1.4) yields the red solid curve, which fits our experimental data. The dual situation for the insulating side is sketched in figure B.1(b). Here the current I is recalculated from $I_{B_{IZ}}$ according to $I = I_{B_{IZ}} - V/R_B$. The blue dashed line corresponds to the $I_{B_{IZ}}(V)$ curve resulting from the dual Ivanchenko-Zil'berman relation (see equation 2.39). Our adaptation, i.e., the subtraction of a current through a parallel resistance, yields the red solid curve.

8. Since in step 2 we just made a rough assumption for the value of R_N, the match between fit curve and measurement curve might still be optimized by a slight variation of R_N. Especially the deviation between both curves at high voltages shows whether R_N should be decreased or increased. Therefore we have to start again from step 2 and fine-tune R_N in a reasonable way. Subsequently step 3–7 are carried out again. All steps should then be repeated (maybe several times) until a self-consistency is reached.

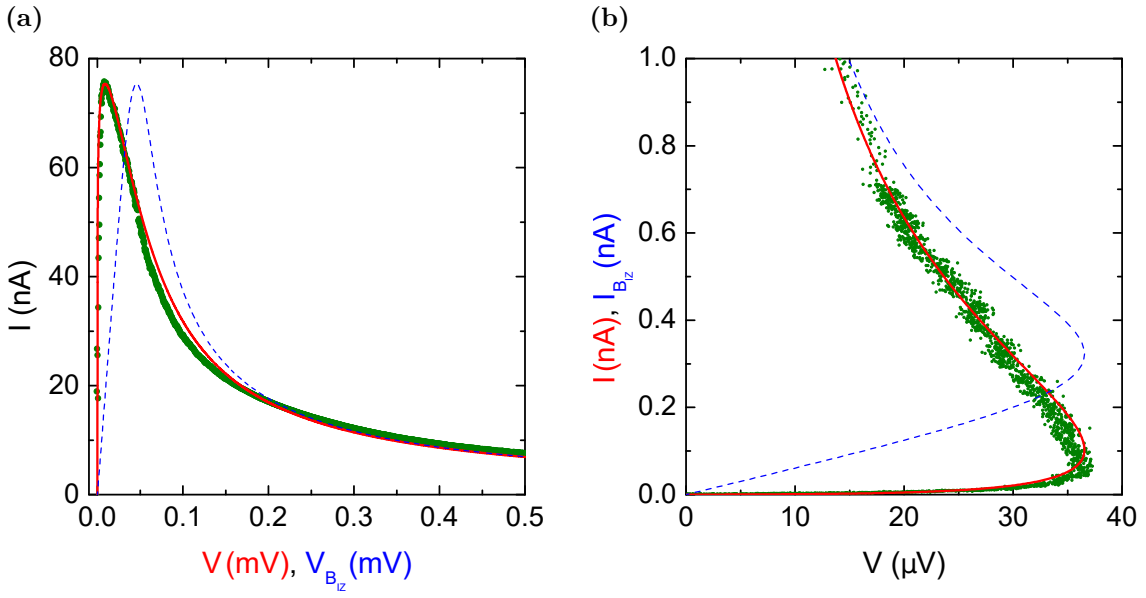

Figure B.1.: (a) Illustration of our adaptation for the Ivanchenko-Zil'berman theory on the superconducting side. The experimental data is plotted in green. The blue dashed line shows the $I(V_{BIZ})$ curve resulting from the original relation. The red solid curve includes our adaptation. **(b)** Dual situation for the insulating side. The green dots display the measurement curve. The blue dashed line shows the $I_{BIZ}(V)$ curve resulting from the original relation. The red solid curve includes our adaptation.

Higher Temperatures

We started the procedure for an intermediate temperature where we can be sure that the effective temperature T_{eff} is identical to the set bath temperature of the cryostat and adjusted the intrinsic critical current I_0 in order to make the local maximum of the fit curve match the critical current of the measurement curve. The procedure can now be carried out for measurement curves recorded at higher temperatures in the same way, i.e., the bath temperature is used as the effective temperature in steps 5 and 7, whereby I_0 will continuously decrease for increasing temperatures. At a certain temperature, it won't be possible anymore to obtain satisfying fit results since the subtraction of the normal state current in step 2 yields very flat $I(V)$ curves where the fit parameters can't be adjusted in a reasonable way anymore. When this is the case, continue with the low temperatures as described in the next section.

Lower Temperatures

From the temperature where we started the fitting routine, we gradually go to smaller temperatures now. We continue in handing over the bath temperature as the effective temperature T_{eff} and in adjusting I_0 in order to obtain the correct value of the critical current in step 5. In doing so, I_0 will initially be increasing for decreasing temperatures. However, at a certain temperature we find that I_0 would start to decrease when the bath temperature is still used as the effective temperature which is not reasonable. At this point, we modify the process in the way that I_0 is kept constant at the value that was obtained at the previous temperature and instead, we vary the effective temperature in step 5 in such a way that the correct value of the critical current is achieved. The resulting value of T_{eff} also has to be used then in step 7.
The resulting effective temperature now continuously deviates more and more upwards from the decreasing bath temperature, i.e., it shows a saturation behavior. Usually at the transition point between adjusting I_0 and adjusting T_{eff} small adaptations have to be made in order to prevent the effective temperature from locally dropping below the bath temperature which would also not be reasonable.

Bibliography

[1] T. I. Baturina, A. Y. Mironov, V. M. Vinokur, M. R. Baklanov, and C. Strunk, "Localized superconductivity in the quantum-critical region of the disorder-driven superconductor-insulator transition in TiN thin films," *Phys. Rev. Lett.*, vol. 99, no. 25, p. 257003, 2007.

[2] B. Sacépé, C. Chapelier, T. I. Baturina, V. M. Vinokur, M. R. Baklanov, and M. Sanquer, "Disorder-induced inhomogeneities of the superconducting state close to the superconductor-insulator transition," *Phys. Rev. Lett.*, vol. 101, no. 15, p. 157006, 2008.

[3] C. Carbillet, S. Caprara, M. Grilli, C. Brun, F. Debontridder, B. Vignolle, W. Tabis, D. Demaille, L. Largeau, K. Ilin, M. Siegel, D. Roditchev, and B. Leridon, "Confinement of superconducting fluctuations due to emergent electronic inhomogeneities," *Phys. Rev. B*, vol. 93, no. 14, p. 144509, 2016.

[4] M. Mondal, A. Kamlapure, M. Chand, G. Saraswat, S. Kumar, J. Jesudasan, L. Benfatto, V. Tripathi, and P. Raychaudhuri, "Phase fluctuations in a strongly disordered s-wave NbN superconductor close to the metal-insulator transition," *Phys. Rev. Let.*, vol. 106, no. 4, p. 047001, 2011.

[5] R. Fazio and H. van der Zant, "Quantum phase transitions and vortex dynamics in superconducting networks," *Phys. Rep.*, vol. 355, no. 4, pp. 235 – 334, 2001.

[6] H. S. J. van der Zant, W. J. Elion, L. J. Geerlings, and J. E. Mooij, "Quantum phase transitions in two dimensions: Experiments in Josephson-junction arrays," *Phys. Rev. B*, vol. 54, no. 14, p. 10081, 1997.

[7] P. Martinoli and C. Leemann, "Two dimensional Josephson junction arrays," *J. Low Temp. Phys.*, vol. 118, no. 5, pp. 699–731, 2000.

[8] R. Newrock, C. Lobb, U. Geigenmüller, and M. Octavio, "The two-dimensional physics of Josephson junction arrays," in *Solid State Physics* (H. Ehrenreich and F. Spaepen, eds.), vol. 54 of *Solid State Physics*, pp. 263 – 512, Academic Press, 2000.

[9] D. B. Haviland, K. Andersson, and P. Ågren, "Superconducting and insulating behavior in one-dimensional Josephson junction arrays," *J. Low Temp. Phys.*, vol. 118, no. 5, pp. 733–749, 2000.

[10] Y. Nakamura, Y. Pashkin, and J. Tsai, "Coherent control of macroscopic quantum states in a single-Cooper-pair box," *Nature*, vol. 398, pp. 786–788, 1999.

[11] Y. Makhlin, G. Schön, and A. Shnirman, "Josephson-junction qubits with controlled couplings," *Nature*, vol. 398, pp. 305–307, 1999.

[12] D. Vion, A. Aassime, A. Cottet, P. Joyez, H. Pothier, C. Urbina, D. Esteve, and M. H. Devoret, "Manipulating the quantum state of an electrical circuit," *Science*, vol. 296, no. 5569, pp. 886–889, 2002.

[13] T. P. Orlando, J. E. Mooij, L. Tian, C. H. van der Wal, L. S. Levitov, S. Lloyd, and J. J. Mazo, "Superconducting persistent-current qubit," *Phys. Rev. B*, vol. 60, pp. 15398–15413, 1999.

[14] J. E. Mooij, T. P. Orlando, L. Levitov, L. Tian, C. H. van der Wal, and S. Lloyd, "Josephson persistent-current qubit," *Science*, vol. 285, no. 5430, pp. 1036–1039, 1999.

[15] M. Tinkham, *Introduction to Superconductivity*. Mineola: Dover Publications, 2nd ed., 1996.

[16] W. Buckel and R. Kleiner, *Supraleitung, Grundlagen und Anwendungen*. Weinheim: Wiley-VCH, 6th ed., 2012.

[17] S. Hunklinger and C. Enss, *Low-Temperature Physics*. Berlin Heidelberg: Springer, 1st ed., 2005.

[18] C. Kittel, *Introduction to Solid State Physics*. Hoboken: John Wiley & Sons, Inc., 8th ed., 2005.

[19] H. Kamerlingh Onnes, "Further experiments with liquid helium," *Leiden Comm.*, vol. 120b, 122b, 124c, 1911.

[20] W. Meißner and R. Ochsenfeld, "Ein neuer Effekt bei Eintritt der Supraleitfähigkeit," *Naturwissenschaften*, vol. 21, no. 44, pp. 787–788, 1933.

[21] J. N. Rjabinin and L. W. Shubnikow, "Magnetic Properties and Critical Currents of Supra-conducting Alloys," *Nature*, vol. 135, pp. 581–582, Apr. 1935.

[22] A. A. Abrikosov, "On the magnetic properties of superconductors of the second group," *Sov. Phys. JETP*, vol. 5, no. 6, pp. 1174–1182, 1957.

[23] F. London and H. London, "The electromagnetic equations of the supraconductor," *Proc. Roy. Soc.*, vol. 149, no. 866, p. 71, 1935.

[24] L. N. Cooper, "Bound electron pairs in a degenerate fermi gas," *Phys. Rev.*, vol. 104, no. 4, pp. 1189–1190, 1956.

[25] H. Fröhlich, "Theory of the superconducting state," *Phys. Rev.*, vol. 79, no. 5, pp. 845–856, 1950.

[26] J. Bardeen, "Electron-vibration interactions and superconductivity," *Rev. Mod. Phys.*, vol. 23, no. 3, pp. 261–270, 1951.

[27] E. Maxwell, "Isotope effect in the superconductivity of mercury," *Phys. Rev.*, vol. 78, no. 4, p. 477, 1950.

[28] J. Bardeen, L. N. Cooper, and J. R. Schrieffer, "Theory of superconductivity," *Phys. Rev.*, vol. 108, no. 5, pp. 1175–1204, 1957.

[29] V. L. Ginzburg and L. D. Landau, "On the theory of superconductivity," *Zh. Eksp. Teor. Fiz.*, vol. 20, pp. 1064–1082, 1950.

[30] L. Landau, "On the theory of phase transitions," *Zh. Eksp. Teor. Fiz.*, vol. 7, pp. 19–32, 1937.

[31] L. P. Gor'kov, "Microscopic derivation of the Ginzburg-Landau equations in the theory of superconductivity," *Sov. Phys. JETP*, vol. 36, no. 9, pp. 1364–1367, 1959.

[32] B. D. Josephson, "Possible new effects in superconductive tunnelling," *Phys. Lett.*, vol. 1, no. 7, pp. 251–253, 1962.

[33] A. Barone and G. Paterno, *Physics and Applications of the Josephson Effect*. New York: John Wiley & Sons, Inc, 1982.

[34] J. Q. You and F. Nori, "Atomic physics and quantum optics using superconducting circuits," *Nature*, vol. 474, pp. 589–597, 2011.

[35] M. H. Devoret, *Quantum Fluctuations in Electrical Circuits.* New York: Elsevier Science, 1997.

[36] G. Schön and A. Zaikin, "Quantum coherent effects, phase transitions, and the dissipative dynamics of ultra small tunnel junctions," *Phys. Rep.*, vol. 198, no. 5-6, pp. 237–413, 1990.

[37] K. K. Likharev, *Dynamics of Josephson Junction and Circuits.* New York: Gordon and Breach, 3rd ed., 1996.

[38] W. C. Stewart, "Current-voltage characteristics of josephson junctions," *Appl. Phys. Lett.*, vol. 12, no. 8, pp. 277–280, 1968.

[39] D. E. McCumber, "Effect of ac impedance on dc voltage-current characteristics of superconductor weak-link junctions," *J. Appl. Phys.*, vol. 39, pp. 3113–3118, 1968.

[40] A. Bezryadin, *Superconductivity in Nanowires.* Weinheim: Wiley VCH, 1st ed., 2012.

[41] J. Clarke and A. I. Braginski, *The SQUID Handbook*, vol. 1. Weinheim: Wiley VCH, 2006.

[42] V. Ambegaokar and B. I. Halperin, "Voltage due to thermal noise in the dc Josephson effect," *Phys. Rev. Lett.*, vol. 22, no. 25, pp. 1364–1366, 1969.

[43] Y. M. Ivanchenko and L. A. Zil'berman, "The josephson effect in small tunnel contacts," *Zh. Eksp. Teor. Fiz.*, vol. 55, pp. 2395–2402, 1968.

[44] Y. M. Ivanchenko and L. A. Zil'berman, "The josephson effect in small tunnel contacts," *Sov. Phys. JETP*, vol. 28, no. 6, pp. 1272–1276, 1969.

[45] Y. M. Ivanchenko and L. A. Zil'berman, "Destruction of Josephson current by fluctuations," *Zh. Eksp. Teor. Fiz.*, vol. 8, no. 4, p. 189, 1968.

[46] Y. M. Ivanchenko and L. A. Zil'berman, "Destruction of Josephson current by fluctuations," *Sov. Phys. JETP*, vol. 8, pp. 113–115, 1968.

[47] A. Steinbach, P. Joyez, A. Cottet, D. Esteve, M. H. Devoret, M. E. Huber, and J. M. Martinis, "Direct measurement of the Josephson supercurrent in an ultrasmall Josephson junction," *Phys. Rev. Lett.*, vol. 87, no. 13, p. 137003, 2001.

[48] J. E. Mooij and Y. V. Nazarov, "Superconducting nanowires as quantum phase-slip junctions," *Nat. Phys.*, vol. 2, no. 3, pp. 169–172, 2006.

[49] "Nanowerk." `http://www.nanowerk.com/news/newsid=24963.php`. Visited on 03.11.2016.

[50] J. S. Lehtinen, K. Zakharov, and K. Y. Arutyunov, "Coulomb blockade and bloch oscillations in superconducting Ti nanowires," *Phys. Rev. Lett.*, vol. 109, no. 18, p. 187001, 2012.

[51] J. C. Fenton, C. H. Webster, and P. A. Warburton, "Materials for superconducting nanowires for quantum phase-slip devices," *JPCS*, vol. 286, no. 1, p. 012024, 2011.

[52] T. T. Hongisto and A. B. Zorin, "Single-charge transistor based on the charge-phase duality of a superconducting nanowire circuit," *Phys. Rev. Lett.*, vol. 108, no. 9, p. 097001, 2012.

[53] A. M. Hriscu and Y. V. Nazarov, "Coulomb blockade due to quantum phase slips illustrated with devices," *Phys. Rev. B*, vol. 83, no. 17, p. 174511, 2011.

[54] O. V. Astafiev, L. B. Ioffe, S. Kafanov, Y. A. Pashkin, K. Y. Arutyunov, D. Shahar, O. Cohen, and J. S. Tsai, "Coherent quantum phase slip," *Nature*, vol. 484, pp. 355–358, 2012.

[55] J. E. Mooij, G. Schön, A. Shnirman, T. Fuse, C. J. P. M. Harmans, H. Rotzinger, and A. H. Verbruggen, "Superconductor–insulator transition in nanowires and nanowire arrays," *New J. Phys.*, vol. 17, p. 033006, 2015.

[56] F. Altomare and A. M. Chang, *One-Dimensional Superconductivity in Nanowires*. Weinheim: Wiley VCH, 1st ed., 2013.

[57] S. Corlevi, *Quantum effects in nanoscale Josephson junction circuits*. PhD thesis, KTH Royal Institute of Technology, Stockholm, 2006.

[58] W. Guichard and F. W. J. Hekking, "Phase-charge duality in Josephson junction circuits: Role of inertia and effect of microwave irradiation," *Phys. Rev. B*, vol. 81, no. 6, p. 064508, 2010.

[59] D. V. Averin, A. B. Zorin, and K. K. Likharev, "Bloch oscillations in small Josephson junctions," *Sov. Phys. JETP*, vol. 61, no. 2, pp. 407–413, 1985.

[60] K. K. Likharev and A. B. Zorin, "Theory of the bloch-wave oscillations in small Josephson junctions," *J. Low Temp. Phys.*, vol. 59, no. 3, pp. 347–382, 1985.

[61] M. Watanabe and D. B. Haviland, "Quantum effects in small-capacitance single Josephson junctions," *Phys. Rev. B*, vol. 67, no. 9, p. 094505, 2003.

[62] A. Di Marco, F. W. J. Hekking, and G. Rastelli, "Quantum phase-slip junction under microwave irradiation," *Phys. Rev. B*, vol. 91, p. 184512, May 2015.

[63] L. S. Kuzmin and H. D. B., "Observation of the bloch oscillations in an ultrasmall Josephson junction," *Phys. Rev. Lett.*, vol. 67, no. 20, pp. 2890–2893, 1991.

[64] D. B. Haviland, L. S. Kuzmin, P. Delsing, K. K. Likharev, and T. Claeson, "Experimental evidence for the Coulomb blockade of Cooper pair tunneling and bloch oscillations in single Josephson junctions," *Z. Phys. B*, vol. 85, no. 3, pp. 339–347, 1991.

[65] L. S. Kuzmin, Y. A. Pashkin, A. B. Zorin, and T. Claeson, "Linewidth of bloch oscillations in small Josephson junctions," *Physica B*, vol. 203, no. 3-4, pp. 376–380, 1994.

[66] I. S. Beloborodov, F. W. J. Hekking, and F. Pistolesi, "Influence of thermal fluctuations on an underdamped Josephson tunnel junction," in *New Directions in Mesoscopic Physics (Towards Nanoscience)* (R. Fazio, V. F. Gantmakher, and Y. Imry, eds.), pp. 339–349, Dordrecht: Springer Netherlands, 2003.

[67] S. Corlevi, W. Guichard, F. W. D. Hekking, and D. B. Haviland, "Phase-charge duality of a Josephson junction in a fluctuating electromagnetic environment," *Phys. Rev. Lett.*, vol. 97, no. 9, p. 096802, 2006.

[68] V. F. Gantmakher and V. T. Dolgopolov, "Superconductor–insulator quantum phase transition," *Phys. Usp.*, vol. 53, no. 1, pp. 1–49, 2010.

[69] D. B. Haviland, Y. Liu, and A. M. Golman, "Onset of superconductivity in the two-dimensional limit," *Phys. Rev. Lett.*, vol. 62, no. 18, pp. 2180–2183, 1989.

[70] S. Kobayashi, "Experiments of random Josephson network," *Physica B*, vol. 152, no. 1-2, p. 223, 1988.

[71] A. Frydman, "The superconductor insulator transition in systems of ultrasmall grains," *Physica C*, vol. 391, no. 2, pp. 189 –195, 2003.

[72] D. Shahar and Z. Ovadyahu, "Superconductivity near the mobility edge," *Phys. Rev. B*, vol. 46, no. 17, pp. 10917–10922, 1992.

[73] T. I. Baturina, C. Strunk, M. R. Baklanov, and A. Satta, "Quantum metallicity on the high-field side of the superconductor-insulator transition," *Phys. Rev. Lett.*, vol. 98, no. 12, p. 127003, 2007.

[74] C. D. Chen, P. Delsing, D. B. Haviland, Y. Harada, and T. Claeson, "Scaling behavior of the magnetic-field-tuned superconductor-insulator transition in two-dimensional Josephson-junction arrays," *Phys. Rev. B*, vol. 51, no. 21, pp. 15645–15648, 1995.

[75] A. J. Rimberg, T. R. Ho, C. Kurdak, K. L. Campman, and A. C. Gossard, "Dissipation-driven superconductor-insulator transition in a two-dimensional Josephson-junction array," *Phys. Rev. Lett.*, vol. 78, no. 13, pp. 2632–2635, 1997.

[76] V. M. Vinokur, T. I. Baturina, M. V. Fistul, A. Y. Mironov, M. R. Baklanov, and C. Strunk, "Superinsulator and quantum synchronization," *Nature*, vol. 452, pp. 613–615, 2008.

[77] Y. Dubi, Y. Meir, and Y. Avishai, "Theory of the magnetoresistance of disordered superconducting films," *Phys. Rev. B*, vol. 73, no. 5, p. 054509, 2006.

[78] M. V. Fistul, V. M. Vinokur, and T. I. Baturina, "Collective Cooper-pair transport in the insulating state of Josephson-junction arrays," *Phys. Rev. Lett.*, vol. 100, no. 8, p. 086805, 2008.

[79] A. Ghosal, M. Randeria, and N. Trivedi, "Role of spatial amplitude fluctuations in highly disordered s-wave superconductors," *Phys. Rev. Lett.*, vol. 81, no. 18, pp. 3940–3943, 2001.

[80] A. Ghosal, M. Randeria, and N. Trivedi, "Inhomogeneous pairing in highly disordered s-wave superconductors," *Phys. Rev. B*, vol. 65, no. 1, p. 014501, 2001.

[81] Y. Dubi, Y. Meir, and Y. Avishai, "Nature of the superconductor–insulator transition in disordered superconductors," *Nature*, vol. 449, pp. 876–880, 2007.

[82] M. J. Kelly and C. Weisbuch, *The Physics and Fabrication of Microstructures and Microdevices - Proceedings of the Winter School Les Houches, France, March 25–April 5, 1986*. Berlin Heidelberg: Springer, 1986.

[83] M. Stepanova and S. Dew, *Nanofabrication - Techniques and Principles*. Wien: Springer, 1st ed., 2012.

[84] S. V. Postolova, A. Y. Mironov, and T. I. Baturina, "Nonequilibrium transport near the superconducting transition in TiN films," *JETP Lett.*, vol. 100, no. 10, pp. 635–641, 2015.

[85] Private communication with T. I. Baturina.

[86] S. Ma, C. Con, M. Yavuz, and B. Cui, "Polystyrene negative resist for high-resolution electron beam lithography," *NRL*, vol. 6, no. 1, p. 446, 2011.

[87] I. Zailer, J. E. F. Frost, V. Chabasseur-Molyneux, C. J. B. Ford, and M. Pepper, "Crosslinked pmma as a high-resolution negative resist for electron beam lithography and applications for physics of low-dimensional structures," *Semicond. Sci. Tech.*, vol. 11, no. 8, p. 1235, 1996.

[88] C. T. Leondes, *Mems/Nems*. Springer US, 1st ed., 2006.

[89] F. Pobell, *Matter and Methods at Low Temperatures*. Berlin Heidelberg: Springer, 3rd ed., 2007.

[90] A. T. Bollinger, R. C. Dinsmore, A. Rogachev, and A. Bezryadin, "Determination of the superconductor-insulator phase diagram for one-dimensional wires," *Phys. Rev. Lett.*, vol. 101, no. 22, p. 227003, 2008.

[91] C. N. Lau, N. Markovic, M. Bockrath, a. Bezryadin, and M. Tinkham, "Quantum phase slips in superconducting nanowires," *Phys. Rev. Lett.*, vol. 87, no. 21, p. 217003, 2001.

[92] M. Zgirski, K. P. Riikonen, V. Touboltsev, and K. Arutyunov, "Size dependent breakdown of superconductivity in ultranarrow nanowires," *Nano Lett.*, vol. 5, no. 6, pp. 1029–1033, 2005.

[93] F. Altomare, A. M. Chang, M. R. Melloch, Y. Hong, and C. W. Tu, "Evidence for macroscopic quantum tunneling of phase slips in long one-dimensional superconducting Al wires," *Phys. Rev. Lett.*, vol. 97, no. 1, p. 017001, 2006.

[94] N. Giordano, "Evidence for macroscopic quantum tunneling in one-dimensional superconductors," *Phys. Rev. Lett.*, vol. 61, pp. 2137–2140, Oct 1988.

[95] A. Bezryadin, "Quantum suppression of superconductivity in nanowires," *J. Phys.: Condens. Matter*, vol. 20, no. 4, p. 043202, 2008.

[96] J. S. Langer and V. Ambegaokar, "Intrinsic resistive transition in narrow superconducting channels," *Phys. Rev.*, vol. 164, pp. 498–510, Dec 1967.

[97] D. E. McCumber and B. I. Halperin, "Time scale of intrinsic resistive fluctuations in thin superconducting wires," *Phys. Rev. B*, vol. 1, pp. 1054–1070, Feb 1970.

[98] A. Schmid, "A time dependent Ginzburg-Landau equation and its application to the problem of resistivity in the mixed state," *Phys.Kondenss. Mat.*, vol. 5, no. 4, pp. 302–317, 1966.

[99] C. Caroli and K. Maki, "Fluctuations of the order parameter in type-II superconductors. i. dirty limit," *Phys. Rev.*, vol. 159, pp. 306–315, Jul 1967.

[100] C. Caroli and K. Maki, "Fluctuations of the order parameter in type-II superconductors. ii. pure limit," *Phys. Rev.*, vol. 159, pp. 316–326, Jul 1967.

[101] E. Abrahams and T. Tsuneto, "Time variation of the Ginzburg-Landau order parameter," *Phys. Rev.*, vol. 152, pp. 416–432, Dec 1966.

[102] J. W. F. Woo and E. Abrahams, "Relaxation of the superconducting order parameter," *Phys. Rev.*, vol. 169, pp. 407–413, May 1968.

[103] K. Kronfeldner, *Transport properties of critically disordered TiN films.* PhD thesis, Universität Regensburg, Regensburg, 2016.

[104] F. L. Vernon Jr. and R. J. Pedersen, "Relaxation oscillations in Josephson junctions," *J. Appl. Phys.*, vol. 39, pp. 2661–2664, 1968.

[105] I. M. Pop, I. Protopopov, F. Lecocq, Z. Peng, B. Pannetier, O. Buisson, and W. Guichard, "Measurement of the effect of quantum phase slips in a Josephson junction chain," *Nature Phys.*, vol. 6, pp. 589–592, 2010.

[106] W. Kuo and C. D. Chen, *Magnetic Field Tuned Superconductor-Insulator Phase Transitions in One-Dimensional Arrays of Josephson Junctions.* Scientific World, 2003.

Acknowledgment

The work presented in this thesis could only be completed thanks to the help of many people who supported and assisted me in my time as a PhD student.

I would like to give my sincere thanks to my supervisor Prof. Dr. Christoph Strunk for his encouragement and guidance in all stages of my research work. He offered me advice and always guided me in the right direction in moments where I did not know where my PhD was heading. Without his dedication to my topic and the countless hours of discussions, this work could not have been successful.

Besides my advisor I would like to thank the other members of my committee, Prof. Dr. Tilo Wettig, Prof. Dr. Sergey Ganichev and in particular Prof. Dr. Ferdinand Evers who agreed to be co-examiner of this thesis.

Special thanks are given to Prof. Dr. Tatyana Baturina for the collaboration and support and for being a great mentor as an outstanding woman physicist and professor for me. I am grateful that I had the chance to work with her during her time as a guest member of our research group.

I am very thankful to Prof. Dr. Valerii Vinokur, Prof. Dr. David Haviland and Prof. Dr. Yuli Nazarov for the fruitful and kind discussions during their visits in Regensburg.

For the supply with TiN material I would like to thank Prof. Dr. Mikhail Baklanov.

Gratitude is owed to Prof. Dr. Dieter Weiss, the head of our chair, for providing me access to the cleanroom and all other chair equipment and facilities.

I want to thank Thomas Solleder and Christian Haimerl for the friendly supply with liquid helium that I could always count on, even in times where it was running low (literally speaking).

Our chair technicians Thomas Haller, Michael Weigl, Uli Gürster and Cornelia Linz are acknowledged for their assistance in all technical issues that came up. I would also like to thank the mechanics and electronics workshop for their kind support.

My time at the chair was made enjoyable in large part thanks to our secretaries Claudia Rahm and Elke Haushalter who do not only shoulder all the administrative work for us but also enrich the chair with their cheerful manner and their kindness. Thanks a lot for that!

Many thanks go to my TiN fellow Klaus. He was a great office mate, an indispensable source of help in all questions concerning cryogenics, measuring techniques and data analysis and most importantly became a really good friend.

I would also like to thank my other office mates Lorenz and Markus as well as all other members of our group who were always a welcome interruption from physics and who made everyday life at university valuable and joyful.

My time in our research group gave me the chance to make wonderful friendships. I am glad that I met Sasmita and Ondrej who became dear friends of mine in the last years. Thank you and your families for all the nice moments together!

For the thorough proofreading a big thank you goes to my dearest cousin Nenja and her spouse Jean.

I wish to thank Daniel for being the most warm-hearted, patient and humorous person I have ever met. He is by far the best consequence of my PhD time and I can't express how thankful I am to have him in my life.

Lastly, I would like to thank my family with all my heart for all their love, encouragement and support that I could always rely on despite the challenging times that we had to go through together.